

---

**Forecast influence of  
adaptive airborne observations  
in the environment of tropical cyclones  
in the western North Pacific basin**

---

Dissertation  
an der Fakultät für Physik  
der Ludwig-Maximilians-Universität  
München

vorgelegt von  
Florian Harnisch  
aus Prien am Chiemsee

München März 2011

1. Gutachter: Prof. Dr. G. C. Craig
  2. Gutachter: Prof. Dr. U. Schumann
- Tag der mündlichen Prüfung: 1. Juni 2011

# Contents

<b>Contents</b>	<b>i</b>
<b>Zusammenfassung</b>	<b>iii</b>
<b>Abstract</b>	<b>v</b>
<b>1 Introduction</b>	<b>1</b>
1.1 Background . . . . .	1
1.2 Adaptive observations for tropical cyclones . . . . .	4
1.3 Humidity observations by new observing systems . . . . .	7
1.4 Goals and outline . . . . .	8
<b>2 Methods and data</b>	<b>11</b>
2.1 Data assimilation . . . . .	12
2.1.1 Variational approach . . . . .	12
2.1.2 Incremental 4D-Var . . . . .	15
2.2 ECMWF analysis and forecasting system . . . . .	17
2.3 Observation targeting . . . . .	20
2.4 Observing system experiments . . . . .	23
2.5 T-PARC observations . . . . .	26
2.6 Dropsonde system . . . . .	30
2.7 Differential absorption lidar . . . . .	31
2.7.1 Basic principles . . . . .	31
2.7.2 Airborne WALES demonstrator . . . . .	34
<b>3 The influence of adaptive dropsonde observations on ECMWF typhoon track forecasts</b>	<b>37</b>
3.1 Introduction . . . . .	37
3.2 Experimental design . . . . .	38
3.3 Results . . . . .	39
3.4 Importance of correct observation times . . . . .	43
3.5 Discussion and conclusion . . . . .	45

<b>4</b>	<b>Strategies for adaptive tropical cyclone observations</b>	<b>47</b>
4.1	Introduction . . . . .	47
4.2	Experimental design . . . . .	48
4.3	Results . . . . .	52
4.3.1	Assimilation statistics of TC centre and core observations . . . . .	52
4.3.2	Typhoon track forecasts . . . . .	54
4.3.3	Typhoon intensity forecast . . . . .	64
4.4	Discussion and conclusion . . . . .	66
<b>5</b>	<b>Adaptive DIAL humidity observations</b>	<b>69</b>
5.1	Introduction . . . . .	69
5.2	Setup of assimilation experiments . . . . .	70
5.2.1	Precipitable water content . . . . .	70
5.2.2	Experiments . . . . .	71
5.2.3	Error specification . . . . .	72
5.3	Results . . . . .	72
5.3.1	Comparison of DIAL and dropsonde observations . . . . .	72
5.3.2	Assimilation statistics of the DIAL experiments . . . . .	75
5.3.3	Analysis impact . . . . .	77
5.3.4	Forecast impact . . . . .	80
5.4	Case study: 19 September 2008 . . . . .	82
5.5	Discussion and conclusion . . . . .	87
<b>6</b>	<b>Conclusions and outlook</b>	<b>91</b>
	<b>List of abbreviations</b>	<b>95</b>
	<b>Bibliography</b>	<b>99</b>
	<b>Acknowledgements</b>	<b>111</b>
	<b>Curriculum vitae</b>	<b>113</b>

# Zusammenfassung

Im Rahmen der THORPEX Pacific Asian Regional Campaign (T-PARC) 2008, wurde ein beispielloser Datensatz von Flugzeugmessungen im westlichen Nordpazifik gewonnen. Von mehreren Flugzeugen wurden insgesamt etwa 1500 Dropsonden abgeworfen, die hauptsächlich zur Beobachtung tropischer Wirbelstürme dienten. Zusätzlich wurden mehr als 3900 Wasserdampfprofile von einem flugzeuggetragenen Differentiellen-Absorptions-Lidar (DIAL) gemessen, das auf dem DLR Forschungsflugzeug Falcon 20 installiert war. Die vorliegende Arbeit befasst sich mit dem Einfluss dieser gezielten Dropsonden- und DIAL-Messungen auf die Vorhersagequalität des globalen Wettermodells des Europäischen Zentrums für Mittelfristige Wettervorhersage (EZMW).

Verschiedene Vorhersageexperimente wurden durchgeführt, um den Einfluss der Dropsonden auf die Zugbahnvorhersage der zwei wichtigsten tropischen Wirbelstürme während T-PARC, Sinlaku und Jangmi, zu analysieren. Die Verwendung der Dropsonden-Messungen bewirkt eine 15-prozentige Verringerung des mittleren 12- bis 120-stündigen Zugbahnfehlers gemittelt über die gesamte Periode von Sinlaku und Jangmi. Die Dropsonden werden des Weiteren, in Abhängigkeit ihrer Position relativ zum Sturm, in drei verschiedene Untergruppen aufgeteilt um zu untersuchen in welchem Gebiet zusätzliche Messungen den größten Nutzen für die Zugbahnvorhersage tropischer Stürme haben. Die größte Verbesserung der Zugbahnvorhersage bewirken Messungen, die in der näheren Umgebung, kreisförmig am Außenrand des Sturmes liegen. Im Gegensatz dazu zeigen Messungen in weiter vom Sturm entfernten Regionen, welche von Berechnungen mit singulären Vektoren als sensitiv eingestuft wurden, nur einen kleinen, aber leicht positiven Einfluss auf die Zugbahnvorhersage. Messungen im Zentrum des Wirbelsturmes führen zu großen Veränderungen der Analysefelder, aber nur zu sehr kleinen Verbesserungen der Vorhersage. In allen Experimenten werden besonders die zu den Zeitpunkten vor dem Eintreffen des Sturmes an der Küste und der darauffolgenden Umlenkung der Zugbahn gestarteten Vorhersagen durch die zusätzlichen Dropsonden-Messungen verbessert, während die positiven Auswirkungen nach der Umlenkung des Sturmes relativ gering sind.

Hochaufgelöste DIAL-Messungen der Wasserdampfkonzentration werden unter Verwendung des operationellen vier-dimensionalen variationellen Datenassimilationssystems in das Globalmodell des EZMW assimiliert. Das Assimilationssystem nutzt die in den DIAL-Messungen enthaltene Information und der Analysefehler, der mit unabhängigen Messungen von Dropsonden verifiziert wird, verringert sich durch die assimilierten DIAL-Messungen. Die Auswirkungen der Wasserdampfmessungen auf die Vorhersagequalität

sind in den meisten Fällen gering, wobei in zwei Fällen eine Verbesserung der Vorhersagequalität durch die DIAL-Messungen erzielt wird. Des Weiteren werden systematische Unterschiede zwischen den Wasserdampfmessungen des DIALs und der Dropsonden sowie dem Wasserdampf im Modell untersucht. Es zeigt sich, dass in der Troposphäre die DIAL-Messungen im Mittel etwa 7-10% trockener sind als die Modellwerte. Aus dem Vergleich zwischen den Messungen des DIALs und der Dropsonden lässt sich wiederum schließen, dass DIAL-Messungen zwar in der unteren Troposphäre zu trocken sind, nicht aber in höheren Schichten.

# Abstract

In the framework of the THORPEX Pacific Asian Regional Campaign (T-PARC) 2008, an unprecedented data set of airborne observations was sampled in the western North Pacific basin. About 1500 dropsondes were deployed by several aircraft, mainly during tropical cyclone surveillance missions. Additionally, a set of about 3900 water vapour profiles was measured by an airborne differential absorption lidar (DIAL) installed on-board the DLR Falcon 20 aircraft. The forecast influence of the adaptive dropsondes and DIAL humidity observations in the European Centre for Medium-Range Weather Forecasts (ECMWF) global model is addressed in this thesis.

Observing system experiments were performed to analyse the forecast influence of dropsonde observations for the two major T-PARC typhoon systems, Sinlaku and Jangmi. The assimilated dropsonde observations reduce the mean 12-120 h track forecast error in the period of Sinlaku and Jangmi by 15%. Further, the dropsonde observations were divided into three different subsets depending on their location relative to the tropical cyclone (TC) and sensitivity studies were carried out to investigate which observations are most beneficial for typhoon track forecasting. The largest TC track forecast improvements are found for observations in the vicinity of the storm, placed at a circular ring at the outer boundary of the TC. In contrast, observations in remote regions indicated to be sensitive by singular vectors seem to have a relatively small influence with a slight positive tendency on average. Observations in the TC core and centre lead to large analysis differences, but only very small mean forecast improvements. Forecasts initialised prior to landfall and recurvature are stronger influenced by additional dropsonde observations, while the observation impact on the track forecast after recurvature is relatively weak.

High-resolution DIAL humidity observations were assimilated into the ECMWF global model using the operational four-dimensional variational data assimilation system. The assimilation system is able to extract the information of DIAL observations and the verification with independent dropsonde observations shows a reduction of the analysis error when DIAL water vapour observations are assimilated. The forecast influence of the humidity observations is found to be small in most cases, but the observations are able to affect the forecast considerably under certain conditions. Systematic errors are investigated by comparison between humidity model fields, DIAL and dropsonde observations. Overall, DIAL observations are roughly 7-10% drier than model fields throughout the troposphere. Comparison with dropsonde observations suggests that the DIAL observations are too dry in the lower troposphere but not above.

Parts of this work are included in:

Harnisch, F. and M. Weissmann, 2010: Sensitivity of typhoon forecasts to different subsets of targeted dropsonde observations. *Mon. Wea. Rev.*, **138**, 2664-2680

Weissmann, M., F. Harnisch, C. Wu, P. Lin, Y. Ohta, K. Yamashita, Y. Kim, E. Jeon, T. Nakazawa, and S. Aberson, 2011: The influence of assimilating dropsonde data on typhoon track and mid-latitude forecasts. *Mon. Wea. Rev.*, **139**, 908-920

Harnisch, F., M. Weissmann, C. Cardinali, and M. Wirth, 2010: Experimental assimilation of DIAL water vapour observations in the ECMWF global model. *Quart. J. Roy. Meteor. Soc.*, accepted

# Chapter 1

## Introduction

### 1.1 Background

The time integration of a numerical weather prediction (NWP) illustrates an initial value problem (Kalnay, 2003). Bjerknes (1904) already stated more than 100 years ago that, in addition to having a model with a realistic representation of the atmosphere, one has to know the atmospheric state at a given time with sufficient accuracy to produce an accurate weather forecast.

The atmosphere is a nonlinear, chaotic and complex system, and the predictability of the atmospheric state is limited as both the NWP model and the initial conditions are sources of errors. In NWP models, errors arise due to our limited knowledge of governing laws of atmospheric physical processes as well as due to limited computer resources that make it necessary to use technical assumptions and simplifications. However, even if we would have a perfect model and unlimited computing resources, we would still face limits of predictability and would not be able to produce perfect forecasts as there are always errors that arise from imperfect initial conditions.

The importance of accurate initial conditions was highlighted by Lorenz (1963), who demonstrated in his famous experiments on predictability that the atmosphere can be highly sensitive to the choice of initial conditions. Small errors in the initial conditions may grow significantly during the forecast period, which can finally lead to an erroneous prediction of the atmospheric state.

In order to determine the initial conditions, observations of the state of the atmosphere are taken on a regular basis by a large number of different observational platforms and instruments. Figure 1.1 gives an overview of the current Global Observing System (GOS). The observation components of the GOS can be separated into six different groups: surface observations (e.g. synoptic observations), profile observations (e.g. radiosonde soundings),

marine observations (e.g. buoys), aircraft observations (e.g. Aircraft Meteorological Data Relay (AMDAR)), satellite observations (e.g. radiances) and other observational platforms (e.g. Doppler radars). The GOS provides of the order of  $10^8$  observations per day to determine the actual state of the atmosphere. Nevertheless, independent of the number of observations, gaps both in time and space always exist. Radiosonde observations for example, which measure the vertical structure of temperature, wind and humidity, are launched from distinct locations, mostly airports, and are only available a few times per day. To complete the observed picture of the atmosphere and produce accurate initial conditions, another source of background information about the atmospheric state is required. In the task of operational NWP, this background information is provided by a short-term forecast created by the NWP model. This merging process of observations and background information is called data assimilation, and aims to find the best possible initial conditions to initialise a model and generate weather forecasts.

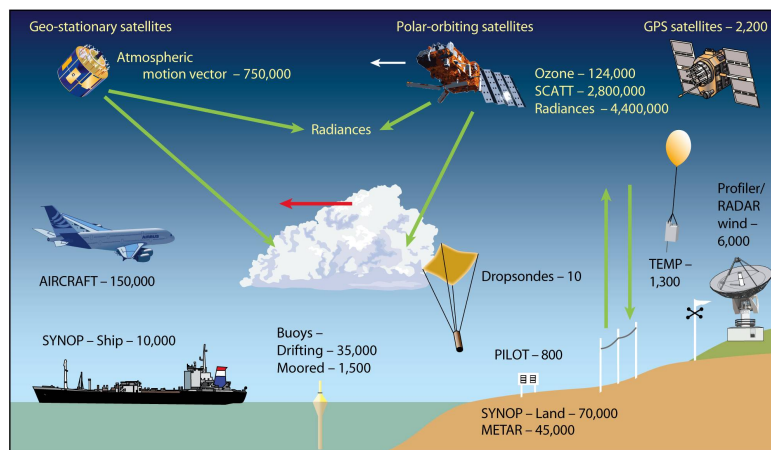


**Figure 1.1:** Overview of the Global Observing System. Figure taken from Hagedorn (2010).

Deficiencies of the GOS can generate errors in the initial conditions. Poor observational coverage for example limits the ability to correct the background information adequately with the information provided by observations. The concept of adaptive observing strategies (also called observation targeting) aims to tackle deficiencies in the observational network by deploying additional observations in areas, where they are most beneficial for the reduction of forecast errors. Adaptive observing strategies can be further applied to optimise the design of the future observing network in a way that maximises the improvements of observations for NWP and minimises the costs of instruments.

Adaptive observing strategies have been applied and tested in several field campaigns under the umbrella of The Observing System Research and Predictability Experiment (THORPEX). THORPEX is a 10-year programme within the World Weather Research

Programme (WWRP) of the World Meteorological Organization (WMO) and aims “to accelerate improvements in the accuracy of one-day to two-week high impact weather forecasts for the benefit of society, the economy and the environment”<sup>1</sup>. Therefore, one major focus of THORPEX are forecasts of tropical and extratropical cyclones, that can have a disastrous impact on society when predicted poorly. Forecast failures of high impact weather are often due to inaccurate or erroneous initial conditions (Rabier et al., 1996). After the start of THORPEX in 2002, the research in the field of adaptive observations has increased rapidly. One of the key issues is to evaluate how adaptive observations can be applied to achieve the largest benefits for the forecast quality. The research group Predictability and Dynamics Of Weather Systems in the Atlantic-European Sector (PANDOWAE<sup>2</sup>) is a German initiative contributing to THORPEX related research on the improvement of the forecast quality of high impact weather events. PANDOWAE consists of three different research areas dealing with upper-level Rossby wave trains, moist processes and diabatic Rossby waves, and ensembles and adaptivity.

The work of this thesis is part of the PANDOWAE project “Adaptive observing strategies for active airborne remote sensing instruments” that aims to:

- develop targeting strategies for future field campaigns and operational observations
- investigate the potential of new remote sensing instruments
- quantify the impact of airborne wind and water vapour lidar observations on the forecast skill of NWP models.

Data collected during the summer phase of the multi-national THORPEX Pacific Asian Regional Campaign (T-PARC<sup>3</sup>), that took place in the western North Pacific basin from August to October 2008, are analysed in this thesis to address the above listed PANDOWAE and THORPEX related research topics.

In T-PARC, a strong effort was made to bundle international research activities for extensive observations of tropical cyclones. The goals of the campaign were to enhance the understanding of the short- and medium-range dynamics of tropical cyclones (TCs) and to increase the forecast skill of high impact weather events related to TCs in the western North Pacific and their downstream impact in the eastern North Pacific and North America. An unprecedented set of observational platforms of up to four different research aircraft, in combination with driftsonde gondolas, research vessels and extra satellite observations was

---

<sup>1</sup>[http://www.wmo.int/pages/prog/arep/wwrp/new/thorpex\\_new.html](http://www.wmo.int/pages/prog/arep/wwrp/new/thorpex_new.html)

<sup>2</sup><http://www.pandowae.de>

<sup>3</sup><http://www.eol.ucar.edu/projects/t-parc/>

operated in the framework of T-PARC and collaborative projects. Systematic observations targeted around TCs during the full life cycle of a storm from the genesis in tropical waters throughout its northwestward movement, recurvature and extratropical transition (ET) were conducted.

## 1.2 Adaptive observations for tropical cyclones

TCs usually develop over tropical oceans which are data sparse. The limited number of observations and the rapid development of TCs increases uncertainties of the model analysis in these regions, which can lead to significant forecast errors (Langland, 2005a). However, accurate forecasts of these high impact weather events are extremely important to protect the increasing population in coastal areas worldwide.

The first regular adaptive observations for TC forecasts were conducted by the National Oceanic and Atmospheric Administration (NOAA) Hurricane Research Division (HDR) in the North Atlantic basin from 1982 to 1996. Assimilation of those observations of wind and thermodynamic profiles reduced the mean 12-60 h track forecast error by 16-30%, which was about the same size as the improvements in the operational forecast model over the years from 1970 to 1991 (Burpee et al., 1996). Following these promising results, surveillance programs deploying dropsonde observations in and around TCs have been operated for the Atlantic from 1997 onwards (Aberson, 2002). Despite the increased use of satellite data in the analysis of NWP models, the adaptive dropsonde measurements of key variables such as wind, temperature and humidity in the environment of TCs, still lead to mean improvements of 10-15% in the Atlantic and eastern North Pacific TC track forecasts of the National Centers for Environmental Prediction (NCEP) Global Forecasting System (GFS) within the critical watch and warning period before landfall (Aberson, 2010).

In the western North Pacific basin, a surveillance programme for adaptive TC observations, called Dropwindsonde Observations for Typhoon Surveillance near the Taiwan Region (DOTSTAR), started in 2003 (Wu et al., 2005). Similar to the Atlantic, several studies using the NCEP GFS and the Japan Meteorological Agency (JMA) models showed that dropsonde observations in the environment of TCs can lead to improvements of TC track forecasts of the order of 10-20% (Wu et al., 2007b; Yamaguchi et al., 2009).

To deploy additional observations in the most beneficial way, adaptive observing guidance based on the findings of different targeting techniques as singular vector (SV) calculations (Buizza and Palmer, 1995; Buizza and Montani, 1999; Peng and Reynolds, 2006; Reynolds et al., 2009), ensemble transform Kalman filter (ETKF) products (Bishop et al., 2001; Majumdar et al., 2002), ensemble deep-layer mean (DLM) wind variances (Aberson, 2003) and adjoint-derived sensitivity steering vector (ADSSV) calculations (Wu et al.,

2007a) have been used over the last few years. A detailed comparison of the different targeting techniques is given in Wu et al. (2009) for the western North Pacific basin and in Majumdar et al. (2006) and Reynolds et al. (2007) for the Atlantic. Sensitivity patterns captured by the different targeting techniques can be significantly different. Majumdar et al. (2006) and Wu et al. (2009) found that one targeting technique, for example SVs, shows similar sensitive regions independent of the model, while the similarity between adjoint-based methods (SV, ADSSV) and ETKF calculations is less distinct. The structural differences between the methods can be linked to the mathematical and physical differences in their calculations (Reynolds et al., 2007). The ETKF, which tends to distribute sensitivity around the storm centre, predicts the forecast error variance reduction from adaptive observations using ensemble forecast perturbations (Majumdar et al., 2002). In contrast, SV-based methods consider optimised perturbation growth and predict regions where changes in the initial analysis have the largest impact on the forecast (Peng and Reynolds, 2006). In addition to the storm itself, SVs often locate sensitivity in remote regions, which are associated with dynamical systems, such as for example the jet stream or an upstream midlatitude trough, that are expected to affect the movement and evolution of the TC (Peng and Reynolds, 2006; Reynolds et al., 2009; Wu et al., 2009).

Figure 1.2 shows an exemplary targeting guidance by six different techniques calculated for Typhoon Shanshan in 2006. At the observing time, the midlatitude flow affects the movement of the storm. The three different SV techniques (Figs. 1.2a-c) show increased sensitivity upstream and at the centre of the approaching midlatitude trough, while the ADSSV points only to the trough centre (Fig. 1.2e). The two ensemble-based methods (Figs. 1.2d,f) locate the maximum sensitivity right at the centre of Shanshan, but increased sensitivity can also be seen north of Shanshan downstream of the midlatitude trough. There is no overall consensus between different targeting methods and considering limited resources, it is essential to investigate where adaptive observations need to be deployed to receive the largest forecast impact.

More insight into how adaptive observations based on different targeting techniques influence the TC forecast is expected from conducting observing system experiments (OSEs) (Reynolds et al., 2007; Wu et al., 2009). For a single case of DOTSTAR dropsonde observations, Yamaguchi et al. (2009) demonstrated that the assimilation of dropsondes only in SV sensitive regions can reproduce most of the forecast improvements gained from the assimilation of all dropsondes. In an OSE study for Atlantic surveillance flights, promising forecast improvements were found when using only observations in sensitive regions indicated by different targeting techniques compared to using all available extra observations (Aberson et al., 2010). However, these studies were restricted to a limited sample size and considerable differences between various techniques were found. The adaptive obser-

#38 WP14Shanshan Ti=20060914 Ta=20060916

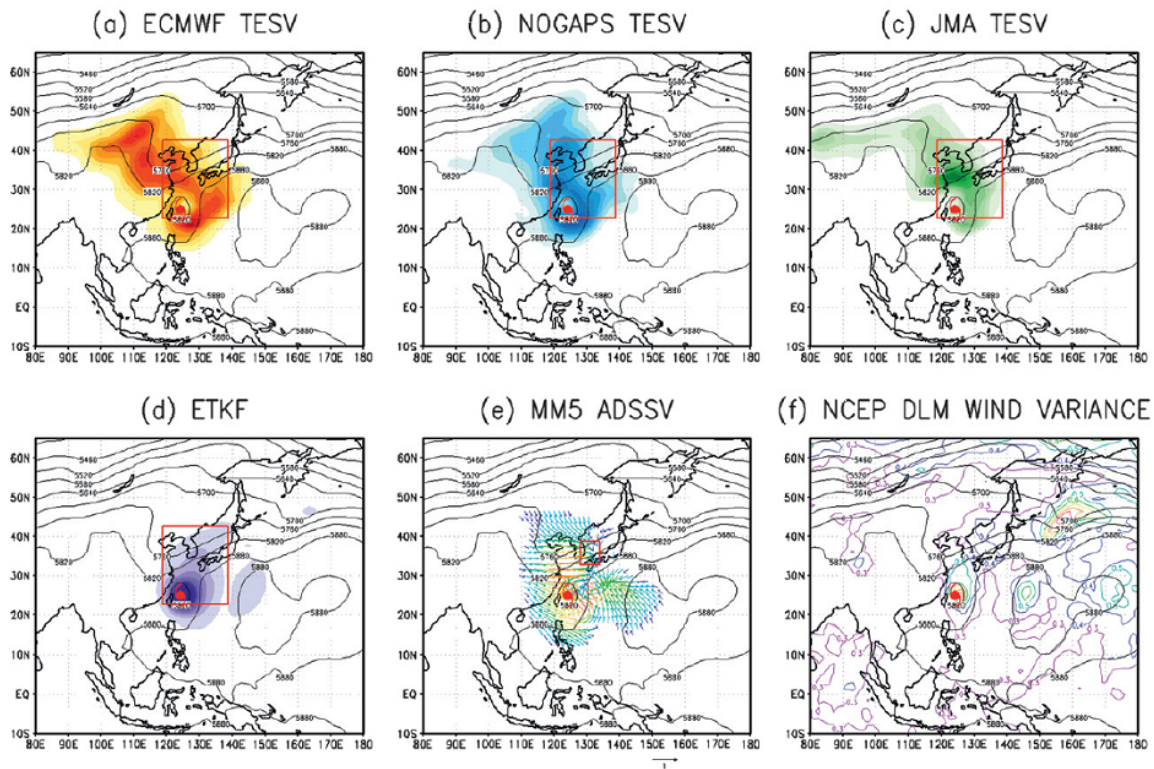


**Figure 1.2:** Example case of sensitivity guidance maps of (a) ECMWF<sup>4</sup> SV, (b) NOGAPS<sup>5</sup> SV, (c) JMA SV, (d) multimodel (ECMWF/NCEP/CMC<sup>6</sup>) ETKF, (e) MM5<sup>7</sup> ADSSV and (f) DLM wind variance valid for Typhoon Shanshan at 00 UTC 16 Sept 2006. The Joint Typhoon Warning Center (JTWC) best track position of Shanshan is displayed by a red typhoon symbol and the geopotential height at 500 hPa from the NCEP analysis is superimposed. The red box in (a)-(e) describes the target domain used for the sensitivity calculations. Figure taken from Wu et al. (2009).

vations sampled during T-PARC provide a promising data set to perform further OSEs to test the impact of observations in different targeting regions on the forecast of TCs. While DOTSTAR only could use the resources of one aircraft, adaptive observations for TCs in the western North Pacific basin were deployed from up to four research aircraft during T-PARC.

<sup>4</sup>European Centre for Medium-Range Weather Forecasts

<sup>5</sup>Navy Operational Global Atmospheric Prediction System

<sup>6</sup>Canadian Meteorological Center

<sup>7</sup>fifth-generation Pennsylvania State University / National Center of Atmospheric Research (NCAR) Mesoscale Model

## 1.3 Humidity observations by new observing systems

The knowledge of the global moisture distribution is an important ingredient for NWP, especially for the forecast of precipitation (Ebert et al., 2003; Keil et al., 2008). In addition, water vapour affects the atmospheric radiation balance and can also be responsible for the transport of energy that is stored in evaporated water and released again by condensation (Pierrehumbert, 2002).

Nevertheless, the current observational network used for the initialisation of NWP models lacks sufficient accurate, vertically resolved observations of humidity. The majority of atmospheric humidity observations are derived from passive satellite instruments such as the Atmospheric Infrared Sounder (AIRS), the Advanced Microwave Sounding Unit (AMSU-A, AMSU-B) sounders, the Infrared Atmospheric Sounding Interferometer (IASI), the High Resolution Infrared Sounder (HIRS), the Microwave Humidity Sounder (MHS), the Advanced Microwave Scanning Radiometer (AMSR-E) or the Special Sensor Microwave/Imager (SSM/I), which provide information on humidity indirectly by observing radiation emitted from the atmosphere. Global Positioning System (GPS) radio occultation techniques (Healy and Thépaut, 2006), GPS ground-based measurements of slant total delay (Zus et al., 2008) or zenith total delay (Poli et al., 2007) are another source of humidity information. High vertical resolution, but poor horizontal and temporal coverage is achieved with radiosonde humidity observations, while ground stations provide observations only near the surface.

The assimilation of humidity observations in NWP models is an active field of ongoing research. Bengtsson et al. (2004) found that even without any humidity observations the European Centre for Medium-Range Weather Forecasts (ECMWF) 40-yr reanalysis (ERA40) system is able to reproduce the hydrological cycle by the time evolution of wind, temperature and surface pressure. They further conducted forecast experiments showing limited impact of humidity observations on the forecast skill of dynamical fields (Bengtsson and Hodges, 2005). In contrast, Andersson et al. (2007) demonstrated that the analysis and the forecast of humidity, mass and wind fields of the ECMWF model benefits from humidity observations. They concluded that the ECMWF four-dimensional variational (4D-Var) data assimilation system and the improved formulation of the background error covariance model for humidity (Hólm et al., 2002) contributed to the positive results, whereas Bengtsson and Hodges (2005) used the less advanced ERA40 3D-Var system.

In recent years, active remote sensing techniques such as differential absorption lidars (DIALs) were developed and tested during several field experiments. DIAL systems demonstrated the ability to supply precise humidity observations with high spatial and temporal resolution (e.g. Browell et al., 1998; Wulfmeyer and Bösenberg, 1998; Ehret et al., 1999;

Bruneau et al., 2001; Kiemle et al., 2008; Wirth et al., 2009). A detailed evaluation of different airborne water vapour DIAL systems was performed within the framework of the International H<sub>2</sub>O Project (IHOP\_2002). The comparison of observations from ground-based lidar systems and different airborne DIAL systems showed an agreement with inter-instrumental biases smaller than 10% (Behrendt et al., 2007a, 2007b). DIAL observations were also used to derive latent heat flux profiles for boundary layer studies by using collocated wind observations (Kiemle et al., 2007). A case study demonstrated improvements of convective initiation and quantitative precipitation forecasts by assimilating Lidar Atmospheric Sensing Experiment (LASE) observations in a mesoscale model (Wulfmeyer et al., 2006). For forecasts of tropical cyclones using the Florida State University global spectral model, a beneficial influence was discovered with the assimilation of LASE humidity observations (Kamineni et al., 2003, 2006; Biswas and Krishnamurti, 2008).

All these previous studies were performed with two-wavelengths DIAL systems. In support of a mission proposal to the European Space Agency (ESA) for the Water Vapour Lidar Experiment in Space (WALES) (Gérard et al., 2004), the first airborne four-wavelength DIAL was recently developed (Wirth et al., 2009) to investigate the feasibility of operating an active profiling DIAL system in space. The nadir-pointing WALES demonstrator was deployed during the Convective and Orographically-induced Precipitation Study (COPS) and the European THORPEX Regional Campaign (E-TReC) in 2007. DIAL humidity observations from these campaigns were compared to ECMWF model fields of humidity (Schäfler et al., 2011a) and were used in an intercomparison study together with other lidar humidity observations (Bhawar et al., 2011).

During T-PARC, the nadir-pointing WALES demonstrator was installed on-board the Deutsches Zentrum für Luft- und Raumfahrt (DLR) research aircraft Falcon and observed more than 3900 water vapour profiles. These high-resolution humidity observations provide a unique data set to study the potential of this new remote sensing instruments for NWP.

## 1.4 Goals and outline

This study intends to evaluate the impact of adaptive T-PARC observations on the forecast performance of the ECMWF model. The thesis consists of three main parts. The first part evaluates the overall impact of more than 1500 dropsondes released during T-PARC on TC forecasts and OSEs with the operational ECMWF model are performed. In the second part, OSEs are conducted for single case studies and different strategies to optimise TC forecasts improvements with airborne dropsondes observations are compared. Particular emphasis is given to the question, in which regions relative to the TC additional dropsondes are most beneficial for the forecast performance to shed further light on the problem where

to deploy adaptive observations considering limited flight time and operational costs. In the third part of the thesis, the potential of new remote sensing observations by an airborne DIAL system for NWP is investigated. Sensitivity studies assimilating DIAL observations during T-PARC are conducted with the ECMWF 4D-Var data assimilation system to examine how the information of those observations can be used optimally. Furthermore, OSEs are performed to explore the influence of the DIAL observations on the analysis and forecast quality.

To summarise, the scientific questions addressed in this thesis are:

- What is the influence of adaptive T-PARC dropsonde observations on tropical cyclone forecasts?
- Where do adaptive dropsonde observations show the largest benefit for tropical cyclone forecasts?
- What is the potential of new types of observations such as water vapour DIAL observations for NWP?

Chapter 2 describes the methods and data used in this thesis. Basic principles of data assimilation are explained and the ECMWF analysis and forecasting system is introduced. Furthermore, the concept of adaptive observations is summarised and the setup of OSEs is presented. Dropsonde and DIAL observations during T-PARC provide the main data set of this study and the two observing systems are explained. In Chapter 3 the overall impact on TC track forecasts of all additional T-PARC dropsonde observations is addressed by the analysis of OSEs. In addition, the effect of an erroneous dropsonde observation time is examined. An evaluation of different TC observing strategies is given in Chapter 4. Dropsonde observations are divided into three different groups depending on their location relative to the storm to test the forecast influence of observations in different areas. Chapter 5 describes the assimilation experiments using DIAL observations and investigates systematic errors of the model and DIAL observations. The overall analysis and forecast influence is presented together with a case study where the influence of DIAL observations is investigated in detail. Finally, the main conclusions of this thesis together with a brief outlook are summarised in Chapter 6.



# Chapter 2

## Methods and data

This chapter presents the methods and data which are applied to answer the proposed research questions. Section 2.1 gives an introduction to data assimilation. Basic principles and the incremental solution method, which are used in the ECMWF variational data assimilation system, are presented. In section 2.2, the detailed specifications of the ECMWF analysis and forecasting system and the used model setup, which is generally similar to the operational one, can be found. The ECMWF model, that uses a modern 4D-Var data assimilation system to assimilate millions of observations, can be considered as one of the best available global NWP models which is confirmed by the latest forecast verification statistics that show the continuously increasing high quality of the ECMWF model forecasts (Fiorino, 2009; Richardson et al., 2009). More informations on the observation targeting process, its application and known problems are illustrated in section 2.3. OSEs are a frequently used tool to evaluate the forecast influence of adaptive or targeted observations (e.g. Irvine et al., 2009) and the general configuration of the performed OSEs and the applied forecast verification metrics are presented in section 2.4. The analysed adaptive airborne observations were collected within the framework of T-PARC. The aims of the campaign, the main observational platforms and an exemplarily observational highlight are presented in section 2.5. Section 2.6 gives a description of the dropsonde system followed by an introduction of the DIAL technique and specifications of the Falcon airborne DIAL system in section 2.7. The observational resources of T-PARC were unprecedented and a high coverage with dropsonde observations as well as with high-resolution DIAL humidity observations was achieved in the western North Pacific basin.

## 2.1 Data assimilation

Modern data assimilation systems aim to find the best possible initial conditions to initialise a NWP model. Accurate initial conditions are produced by a combination of observations and a priori background information. The background information is usually provided by a short-range forecast initialised from the previous analysis cycle. A schematic of such an intermittent data assimilation cycle is shown in Fig. 2.1.

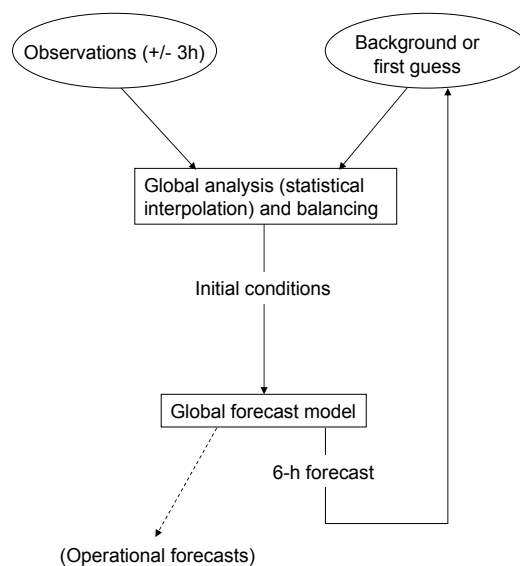


**Figure 2.1:** Sketch of an intermittent data assimilation cycle. Figure adapted from Kalnay (2003).

Data assimilation methods can be based on simple concepts as e.g. interpolation of observations, or apply statistical estimation theory to combine observations and background information in a statistically optimal way. A state-of-the-art assimilation scheme that uses statistical information is the 4D-Var data assimilation, which is commonly used in NWP models at various international weather centres (e.g. ECMWF, MeteoFrance, JMA, CMC).

### 2.1.1 Variational approach

The variational approach, which is based on statistical estimation theory, aims to find the most likely analysis by combining all observations and background information under consideration of their error variances. The variational approach assumes that the background and observation errors are Gaussian distributed with known error variances  $\sigma_b^2$  and  $\sigma_o^2$ , respectively, and that both errors are uncorrelated.

The following example, adapted from Kalnay (2003), describes the principle of the variational approach to find the best estimate of any scalar  $x$  using the observation  $y$  and the background information  $x_b$ . The probability of observing  $y$ , given the true value of  $x$  and the observation error variance  $\sigma_o^2$ , is expressed by the Gaussian distribution

$$p_{\sigma_o}(y | x) = \frac{1}{\sqrt{2\pi}\sigma_o} e^{-\frac{(y-x)^2}{\sigma_o^2}} = L_{\sigma_o}(x | y)$$

which is equal to the likelihood  $L$  of a true value  $x$  given an observation  $y$  with an observation error variance  $\sigma_o^2$ . The likelihood  $L$  for a true value  $x$ , given the background  $x_b$  and the background error variance  $\sigma_b^2$ , can be derived analogue. Multiplying both distributions results in the joint probability or joint likelihood

$$L_{\sigma_b\sigma_o}(x | x_b, y) = p_{\sigma_b}(x_b | x) p_{\sigma_o}(y | x) = \frac{1}{2\pi\sigma_b\sigma_o} e^{-\frac{(x_b-x)^2}{\sigma_b^2} - \frac{(y-x)^2}{\sigma_o^2}}. \quad (2.1)$$

The maximum of the joint probability is the most likely value of  $x$ , given the independent values of the observation  $y$  and the background  $x_b$  and their related error variances. Since the logarithm is a monotonic function, the value of  $x$  that maximises  $L_{\sigma_b\sigma_o}(x | x_b, y)$  (Eq.2.1) also maximises the logarithm of the joint likelihood

$$\max_x \log L_{\sigma_b\sigma_o}(x | x_b, y) = \max_x \left[ \text{const.} - \frac{(x_b - x)^2}{\sigma_b^2} - \frac{(y - x)^2}{\sigma_o^2} \right].$$

The value of  $x$  which minimises a cost function  $J$ , defined as

$$J(x) = \frac{(x_b - x)^2}{\sigma_b^2} + \frac{(y - x)^2}{\sigma_o^2}, \quad (2.2)$$

maximises the joint probability (Eq. 2.1). The minimum of the cost function  $J$  is found by taking the partial derivative with respect to  $x$  and setting it equal to zero:

$$\frac{\partial J}{\partial x} = 0 = -2\frac{(x_b - x)}{\sigma_b^2} - 2\frac{(y - x)}{\sigma_o^2}.$$

This results in

$$x = \frac{1}{\frac{1}{\sigma_b^2} + \frac{1}{\sigma_o^2}} \left( \frac{x_b}{\sigma_b^2} + \frac{y}{\sigma_o^2} \right),$$

which is the best estimate of  $x$  using information of the background  $x_b$ , the observation  $y$  and their error variances  $\sigma_b^2$  and  $\sigma_o^2$ , respectively.

The variational approach can be extended to three-dimensions with the cost function

$J$  now written as

$$J(\mathbf{x}) = \frac{1}{2}(\mathbf{x} - \mathbf{x}_b)^T \mathbf{B}^{-1}(\mathbf{x} - \mathbf{x}_b) + \frac{1}{2} [\mathbf{y} - H(\mathbf{x})]^T \mathbf{R}^{-1} [\mathbf{y} - H(\mathbf{x})] \quad (2.3)$$

similar to the one-dimensional (1D) case (Eq. 2.2). The vector  $\mathbf{x}$  ( $\mathbf{x}_b$ ) of length  $m$  describes the 3D model state (model background state), and the vector  $\mathbf{y}$  of length  $p$  includes all observations. Instead of the 1D error variances  $\sigma_b^2$  and  $\sigma_o^2$ , the cost function for the 3D case uses the background error covariance matrix  $\mathbf{B}$  ( $m \times m$ ) and the observation error covariance matrix  $\mathbf{R}$  ( $p \times p$ ). The observation operator  $H$  transforms the model variables  $\mathbf{x}$  into the observation space. The 3D variational (3D-Var) cost function is represented by two terms. The first one ( $\mathbf{x} - \mathbf{x}_b$ ) penalises the difference of the solution to the background and the second one ( $\mathbf{y} - H(\mathbf{x})$ ) accounts for the misfit between the solution and the observations (Kalnay, 2003). The 3D-Var solution is a global model state  $\mathbf{x}$  that minimises the cost function  $J$  using all available observations  $\mathbf{y}$  simultaneously. This solution is called the analysis state  $\mathbf{x}_a$ .

The 3D-Var cost function does not consider the time of the observation and it is assumed that all observations are taken simultaneously. There are many state-of-the-art observing systems as for examples satellites that perform continuous measurements. 4D-Var data assimilation also includes time as additional variable and all observations are used at their correct time. The 4D-Var cost function can be written as (Kalnay, 2003)

$$J[\mathbf{x}(t_0)] = \frac{1}{2} [\mathbf{x}(t_0) - \mathbf{x}_b(t_0)]^T \mathbf{B}^{-1} [\mathbf{x}(t_0) - \mathbf{x}_b(t_0)] + \frac{1}{2} \sum_{i=0}^N [\mathbf{y}(t_i) - H_i[\mathbf{x}(t_i)]]^T \mathbf{R}_i^{-1} [\mathbf{y}(t_i) - H_i[\mathbf{x}(t_i)]] \quad (2.4)$$

with the observation vector  $\mathbf{y}(t_i)$ , the model state vector  $\mathbf{x}(t_i)$ , the observation operator  $H_i$  and the observation error covariance matrix  $\mathbf{R}_i$  as function of the time  $t_i$  with  $i = 0, 1, \dots, N$ . An assimilation window has to be defined in 4D-Var which spans from time  $t_0$  to  $t_N$  and includes all observations  $\mathbf{y}(t_i)$  within this window. The length of the assimilation window typically ranges from 6 to 12 hours. The consideration of the time variable requires to explicitly include the forecast model in the data assimilation:

$$\mathbf{x}(t_i) = M_{i,0} [\mathbf{x}(t_0)].$$

The model state  $\mathbf{x}(t_0)$  at time  $t_0$  is evolved to time  $t_i$  with the nonlinear forecast model  $M_{i,0}$  within the assimilation window. Rather than finding a solution at one time that minimises the cost function as it is done in 3D-Var, 4D-Var tries to find a model trajectory

that minimises the cost function within the assimilation window. This so called strong-constraint 4D-Var also implies that the nonlinear forecast model is assumed to be ‘perfect’, i.e. that the model has no errors.

A crucial part of the cost function is the appropriate formulation of the background error covariance matrix  $\mathbf{B}$ . The role of  $\mathbf{B}$  is to spread out the information of the observations and to provide statistically consistent increments (i.e. difference between the analysis and background model state) at neighboring grid points and levels of the model. Furthermore, physical properties have to be considered in a way that dynamically balanced and consistent increments of all variables are produced. For example, geostrophic balance is usually included as constraint. The true  $\mathbf{B}$  and the error statistics of the background are unknown and even in case  $\mathbf{B}$  would be known exactly, the dimensions ( $\sim 10^7 \times 10^7$ ) are by far too large to work with the matrix directly. Thus, an approximate surrogate of  $\mathbf{B}$  with known error statistics has to be modelled, which for example can be done by taking differences between short-range forecasts verifying at the same time (Parrish and Derber, 1992) or using an ensemble of analyses (Fisher, 2003).

Additionally, the observation error covariance matrix  $\mathbf{R}$ , which determines the weight of the observations, has to be specified considering three different types of errors: the observing instrument error, the representativeness error of the observation and errors in the design of the observation operator  $H$ . The observation operator  $H$  transforms the model variables from model space to observation space and enables a direct use of observations of non-model variables such as brightness temperature observed by satellites. This operator may include simple interpolation steps as well as complicated radiative transfer models for satellite measurements.

### 2.1.2 Incremental 4D-Var

The cost function  $J$  (Eq. 2.4) of the above discussed strong-constraint 4D-Var problem can be solved using an incremental approach (Courtier et al., 1994). The forecast model  $M$  and the observation operator  $H$  in the cost function can both be nonlinear. The linearisation of these two operators yields a quadratic cost function  $J$  and at the same time the gradient of the cost function  $\nabla J$  is linearly dependent to the control variables.

A model state  $\mathbf{x}(t_0)$  at time  $t_0$  is linearised about the model background state  $\mathbf{x}_b(t_0)$  by introducing a small increment  $\delta\mathbf{x}(t_0)$ . If the Taylor expansion is applied and terms higher than second order are neglected, the time evolved model state  $\mathbf{x}(t_i)$  becomes

$$\mathbf{x}(t_i) = M_{i,0}[\mathbf{x}(t_0)] = M_{i,0}[\mathbf{x}_b(t_0) + \delta\mathbf{x}(t_0)] \approx M_{i,0}[\mathbf{x}_b(t_0)] + \mathbf{M}_{i,0}\delta\mathbf{x}(t_0)$$

using the full nonlinear model  $M_{i,0}$  and a linearised model  $\mathbf{M}_{i,0}$ , the so-called tangent-

linear model. Hence, the approximate cost function  $J$  in the incremental 4D-Var data assimilation as function of the increment at initial time  $\delta\mathbf{x}(t_0)$  (Courtier et al., 1994) can be written as

$$J[\delta\mathbf{x}(t_0)] = \frac{1}{2} [\delta\mathbf{x}(t_0)]^T \mathbf{B}^{-1} [\delta\mathbf{x}(t_0)] + \frac{1}{2} \sum_{i=0}^N [\mathbf{d}(t_i) - \mathbf{H}_i \mathbf{M}_{i,0} \delta\mathbf{x}(t_0)]^T \mathbf{R}_i^{-1} [\mathbf{d}(t_i) - \mathbf{H}_i \mathbf{M}_{i,0} \delta\mathbf{x}(t_0)] \quad (2.5)$$

including a linearised observation operator  $\mathbf{H}_i$  and the innovation vector  $\mathbf{d}(t_i)$  defined as

$$\mathbf{d}(t_i) = \mathbf{y}(t_i) - H_i [M_{i,0} [\mathbf{x}_b(t_0)]] . \quad (2.6)$$

The innovation vector is calculated from the difference in observation space between the observation vector and the nonlinear forecast trajectory of the model initialised from the background model state at initial time  $\mathbf{x}_b(t_0)$ . The increment  $\delta\mathbf{x}(t_0)$  that minimises the cost function  $J$  (Eq. 2.5) is derived from the solution of

$$\nabla J = \mathbf{B}^{-1} \delta\mathbf{x}(t_0) + \sum_{i=0}^N \mathbf{M}_{i,0}^T \mathbf{H}_i^T \mathbf{R}_i^{-1} [\mathbf{d}(t_i) - \mathbf{H}_i \mathbf{M}_{i,0} \delta\mathbf{x}(t_0)] = 0 . \quad (2.7)$$

The transpose of the tangent-linear model  $\mathbf{M}_{0,i}^T$  (called the adjoint model) is required to minimise the cost function  $J$  (Eq. 2.7). The different tasks of the three model versions are sketched in Fig. 2.2. The full model state  $\mathbf{x}(t_0)$  is evolved forward in time by the nonlinear model  $M_{i,0}$  and the innovation vector is calculated from the difference of the nonlinear model trajectory and the observation vector. For each time step of the minimization the increment  $\delta\mathbf{x}(t_i)$  is integrated forward in time from  $t_i$  to  $t_{i+1}$  applying the tangent-linear model  $\mathbf{M}_{i+1,i}$  and backward in time from  $t_{i+1}$  to  $t_i$  using the adjoint model  $\mathbf{M}_{i+1,i}^T$ .

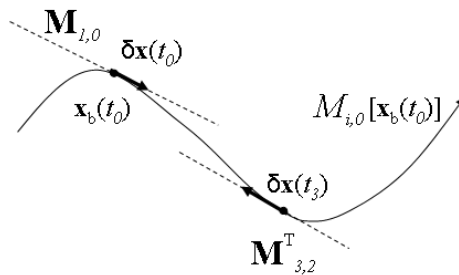


**Figure 2.2:** Nonlinear, tangent-linear and adjoint model.

The process of finding an increment  $\delta\mathbf{x}(t_0)$  that solves Eq. 2.7 is done in an iterative way using about 10 to 100 iterations. The resulting analysis increment  $\delta\mathbf{x}(t_0)$  is added to the model background state  $\mathbf{x}_b(t_0)$  to get the associated model analysis state. The solution is only accurate if the analysis increment is small which means that the analysis state is not too far away from the background state. The solution in the strong-constraint 4D-Var data assimilation is an exact model trajectory since it is assumed that the model has no errors. Hence, all increments in the assimilation window can be obtained by applying the nonlinear forecast model  $M_{i,0}$  to the increment  $\delta\mathbf{x}(t_0)$  at the beginning of the assimilation window.

## 2.2 ECMWF analysis and forecasting system

An intermittent, incremental 4D-Var data assimilation system is used operationally in the ECMWF system since 1997 (Bouttier and Rabier, 1998). The short-term model forecast acts as background state and about 10 million observations are assimilated every 12 hours to correct the approximately 80 million values of the model background state. Twice a day at 00 and 12 UTC, a 10-day model forecast is started from the produced analysis state which is considered as the best possible representation of the real atmosphere.

The ECMWF 4D-Var data assimilation solves an incremental formulation of the cost function  $J$  (Rabier et al., 2000), which is identical to Eq. 2.5. The increments at initial time  $\delta\mathbf{x}(t_0) = \mathbf{x}(t_0) - \mathbf{x}_b(t_0)$  are formulated with respect to the model background state  $\mathbf{x}_b(t_0)$ , which is provided by a short-term model forecast initialised at the previous analysis time. The 4D-Var system uses half-hour time slots within the 12-hourly assimilation windows between 21-09 UTC and 09-21 UTC for the nominal analysis times at 00 UTC and 12 UTC, respectively.

Figure 2.3 displays a schematic of the incremental ECMWF 4D-Var data assimilation system. The incremental approach allows the use of different horizontal resolutions for the comparison of the observations with the model background state (Eq. 2.6) and the minimisation of the cost function (Eq. 2.7). At first, the innovation vector is computed comparing the observations with the high-resolution nonlinear model state. The observation operator and the forecast model are linearised around the model background state. The minimisation of the cost function and the calculation of the increment  $\delta\mathbf{x}$  is done with a reduced model resolution using the linearised version of the forecast model (tangent-linear model), the adjoint model and the linearised observation operator  $\mathbf{H}_i$ . The high-resolution nonlinear model state is updated with the computed increment ( $\mathbf{x}_{i+1} = \mathbf{x}_i + S^{-1}(\delta\mathbf{x})$ ), the analysis is re-linearised and the next minimisation is performed. In the used setup, the nonlinear model runs at the resolution of T<sub>L</sub>799L91, i.e. truncation after wave number

799 ( $\sim 25$  km horizontal grid scale) and 91 vertical level, and is updated three times by increments computed at the resolution of  $T_L 95L91$ ,  $T_L 159L91$  and  $T_L 255L91$ , respectively.

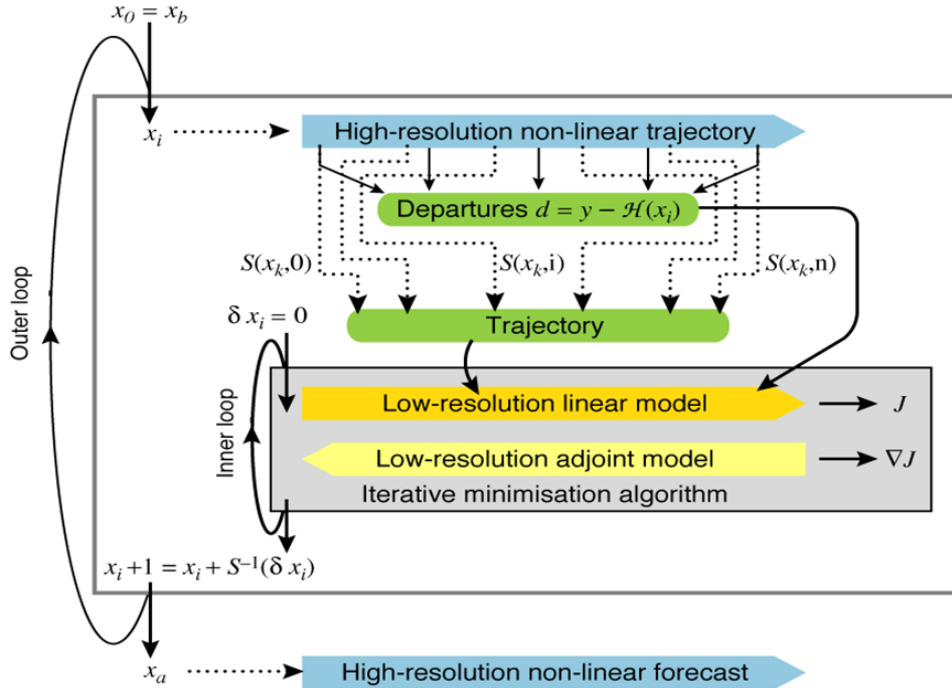


**Figure 2.3:** Schematic of the incremental ECMWF 4D-Var solution algorithm. The first ‘outer loop’ is initialised by the high-resolution (in this study  $T_L 799L91$ ) background model state  $\mathbf{x}_b$ . The iterative solution of the cost function is done in the ‘inner loop’ at a reduced resolution applying the tangent-linear model and its adjoint version. The high-resolution nonlinear model state is updated with the computed increment followed by the next ‘outer loop’. In the current setup three ‘outer loops’ are carried out to get the final analysis state  $\mathbf{x}_a$ .  $S$  denotes the truncation operator. Figure taken from Isaksen (2010).

## Observation processing

Different observation processing steps are carried out before the observations are assimilated. A thinning of the observations is conducted to avoid an oversampling of densely observed areas and to minimise the occurrence of correlated observation errors. Afterwards systematically erroneous or questionable data are excluded using a ‘blacklist’. The ‘blacklists’ are updated on a regular basis several times a year. Data omitted by the thinning and blacklisting steps are monitored passively during the assimilation procedure.

A screening of the observations is performed prior to the main analysis. The difference of the observations compared to the model background state, called background departure (identical to the innovation vector (Eq. 2.6)), is computed. In the background quality control check (BgQC) (Järvinen and Undèn, 1997) observations are rejected if the square of their background departure exceeds its expected variance by more than a predefined multiple  $\alpha$ . For one scalar element  $d$  of the innovation vector  $\mathbf{d}(t_i)$ , the observation gets ‘flagged’ by the BgQC if

$$\|d\| > \alpha \sqrt{\sigma_o^2 + \sigma_b^2}. \quad (2.8)$$

Different flags are assigned to different thresholds of  $\alpha$ : flag 1 to probably correct observations, flag 2 to probably incorrect observations and flag 3 to incorrect observations. Exemplary thresholds of  $\alpha$  for humidity observations are  $\alpha = 3$  (flag 1),  $\alpha = 4$  (flag 2) and  $\alpha = 5$  (flag 3). Only observations with flag 1 or without any flag are assimilated.

During the minimisation process, a variational quality control (VarQC) procedure (Andersson and Järvinen, 1999) is applied, where the cost function is modified by reducing the weight of the observations with large innovations. The VarQC procedure does not irrevocably reject observations and the weight of observations can change between different minimisation steps.

For a more detailed description of the ECMWF assimilation system and observation processing see Rabier et al. (2000), Mahfouf and Rabier (2000), Klinker et al. (2000), and Bauer et al. (2010).

## Forecasting system

The ECMWF global atmospheric model is a hydrostatic model. Upper-air variables are formulated spectrally based on spherical harmonics. Model forecasts used in this thesis are computed at a spectral resolution of  $T_L799$ . The atmosphere is divided into 91 vertical levels (L91) from the ground up to 0.01 hPa. The vertical hybrid coordinate follows the terrain in the lowest parts of the atmosphere where also the highest density of layers is found and shows a smooth transition to levels identical to isobaric surfaces in the upper troposphere and above. The general circulation model consists of three major components: a dynamical part, a physical part and a coupled ocean wave part. Physical processes and surface variables are considered on a reduced Gaussian grid. A parametrisation package is included to model radiative transfer, turbulent mixing, subgrid-scale orographic drag, moist convection, clouds, as well as surface and soil processes. Finally, a wave model is coupled to the atmospheric model to correctly represent the interaction between atmosphere and ocean. In the operational setup, a 10-day model forecast is initialised twice a day at 00 UTC and 12 UTC. Prognostic atmospheric model variables are wind, temperature,

humidity, cloud fraction, cloud water content, cloud ice content, ozone mass mixing ratio, and pressure at surface grid points. For more details on the ECMWF forecasting system see Persson and Grazzini (2007).

## 2.3 Observation targeting

Observation targeting is the process of determining regions in which the assimilation of additional observations is expected to maximally improve the forecast (Thorpe and Petersen, 2005). Those regions identified during the observation targeting process are called target regions or sensitive regions, while the observations in those target regions are named targeted or adaptive observations. Langland (2005a) stated that target regions should fulfil three general conditions. First, a high probability for a large or a fast-growing analysis error has to be present. Second, the analysis error has to be detectable by the additional targeted observations, and third, the analysis error can be corrected by the assimilation of targeted observations. After the reduction of the analysis error with targeted observations, a subsequent reduction of the forecast error is expected.

A schematic sketch of the observations targeting concept is illustrated in Fig. 2.4. To identify target regions, a forecast lead time and verification region have to be determined first. By definition, the forecast error within the verification region is expected to be reduced maximally at the defined forecast lead time by assimilating observations in sensitive areas.

Several objective procedures based on different mathematical methods are able to identify target regions. The most widely-used techniques are adjoint or ensemble methods which both include linear assumptions and assume that linear processes play an important role for the propagation of the effect of targeted observations (Szunyogh et al., 2002). While the adjoint-based SVs focus on finding analysis perturbations which represent fastest growing analysis errors in a tangent-linear framework (e.g. Buizza and Montani, 1999; Peng and Reynolds, 2006), the ETKF uses a linear combination of ensemble forecasts to evaluate the expected forecast error reduction resulting from a localised analysis error reduction due to targeted observations (e.g. Bishop et al., 2001; Majumdar et al., 2002). Further, adjoint-based calculations are used to compute the sensitivity of forecast errors to initial conditions (e.g. Rabier et al., 1996; Pu et al., 1997), to identify the most valuable observations by estimating their impact on the forecast error (e.g. Langland and Baker, 2004) or to determine the forecast sensitivity to dynamical structures in the initial conditions (Wu et al., 2007b).

For the case selection of observation targeting, weather events of interest have to be identified. Typical events are those that are expected to have a high impact on the society

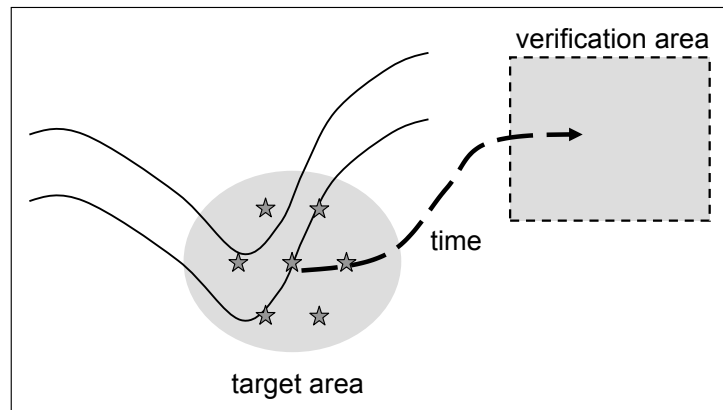


**Figure 2.4:** Schematic illustration of the concept of observation targeting. The target area is the region, where targeted observations (indicated as grey asterisks) are expected to be most beneficial for the forecast within the verification region after a certain forecast lead time. Solid lines mark possible streamlines representing the midlatitude flow.

and also exhibit considerable forecast uncertainty (e.g. indicated by increased ensemble spread). To date, observation targeting has mainly been applied to forecasts of extratropical and tropical cyclones at lead times of 1-3 days.

Observation targeting in midlatitudes was first discussed publicly at a workshop in 1995 (Snyder, 1996) and has been introduced and tested in a number of field experiments. The first one was the 1997 Fronts and Atlantic Storm-Track Experiment (FASTEX; Joly et al., 1999) followed by the NORth-Pacific Experiment (NORPEX; Langland et al., 1999). These experiments lead to the Winter Storm Reconnaissance (WSR) field programme with experiments in 1999 and 2000 (Szunyogh et al., 2000, 2002). WSR 1999 and WSR 2000 demonstrated that targeted observations, dropsondes in this case, are a practical way to improved severe winter storm forecasts over the continental United States (Szunyogh et al., 2002). Based on these findings the WSR programme was implemented operationally in 2001. Within the framework of THORPEX, a series of regional campaigns such as the Atlantic THORPEX Regional Campaign (A-TReC) in 2003 (Langland, 2005b; Petersen and Thorpe, 2007) and E-TReC in 2007 were performed which addressed various issues of observation targeting (Rabier et al., 2008).

The potential of adaptive observations for TCs was tested first in 1982, when the NOAA Hurricane Research Division sent out aircraft to enhance the number of observations in the environment of a hurricane threatening the United States (Burpee et al., 1984). A large area around the storm was defined as target region and no specific sensitive area

calculations were applied. Until 1996, 20 missions were conducted and the deployed additional observations led to 16-30% improvements of the official hurricane track forecasts (Burpee et al., 1996). From 1997, operational surveillance flights were carried out to deploy targeted observations whenever hurricanes were threatening the continental United States, Puerto Rico, and the Virgin Islands (Aberson and Franklin, 1999). Based on the significant track forecast improvements (10-15% within the critical watch and warning period before landfall) during the first 10 years of the surveillance flights (Aberson, 2010), the programme is still continuing. Motivated by the positive results found for Atlantic TCs, a similar operational surveillance programme called DOTSTAR was established for the western North Pacific in 2003 to collect targeted observations whenever TCs threaten Taiwan (Wu et al., 2005). The implementation of DOTSTAR led to a 10-20% reduction of the mean 12-120 hour track forecast error of the NCEP GFS model in the years 2003-2009 (Wu et al., 2007b; Chou et al., 2010). The combination of DOTSTAR and T-PARC in 2008 made it possible to perform a large number of observation targeting flights in the western North Pacific for TCs as well as for the ET of TCs which can have a major effect on the forecast error downstream over the United States.

Dropsondes launched from aircraft within target regions have been the classical, most widely-used type of targeted observations during the last years. However, observation targeting can also be applied to the operational observing network to optimise the use of already available observations and select the most valuable data. Studies based on this concept especially aim at to optimise the use of extensive satellite data sets. To date, a large quantity of satellite observations are discarded because of computational constraints. Possible options for the optimal selection of satellite data are to increase the sampling frequency of satellite observations within target regions (Dando et al., 2007; Bauer et al., 2011), to adjust the channel selection of satellite instruments (Fourrié and Rabier, 2004) or to increase the temporal resolution of wind observations derived from atmospheric motion vectors (AMVs) (Velden et al., 2005; Langland et al., 2009).

In theory, the concept of observation targeting is ideal in a way that forecast errors can be reduced by collecting a small number of extra observations in specified regions. In practice however, there are limitations to the observation targeting process and several issues emerged in recent years (Langland, 2005a). Langland (2005a) pointed out that observation targeting leads to an average improvement of the forecast quality and single cases where targeted observations deteriorate the forecast quality can also occur. In an idealised study, Morss and Emanuel (2002) discussed that a forecast degradation from additional assimilated observations can never be excluded in statistical data assimilation and nonlinear prediction. In fact, the results of observation targeting are crucially depending on the data assimilation system (Bergot, 2001). The low frequency of high impact weather events ad-

ressed by targeted observations limits the number of cases studied which complicates the significance of general conclusions. Additionally, the evaluation of forecasts of high impact weather events with traditional grid-point verification scores does not provide complete information about the forecast quality, especially of small-scale varying variables such as precipitation or surface wind gusts, and new forecast verification approaches are introduced to address this problem (Gilleland et al., 2010). The process of defining target regions is also not faultless. During the calculation of sensitive areas, which is based on imperfect models, linear assumptions are applied and in many targeting cases no general consensus can be found between different sensitive area calculations. Operational constraints pose another hurdle since target regions usually have to be defined in advance to the proposed deployment of targeted observations and it is often not possible to fully sample spatially extended sensitive areas with targeted observations deployed by aircraft, which may limit possible forecast improvements (e.g. Aberson, 2003).

## 2.4 Observing system experiments

OSEs, also called data denial experiments, are an important tool to evaluate the impact of existing observations of the GOS (e.g. Bouttier and Kelly, 2001; Kelly et al., 2007), new types of observations (e.g. Weissmann and Cardinali, 2007) or targeted observations (e.g. Irvine et al., 2009) on the analysis and forecast performance of NWP models. OSEs are usually performed retrospectively, but are generally carried out with the operational version of the NWP model. The interaction between the operational data assimilation scheme and the available observing network can be investigated in OSEs. Long sample periods from different seasons are ideal to get statistically significant results. Disadvantages of OSEs are that the retrospective experiments need considerable computing resources and results might be obsolete once the model system or operational observing network has changed.

In OSEs, at least two model runs are compared which only differ by the observations used for the data assimilation. One or more experiments are performed that either remove observations from the operational observing network to assess the assimilation system and the value of the removed observations or add observations to evaluate the enhancement to the operational observing network by the additional observations. These experiments are either compared to the operational model run, or a reference experiment with all operational observations (as in this study). The comparison to a reference experiment avoid differences that arise from small differences in the setup of the operational run and the retrospective experiments. The experiments on adaptive observations in this study assimilate the operational observations plus the set of targeted observations (Fig. 2.5). Initially, experiments use the same background information, data assimilation system and

forecast model. This guarantees that the difference, also referred to as ‘data signal’ or ‘data impact’, between the analysis (forecast) and the reference analysis (forecast) is only due to the assimilated additional observations.

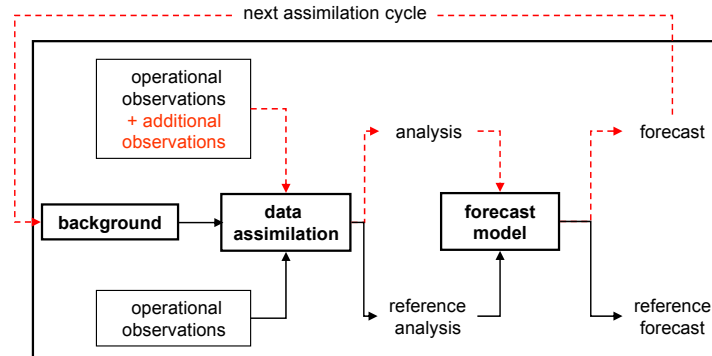


**Figure 2.5:** Schematic diagram of the setup of OSEs. In the cycled mode the background information for successive assimilation cycles is provided by the short-term forecast including additional observations. The background information in the uncycled mode is identical for the different experiments at successive assimilation cycles.

OSEs can be conducted in an uncycled or cycled mode (Fig. 2.5). If they are cycled, the information of the additional observations modifies a sequence of analyses since the background information of the following assimilation cycle is provided by the forecast initialised with the additional observations. By this procedure, information of additional observations is transported to subsequent analysis times, which is likely to increase the forecast impact of the additional observations if longer sample periods are evaluated. A cycled experiment reproduce the impact that additional observations would have in an operational framework. However, it is often impossible to trace the impact of the additional observations in detail as the ‘data signal’ at a certain time is caused by the extra observations at this time and the different background information. To evaluate the influence of the additional observations in detail, OSEs have to be performed uncycled, which means that they use the same background information which is generally provided by the reference run.

## Forecast verification

Different verification metrics are used to evaluate the forecast impact of adaptive observations in OSEs. For the forecast verification, a best estimate of the truth has to be defined which can either be derived from observations or model analyses. The advantage of verifying against observations is that the observations are independent of the NWP model.

However, observations are often of limited density and are not uniformly distributed. Thus, the model analysis is often used to verify forecasts since it provides the best estimate of the full atmospheric state.

Model analyses often show TC position errors larger than 25 km. Hence, all forecasts of TCs are verified against the JMA best track data. The best track data of TCs in the western North Pacific and the South China Sea are issued retrospectively by the Regional Specialized Meteorological Center (RSMC) Tokyo and provide information of the centre position, the central pressure and the maximum sustained wind speed for every single TC. These data are assigned based on the analysis of various meteorological observations such as surface observations from ships and buoys, geostationary meteorological satellite images, scatterometer surface winds, etc. The ECMWF TC model forecasts are evaluated in 12-hourly time steps for all times when the TC is classified as tropical storm or stronger in the JMA best track data and the TC is at least predicted by the model for the next 36 hours. For a statistical interpretation of the results, a Student's t-test for the difference of mean track forecast errors between experiments is calculated.

The TC position of the model is computed by searching for the sub-grid minimum of mean sea level pressure (MSLP) in the western North Pacific domain. The definition of the TC position as minimum MSLP shows no significant differences compared to the result of the operational ECMWF TC tracker algorithm (Van der Grijn et al., 2005). In general, the TC position definition by MSLP is reliable over the ocean, but can lead to errors when the TC reaches the complex orography of Taiwan with mountains up to 4000 m. In order to minimise the interference of model fields with the topography of Taiwan, the minimum of the geopotential height at 700 hPa instead of the MSLP is used to define the TC position when the model forecasts place the TC over Taiwan. This approach is confirmed by the visual interpretation of model fields.

Midlatitude forecasts of OSEs assimilating DIAL humidity observations are verified against ECMWF model analysis and evaluated in terms of total energy. Total energy is an integrated measure of the forecast error and includes information of wind ( $u, v$ ), temperature ( $T$ ) and specific humidity ( $q$ ) at multiple levels. The total energy (TE) error [ $\text{m}^2 \text{s}^{-2}$ ] of the forecast is defined as

$$TE_{F-A} = \frac{1}{2} [(u_F - u_A)^2 + (v_F - v_A)^2] + \frac{1}{2} \frac{c_p}{T_{ref}} (T_F - T_A)^2 + \frac{1}{2} \frac{L^2}{c_p T_{ref}} (q_F - q_A)^2, \quad (2.9)$$

similar to the energy norm used in Ehrendorfer et al. (1999) with a reference temperature ( $T_{ref} = 300 \text{ K}$ ), the specific heat at constant pressure ( $c_p = 1004.7 \text{ J kg}^{-1} \text{ K}^{-1}$ ) and the latent heat of condensation ( $L = 2.51 \cdot 10^6 \text{ J kg}^{-1}$ ). The subscript  $F$  denotes the forecast and the subscript  $A$  the analysis fields. The calculation of  $TE_{F-A}$  is done at 850, 500 and

250 hPa, and the results summed.

## 2.5 T-PARC observations

The summer phase of T-PARC and the collaborative Tropical Cyclone Structure (TCS08) field experiment (Elsberry and Harr, 2008) took place in the western North Pacific basin from August to October 2008. The aims were to increase the understanding of TC formation, intensification, structure change and extratropical transition, as well as to improve the forecast skill of TCs. Different research aircraft, the United States Air Force WC-130, the Naval Research Laboratory (NRL) P-3, and the DLR Falcon 20, were operated within T-PARC. Those aircraft were supplemented by the Taiwanese Astra Jet operated under the research programme DOTSTAR, an operational surveillance programme to deploy dropsonde observations in the environment of TCs that pose a threat to the Taiwanese island (Wu et al., 2005, 2007b). Altogether, up to four aircraft with dropsonde systems were simultaneously available and spent more than 500 flight hours. In addition to the aircraft, driftsonde gondolas were launched on Hawaii. The gondolas released dropsondes while they were drifting westwards towards Asia in the lower stratosphere. JMA conducted additional radiosonde soundings (TEMPs) and in-situ synoptic observations (SYNOps) from research vessels and ground stations. Further, extra observations of MTSAT-2<sup>1</sup> rapid scan AMVs were produced by JMA's meteorological satellite centre.

Four typhoon systems were investigated during the campaign (Fig. 2.6). Two storms, Nuri and Hagupit, traveled straight to the west without making recurvature. They both passed by the northern end of Luzon, Philippines, before they moved on and made landfall on the southeastern Chinese coast next to Hong Kong (Nuri) and further west next to Maoming, China (Hagupit). The two other storms, Sinlaku and Jangmi, developed east of the Philippines, headed northwestward and made landfall on Taiwan. They recurved and moved to the northeast. While Jangmi weakened and dissipated to the southwest of Japan, Sinlaku intensified again after recurvature and passed by south of Japan before the system underwent ET. Both, Sinlaku and Jangmi, were observed frequently by all four aircraft. For the first time, systematic observations targeted on TCs during the full life cycle of a storm from the genesis in tropical waters throughout the northwestward movement, recurvature and ET were conducted in the western North Pacific basin.

Sensitive area calculations of several targeting techniques were available for evaluation and comparison of targeting strategies. For the planning of targeted observations, the EURORISK PREVIEW Data Targeting System (DTS<sup>2</sup>) was applied during the cam-

---

<sup>1</sup>Multi-functional transport satellite-2

<sup>2</sup>[http://www.ecmwf.int/research/WMO\\_projects/TPARC/DTS\\_for\\_TPARC.pdf](http://www.ecmwf.int/research/WMO_projects/TPARC/DTS_for_TPARC.pdf)

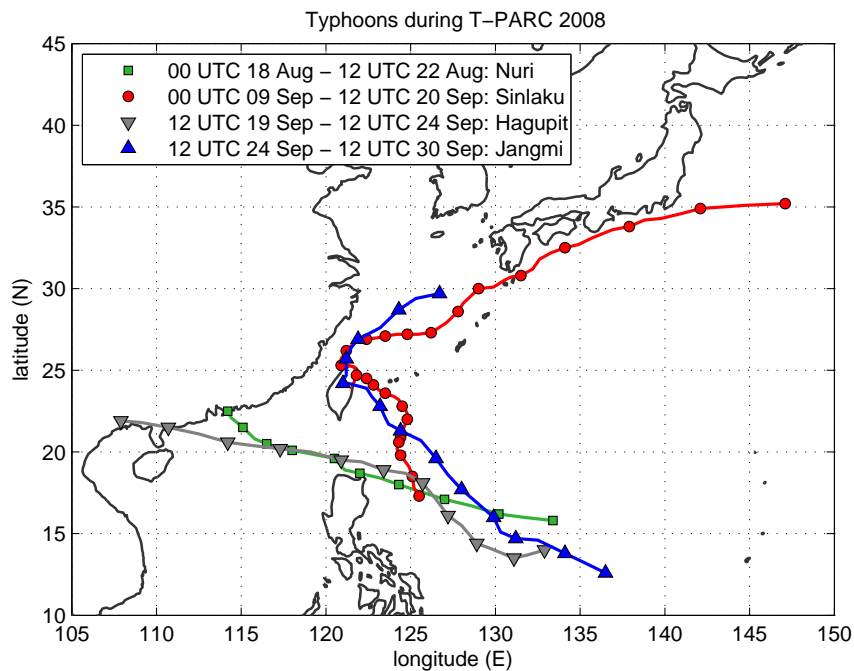


**Figure 2.6:** JMA best track data of observed typhoons during T-PARC 2008: Nuri (green rectangles), Sinlaku (red squares), Hagupit (grey downward-pointing triangles) and Jangmi (blue upward-pointing triangles). The markers indicate the position of the typhoons at 00 UTC and 12 UTC for the period the storms reached at least tropical storm intensity.

paign. DTS is an interactive web-based system that allows specified users to identify and propose targeting cases and to request sensitive area calculations for selected cases based on SV calculations of the ECMWF model and ETKF calculations of a multimodel (NCEP/ECMWF/CMC) and the United Kingdom Met Office (UKMO) ensemble. Further, SV- and ETKF-based sensitive area calculations from several institutions (e.g. JMA, National Taiwan University, University of Washington, University of Yonsei) were accessible via the DTS.

An example of targeting guidance for Typhoon Sinlaku by six different methods valid for targeted observations at 00 UTC 11 Sept 2008 is shown in Fig. 2.7. ETKF-based calculations (Figs. 2.7 c,e) placed sensitive areas close to the centre of the storm, while singular vectors and the ADSSV rather pointed to regions to the north and east of Sinlaku. In addition, upstream regions over China were indicated to be sensitive by ECMWF and NOGAPS SVs.

The infrastructure of T-PARC with multiple aircraft available, made it possible to sample different sensitive areas highlighted by different targeting techniques. Figure 2.8 shows the flight tracks of the joint mission that incorporated the targeting guidance for Typhoon Sinlaku (Fig. 2.7). All flights were performed within 24 hours between 2000 UTC

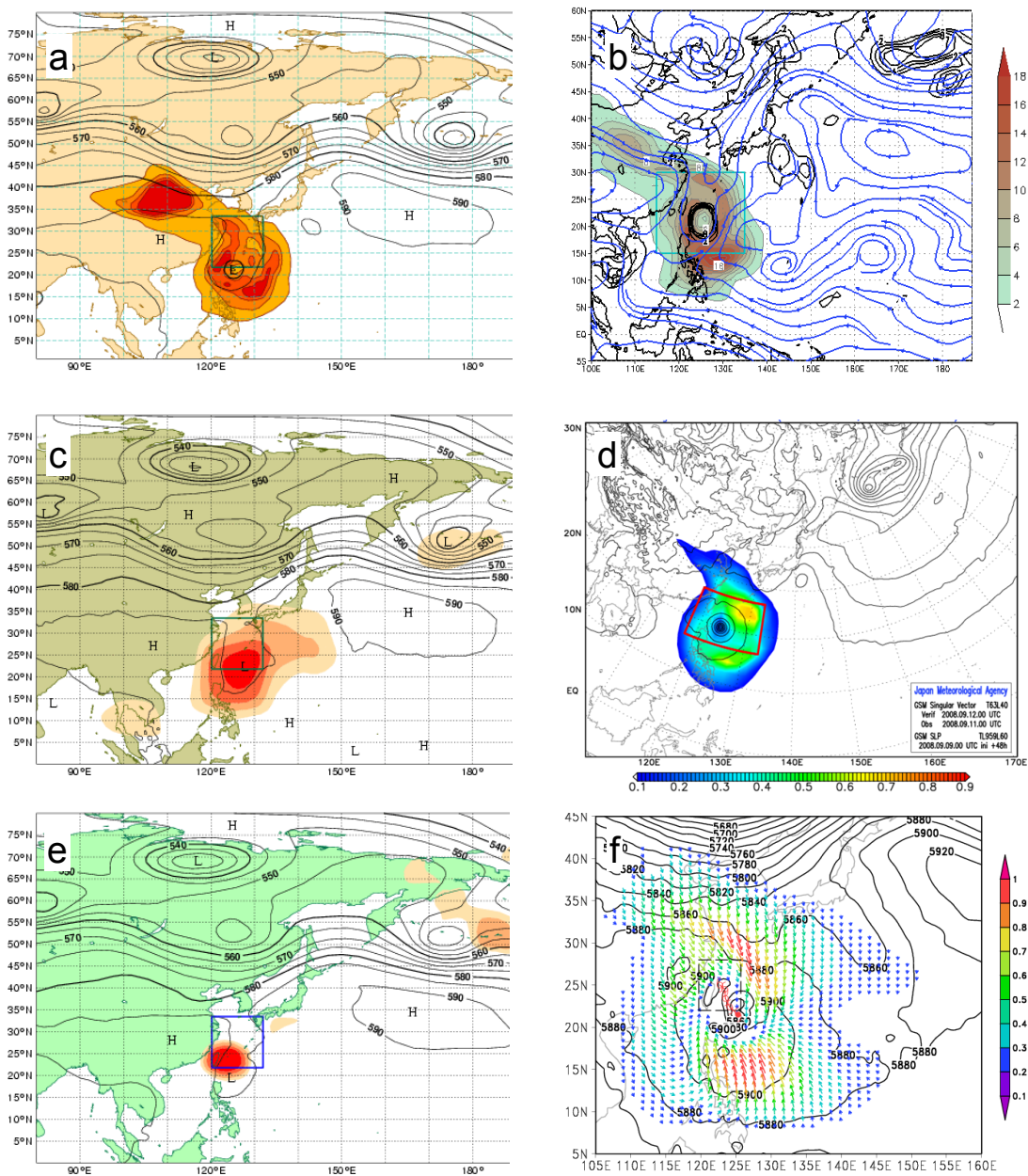


**Figure 2.7:** Overview of targeting guidance by different methods: (a) ECMWF SV, (b) NO-GAPS SV, (c) multimodel (NCEP/ECMWF/CMC) ETKF, (d) JMA SV, (e) UKMO ETKF and (f) MM5 ADSSV.

10 Sept and 1828 UTC 11 Sept 2008. The DOTSTAR flight strategy was to circumnavigate the TC and provide observations all around the storm with higher dropsonde coverage in sensitive regions. The DLR Falcon stayed further away from the TC and sampled sensitive

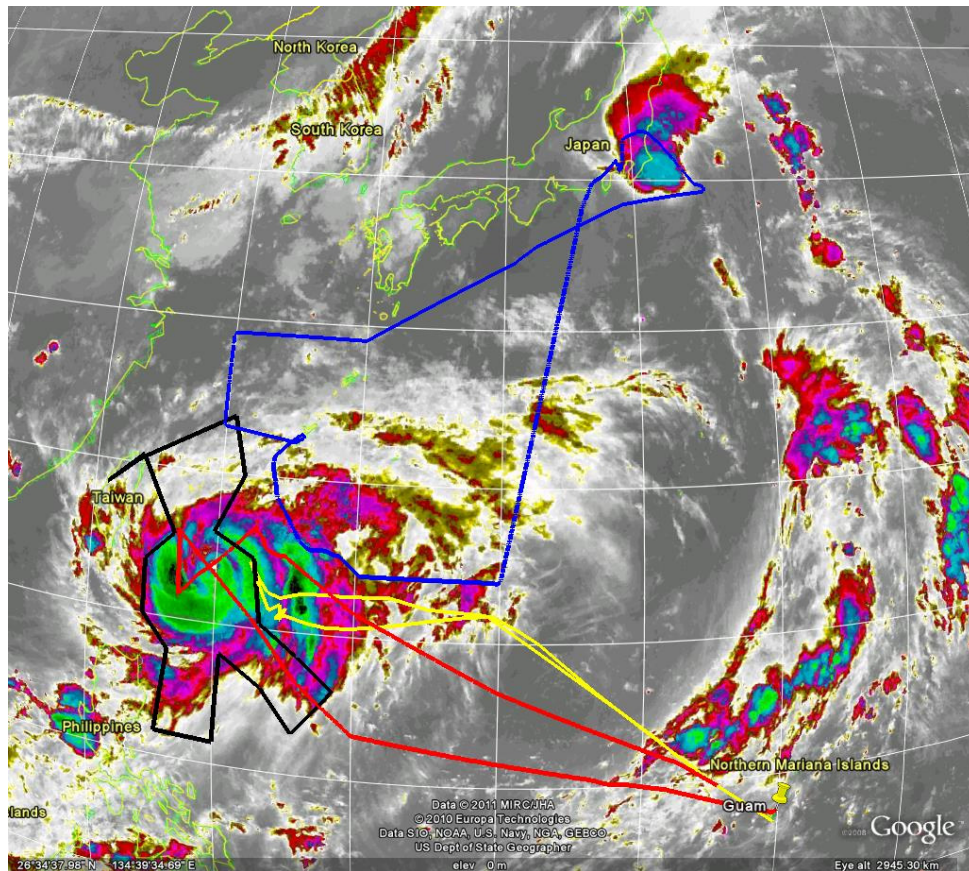


**Figure 2.8:** Flight tracks of the four aircraft joint mission for Typhoon Sinlaku: WC-130 (blue; 0728-1828 UTC 11 Sept 2008), NRL P-3 (yellow; 2019 UTC 10 Sept - 0602 UTC 11 Sept 2008), DOTSTAR astra jet (black; 2043 UTC 10 Sept - 0242 UTC 11 Sept 2008) and DLR Falcon (red; 0320-1220 UTC 11 Sept 2008). Enhanced MTSAT IR imagery valid at 1030 UTC 11 Sept 2008 provided by NCAR/EOL<sup>3</sup>.

regions to the north and east of the system. While the WC-130 covered the typhoon centre and penetrated the core and eye wall of Sinlaku, the NRL P-3 observed rainbands to the east of Sinlaku.

The DLR Falcon 20 aircraft was based in Atsugi, Japan and performed 25 research flights spending 93 flight hours in the period from 26 Aug 2008 to 01 Oct 2008. The payload of the Falcon, shown in Fig. 2.9, consists of three observational platforms: a dropsonde system, a water vapour DIAL system and a Doppler wind lidar. This unique setup provides the possibility to observe collocated water vapour and wind profiles from in-situ and remote sensing instruments. In addition to T-PARC observations (dropsondes, extra TEMPs and

<sup>3</sup>National Center for Atmospheric Research/Earth Observing Laboratory

SYNOPs) that were provided to the GOS via the Global Telecommunication System (GTS) in real-time, DIAL humidity observations sampled by the DLR Falcon are analysed in this thesis. The Doppler wind lidar observations sampled during T-PARC are evaluated in Weissmann et al. (2011).

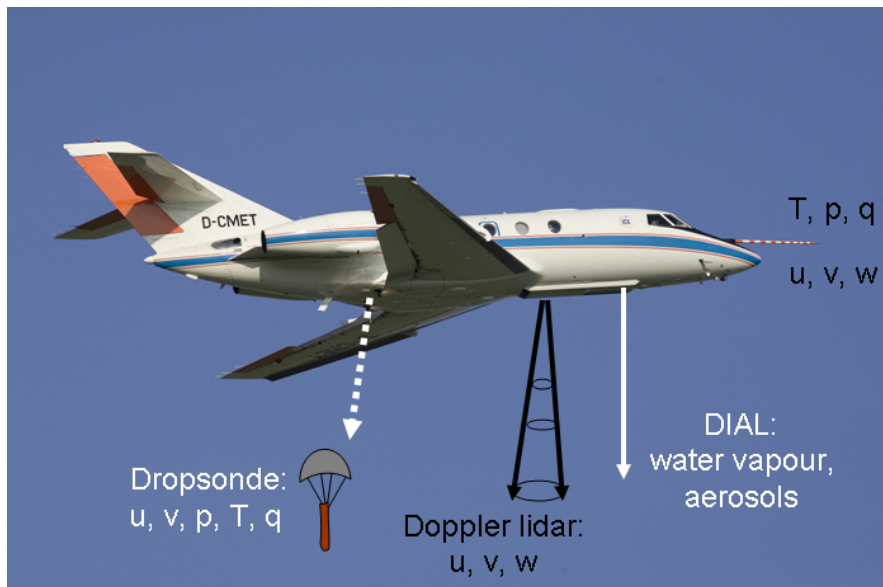


**Figure 2.9:** The DLR Falcon 20 research aircraft and its instrumentation during T-PARC. Picture provided by Minoru Toyoshima.

## 2.6 Dropsonde system

The Global Position System (GPS) dropsonde was developed at NCAR (Hock and Franklin, 1999) and is produced by Vaisala. During the summer phase of T-PARC about 1500 dropsondes of the type Vaisala RD-93<sup>4</sup> were launched from four aircraft.

The NCAR GPS dropsonde consists of a module containing pressure, temperature and humidity sensors, a GPS receiver module to determine wind from the dropsonde shift and a 400 MHz telemetry transmitter which transfers data from the sonde to a receiving system, which for example is installed on-board of an aircraft (Hock and Franklin, 1999). Data are transmitted continuously from the launch of the dropsonde until it hits the ocean surface. The dropsonde is attached to a small parachute and the overall descent rate is approximately  $11 \text{ m s}^{-1}$ . Measurements are performed with 2 Hz temporal resolution, which yields a vertical resolution of temperature, pressure, humidity and wind profiles ranging from 5

<sup>4</sup>[http://br.vaisala.com/files/RD93\\_Dropsonde\\_Datasheet\\_in\\_English.pdf](http://br.vaisala.com/files/RD93_Dropsonde_Datasheet_in_English.pdf)

to 10 m (Wang et al., 2010). Dropsonde data profiles are carefully quality-controlled using several post-processing methods including an automatic sounding quality-control software called Atmospheric Sounding Processing Environment (ASPEN<sup>5</sup>). For example, ASPEN calculates the height of the dropsonde observations by integrating upwards from the point where the dropsonde hits the surface.

	range	resolution	accuracy	response time
pressure	3 - 1080 hPa	0.1 hPa	0.4 hPa	
temperature	-90 to +60 °C	0.1 °C	0.2 °C	< 2 s
humidity	0 - 100%	1%	2%	< 0.5 s at +20 °C < 20 s at -40 °C
wind	0 - 200 m s <sup>-1</sup>	0.1 m s <sup>-1</sup>	0.5 m s <sup>-1</sup> RMS	

**Table 2.1:** Vaisala RD-93 specifications for dropsonde measurement errors. Accuracy refers to the standard deviation of differences between two successive repeated calibrations. RMS stands for root mean square. Response time is valid at 6 m s<sup>-1</sup> descent rate and 1000 hPa. Numbers adapted from Vaisala<sup>4</sup>.

Quality-controlled dropsonde data can be sent out to the GTS directly from the aircraft to be available as part of the GOS. Dropsondes provide accurate observations of pressure, temperature, humidity and wind (Tab. 2.1), that are assimilated operationally in NWP models if available. From the FASTEX campaign in 1997 onwards, GPS dropsondes were frequently applied during field campaigns and dropsonde observations were used for OSEs and targeting studies (e.g. Montani et al., 1999; Szunyogh et al., 2002; Petersen and Thorpe, 2007; Irvine et al., 2009). Additionally, in-situ dropsonde observation profiles were applied to study the vertical distribution of different atmospheric variables such as water vapour (e.g. Zhang et al., 2003; Wang, 2005; Wang et al., 2010).

## 2.7 Differential absorption lidar

### 2.7.1 Basic principles

The active remote sensing technique of a DIAL can be used to measure the concentration of various atmospheric trace gases such as water vapour, ozone, carbon dioxide, methane, etc. (Ehret et al., 1999; Gimmetstad, 2005; Bösenberg, 2005). A DIAL system emits spectrally narrow ( $\sim 0.1$  GHz) and short (several ns) laser pulses at two distinct wavelengths, an on-line wavelength which is placed at an absorption line of the trace gas of interest and an

<sup>5</sup><http://www.eol.ucar.edu/isf/facilities/software/aspn/aspn.html>

off-line wavelength at a nearby non-absorbing wavelength. The concentration of the trace gas can be derived from the intensity difference of the backscatter signal received at the two wavelengths.

The basic equation when dealing with lidar systems is the so-called lidar equation (Wandinger, 2005) which describes the backscattered power  $P$  of an emitted laser signal as a function of the wavelength  $\lambda$  and the distance  $r$  to the scattering volume:

$$P(r, \lambda) = P_0 \cdot \frac{c\tau}{2} \cdot A \cdot \eta \cdot \frac{1}{r^2} \cdot \beta(r, \lambda) \cdot T^2(r, \lambda) . \quad (2.10)$$

$P_0$  is the power of the emitted laser signal,  $c$  the speed of light,  $\tau$  the duration of the laser pulse,  $A$  the area of the telescope,  $\eta$  the overall system efficiency and  $\beta$  the backscatter coefficient consisting of the Rayleigh backscatter by air molecules and the Mie backscatter by clouds and aerosols. The atmospheric transmission  $T$  has to be calculated for the two way path from the source of the laser signal to the scattering volume and back. The Lambert-Beer-Bouguer law gives the relationship between the atmospheric transmission from the location of the laser to the distance or range  $r$  and the atmospheric extinction coefficient  $\alpha$  (Wandinger, 2005):

$$T(r, \lambda) = \exp\left[-\int_0^r \alpha(r', \lambda) dr'\right] . \quad (2.11)$$

The atmospheric extinction coefficient  $\alpha$  as function of the wavelength  $\lambda$  and range  $r$  is

$$\alpha(r, \lambda) = \sigma(p(r), T(r), \lambda) \cdot n(r) + \alpha_{mol}(r, \lambda) + \alpha_{aer}(r, \lambda) \quad (2.12)$$

with the molecular number density of the trace gas  $n$  [ $\text{m}^{-3}$ ], its molecular absorption cross section  $\sigma$ , the extinction due to air molecules  $\alpha_{mol}$  and due to aerosols and clouds  $\alpha_{aer}$  (Kiemle, 2008). The molecular absorption cross section  $\sigma$  is also dependent on the temperature ( $T$ ) and the pressure ( $p$ ) which both can vary with the range  $r$ . If the on- and off-line wavelength separation is small ( $\sim 1$  nm), it can be assumed that the difference  $\Delta\alpha$  of the atmospheric extinction coefficients at the on- and off-line wavelength is only due to the difference in the absorption cross sections of the trace gas at the two wavelengths (Gimmestad, 2005). This difference  $\Delta\alpha$  can be written as

$$\Delta\alpha(r) = \Delta\sigma(r) \cdot n(r) = [\sigma(r, \lambda_{on}) - \sigma(r, \lambda_{off})] \cdot n(r) . \quad (2.13)$$

The small wavelength separation also allows the assumption of identical backscatter coefficients  $\beta$  for the on- and off-line wavelengths so that the molecular number density of the trace gas  $n$  can be calculated from the ratio of the backscattered power (Eq. 2.10)

$P(r, \lambda_{off})/P(r, \lambda_{on})$  at the two wavelengths:

$$n(r) = \frac{1}{2\Delta\sigma(r)} \frac{\delta}{\delta r} \ln \left[ \frac{P(r, \lambda_{off})}{P(r, \lambda_{on})} \right]. \quad (2.14)$$

Equation 2.14 is the DIAL equation (Gimmetstad, 2005) written in its differential form. The differential absorption cross section  $\Delta\sigma$  is an important part in the DIAL equation. A typical molecular absorption line shape with the choice of DIAL on- and off-line wavelength is shown in Fig. 2.10. Note that the absorption line shape may change with temperature and pressure.

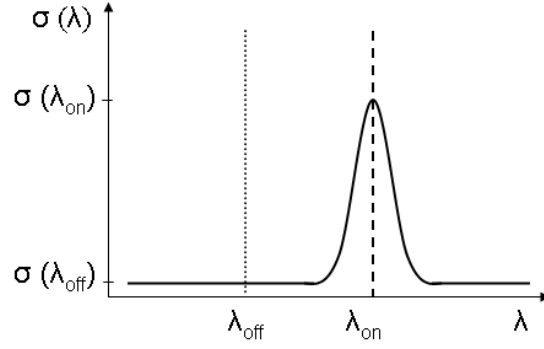


**Figure 2.10:** Sketch of the molecular absorption cross section as function of the wavelength.

Given a finite range resolution  $\Delta r$  of the laser signal, the DIAL equation (Eq. 2.14) can be converted to

$$\bar{n}(r + \Delta r) = \frac{1}{2\Delta\sigma(r)} \frac{1}{\Delta r} \ln \left[ \frac{P(r + \Delta r, \lambda_{off})}{P(r, \lambda_{off})} \frac{P(r, \lambda_{on})}{P(r + \Delta r, \lambda_{on})} \right], \quad (2.15)$$

with the average molecular number density  $\bar{n}$  within the scattering volume between  $r$  and  $r + \Delta r$  (Gimmetstad, 2005). To derive the number density of the measured trace gas  $n$  from the DIAL equation, no system constants of the lidar are required and no calibration of the measured signals has to be carried out.

A balance between atmospheric extinction and return signal power should be achieved when the absorption line strength and the on-line wavelength are selected (Kiemle, 2008) since the extinction of the on-line signal is linearly proportional to the concentration  $n$  of the measured trace gas and its absorption cross section  $\sigma$  (Eq. 2.12). If the extinction of the on-line wavelength is very large, the signal is attenuated strongly which limits the measurement range. However, if the absorption is too weak or the finite range interval  $\Delta r$  too small, the difference between on- and off-line wavelength signal is too small and

dominated by noise (Eq. 2.15). To achieve a large range and simultaneously measure range-dependent concentrations of the trace gas of interest accurately, further on-line wavelengths can be added. Each of the on-line wavelengths is tuned to differently strong absorption lines which optimises the balance between atmospheric extinction and return signal for different range intervals and trace gas concentrations.

The DIAL equation is derived under the condition that the system parameters are identical for the on- and off-line wavelengths, which requires a proper design of the components of the DIAL system (Kiemle, 2008). The laser has to be stable and spectrally narrow as the on-line wavelength should be at least one order of magnitude narrower than the absorption line. Additionally, the on- and off-line wavelengths need to be close enough (less than 1 nm separation) and no other trace gas should have an absorption line at the considered wavelengths so that the assumption of similar backscatter and extinction properties by air molecules and aerosols of on- and off-line wavelength is valid.

More details of the DIAL technique can be found in Ismail and Browell (1989), Bösenberg (1998), Gimmetstad (2005), Bösenberg (2005) and Kiemle (2008).

## 2.7.2 Airborne WALES demonstrator

The WALES demonstrator (Wirth et al., 2009) is an airborne four-wavelength water vapour DIAL system and was installed on-board of the DLR falcon during T-PARC (Fig. 2.9). The first observations with the nadir-pointing WALES demonstrator were collected during COPS and E-TReC in 2007 and were analysed in an intercomparison study of ECMWF model fields and DIAL humidity observations (Schäfler et al., 2011a).

The WALES demonstrator uses two additional on-line wavelengths to enable a simultaneous coverage of measurements over the whole troposphere with high accuracy (Wirth et al., 2009). The three on-line and one off-line wavelengths are located within 0.6 nm in the 935 nm water vapour absorption band. There are different systematic and statistical error sources that can affect the DIAL observations (Poberaj et al., 2002). Statistical errors that may result from detection noise or low signal-to-noise ratios can be reduced by averaging the raw signals before applying the DIAL equation. Systematic errors may originate from uncertainties related to the water vapour absorption line parameters, the temperature dependency of the absorption cross section, the spectral purity of the laser and the stability of the on-line wavelength. Uncertainties in the temperature along the measured water vapour profile may introduce additional systematic errors since the absorption cross section is also a function of temperature. However, it was shown that the error of the humidity observations can be expected to be less than 5-7% (Kiemle et al., 2007; Bhawar et al., 2011).

The nadir-pointing WALES demonstrator provides observations at a high spatial resolution. The horizontal resolution depends on the averaging interval of the profiles and the speed of the aircraft. For the T-PARC data set the averaging interval was 30 seconds which leads to a horizontal resolution of 5-7 km. In the vertical, the raw data are processed with a resolution of 15 m, but for the humidity retrieval the resolution  $\Delta r$  needs to be reduced to at least 290 m to fulfil precision requirements for data assimilation and provide vertically uncorrelated observations. The DIAL instrument is sensitive to clouds and can not penetrate optically thick clouds or rain, which reduces the observational coverage in cloudy areas. Simultaneously conducted atmospheric backscatter measurements were used to determine lidar signals that were contaminated by clouds. Strict threshold were applied to those signals and all DIAL observations below clouds were generally omitted to provide accurate observations.



## Chapter 3

# The influence of adaptive dropsonde observations on ECMWF typhoon track forecasts

### 3.1 Introduction

The influence of adaptive T-PARC observations on ECMWF typhoon track forecasts during the two major typhoon events, Sinlaku and Jangmi, is evaluated in the following chapter by conducting OSEs. Dropsondes released from the different aircraft or driftsonde gondolas, extra TEMPs and SYNOPs from JMA research vessels are considered as additional T-PARC observations.

Figure 3.1 shows the location of all T-PARC soundings that are used for the OSEs. During the lifetime of Sinlaku and Jangmi, 481 and 224 extra soundings were deployed, respectively. Aircraft missions for Typhoon Sinlaku and Jangmi were performed during the whole life cycle of these storms from early stages in the tropics throughout their recurvature and ET. Dropsondes released by the WC-130 aircraft in the typhoon core and centre were also assimilated in the OSEs.

The setup of the performed experiments is described in section 3.2. The results of influence of T-PARC observations on typhoon track forecasts are presented in section 3.3 and the importance of a correct observation time is highlighted in section 3.4. A discussion and summary are given in section 3.4.

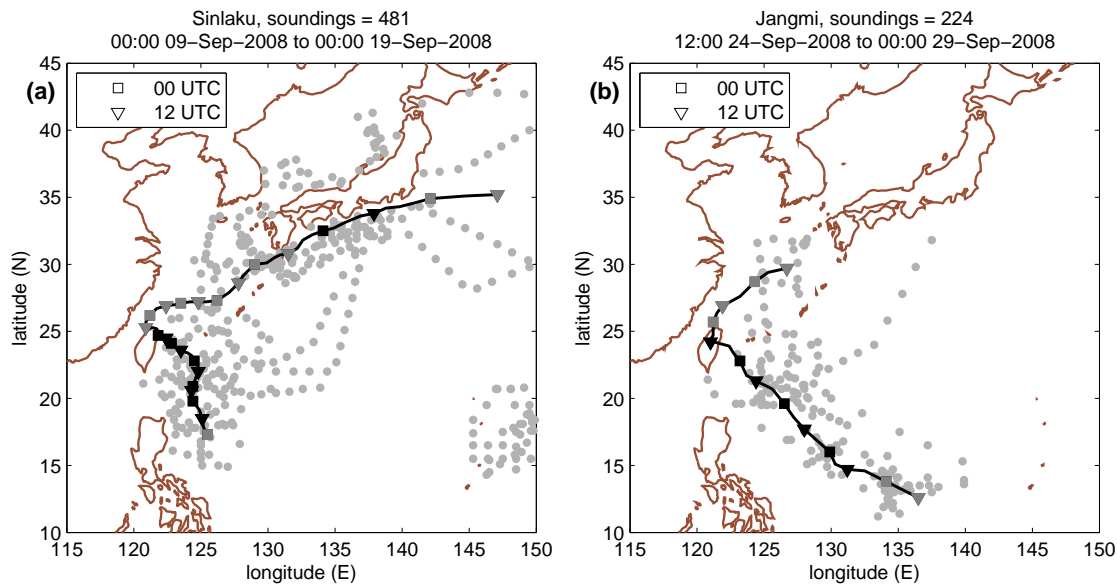


**Figure 3.1:** JMA best track data of (a) Typhoon Sinlaku and (b) Typhoon Jangmi with T-PARC dropsonde and TEMP locations for the respective storms. Rectangles (triangles) on the best track show the position of Sinlaku and Jangmi at 00 UTC (12 UTC) starting on 00 UTC 09 Sept 2008 and 12 UTC 24 Sept 2008, respectively. Black symbols indicate typhoon intensity and grey symbols tropical or severe tropical storm intensity.

## 3.2 Experimental design

OSEs were performed using the spring 2009 version of the ECMWF modelling system (cycle 35r2). The horizontal resolution of the experiments was  $T_L799$  ( $\sim 25$  km) and 91 vertical levels were used. Weakened constraints for the BgQC of dropsondes, which are operationally applied to a region up to  $30^\circ\text{N}$  to avoid very high rejection rates within and near TCs, were extended up to  $40^\circ\text{N}$ , because of the re-intensification of Sinlaku near of  $30^\circ\text{N}$ . In practice, the BgQC for dropsondes was inactive in this region. During the assimilation, the VarQC procedure is applied which modifies the cost function by reducing the weight of observations with large innovations.

Three different experiments were performed. A control experiment (NoObs) without T-PARC observations (western North Pacific basin dropsondes, extra ship SYNOPs and TEMPs) was carried out and serves as reference. The second experiment (DROP) assimilated all adaptive T-PARC observations (Fig. 3.1). DROP was conducted in a cycled mode and the background information used in the assimilation system was provided by the short-term forecast of DROP (see also section 2.4). Both NoObs and DROP covered the period between 09 Sept 2008 and 01 Oct 2008. Additionally, a third experiment DROP\_UnCy

was performed for all times without cycling when adaptive observations were available. The background information in DROP\_UnCy was provided by of the short-term forecast of the control experiment NoObs. The clear majority of assimilated adaptive T-PARC observations in DROP and DROP\_UnCy consisted of airborne dropsondes (Fig. 3.1). Hence, the influence of all adaptive observations is abbreviated with ‘dropsonde influence’ even if some extra TEMP and SYNOP observations are included.

### 3.3 Results

Typhoon track forecast are verified against the JMA best track data. Track forecasts are evaluated in 12-hourly time steps for all times when the storm system is classified as tropical storm or stronger in the JMA best track data and the forecast time of the storm in the model is at least 36 hours long. As Typhoon Sinlaku is classified as tropical storm until 12 UTC 20 Sept, all forecasts between 00 UTC 09 Sept and 00 UTC 19 Sept 2008 are used. Typhoon Jangmi reached tropical storm intensity between 12 UTC 24 Sept and 21 UTC 30 Sept 2008, and forecasts initialised until 00 UTC 29 Sept are evaluated. A secondary low in the model forecast affects the position calculation of Jangmi from MSLP fields when Typhoon Jangmi was located directly over Taiwan at 12 UTC 28 Sept 2008 (compare Fig. 3.1). Thus, the minimum of the geopotential height at 700 hPa is used instead of MSLP for the forecasts initialised between 00 UTC 26 Sept and 00 UTC 28 Sept 2008. For a statistical evaluation of the results, the statistical significance at 90 and 95% confidence level of the mean track forecast error difference between the different experiments is calculated using a Student’s T test.

Figure 3.2a shows the mean track forecast errors of the Typhoons Sinlaku and Jangmi. Until forecast lead times of +72 h, the difference between the track errors of DROP and NoObs is very small and both experiments have a mean track error of about 220 km at +72 h. The track errors start to differ at longer forecast lead times and DROP shows continuously smaller mean track errors compared to NoObs between +84 h and +120 h. The mean track forecast error is reduced from approximately 620 km to 480 km at +120 h due to the assimilation of adaptive T-PARC observations, which is an improvement of 22.4% (Tab. 3.1). The improvements at longer forecast lead times ( $\geq +96$  h) are statistical significant at 95% confidence level.

The scatter plot of the track errors (Fig. 3.2b) illustrates that if track forecast errors are smaller than 200 km, the mean errors are similar for DROP and NoObs as the black symbols are located close to the diagonal. The single cases show a large variability and improved and deteriorated cases are identified as symbols are distributed in equal parts above or below the diagonal. Track errors for long forecast lead times ( $\geq +72$  h) are

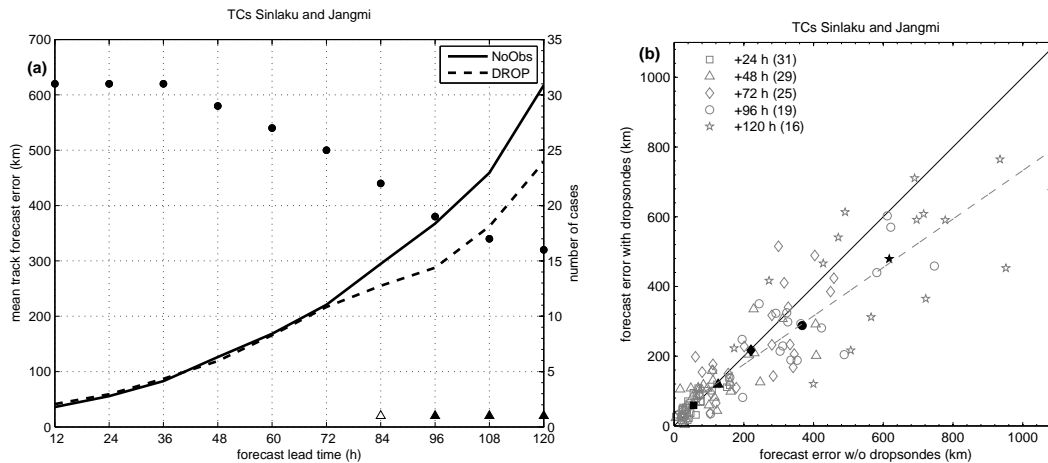


**Figure 3.2:** (a) Mean track forecast errors for DROP (dashed) and NoObs (solid). Mean track errors are computed for all forecast times of Typhoon Sinlaku (00 UTC 09 Sept - 00 UTC 19 Sept 2008) and Typhoon Jangmi (12 UTC 24 Sept - 00 UTC 29 Sept 2008) and are verified against the JMA best track data before 12 UTC 20 Sept and 12 UTC 30 Sept, respectively. Black dots represent the number of cases evaluated at each forecast lead time. Empty (filled) triangles highlight times when mean track differences are significant at 90% (95%) confidence level. In (b) the track forecast error of DROP is plotted against the error of NoObs for all analysed 31 cases. Errors at different forecast lead times are displayed by different grey symbols and mean errors are shown as black filled symbols. Values below the diagonal (solid line) indicate that errors in DROP are smaller than in NoObs. The dashed grey line represents a linear regression fit.

predominantly larger than 200 km and show an increased spread with a higher percentage located below the diagonal equivalent to a reduction of the track forecast errors in the DROP experiment. On average, the track errors are smaller in DROP but there are single cases with larger track errors. However, errors of those deteriorating cases are closer to the diagonal than the errors of improving cases.

The mean track forecast errors for Typhoon Sinlaku and Typhoon Jangmi, respectively, are displayed in Fig. 3.3. The result for Sinlaku (Fig. 3.3a) is comparable to the result for the whole period including both storms (Fig. 3.2a), but smaller track forecast errors of DROP are found already at shorter forecast lead times ( $\geq +48$  h). The improvements of DROP are significant at 95% confidence level from +84 h onwards. A different result is seen for Typhoon Jangmi (Fig. 3.3b) where mean track forecast errors of DROP and NoObs are similar and no clear improvement from the additional observations is found. Between +60 h and +84 h, an increase of the track error of DROP is seen that is significant at +60 h. Mean track errors of NoObs are smaller for Jangmi compared to Sinlaku which may be one of the reasons for the low impact of dropsondes. Furthermore, the number of available Jangmi forecasts decreases after +36 h and only less than five cases are averaged

after +84 h, which leads to lower significance of the results.

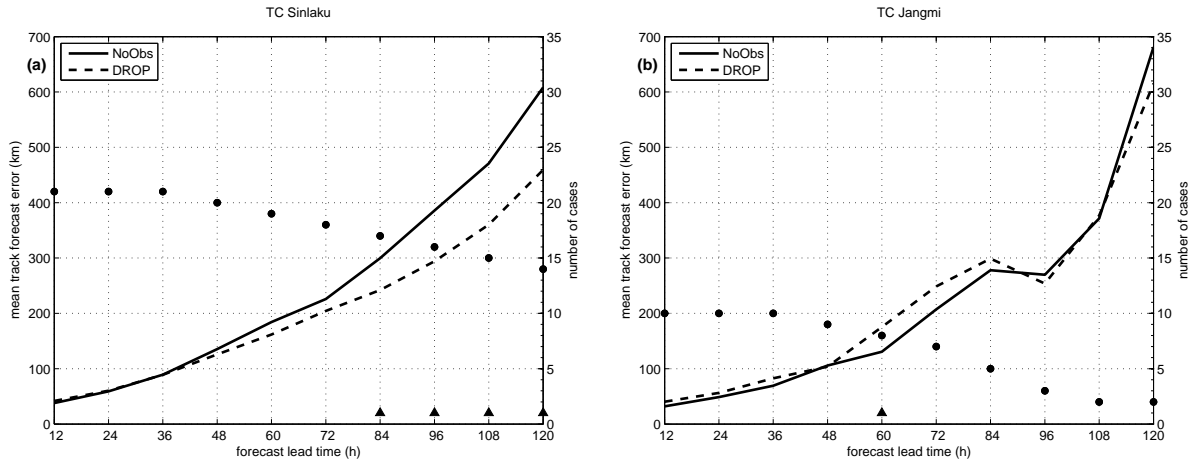


**Figure 3.3:** As in Fig. 3.2a, but valid for (a) Typhoon Sinlaku (00 UTC 09 Sept - 00 UTC 19 Sept 2008) and (b) Typhoon Jangmi (12 UTC 24 Sept - 00 UTC 29 Sept 2008).

Table 3.1 summarises the mean track error reduction of DROP compared to NoObs for Sinlaku and Jangmi. The mean track forecast errors for the entire period with both typhoon events are reduced for forecast lead times of more than +48 h. The forecast error reduction due to the assimilation of adaptive T-PARC dropsonde observations is larger than 20% at +96 h and +120 h. While the overall improvements for the whole period are strongly influenced by larger improvements during Sinlaku, improved and deteriorated forecasts alternate for Jangmi at different lead times.

	+24 hours	+48 hours	+72 hours	+96 hours	+120 hours
Sinlaku & Jangmi	<i>5.9</i>	-5.7	-1.7	-21.7	-22.4
Sinlaku	<i>2.1</i>	-7.1	-9.5	-23.7	-24.5
Jangmi	<i>15.7</i>	-1.8	<i>19.9</i>	-5.9	-9.7

**Table 3.1:** Mean track forecast error reduction (%) for the Typhoons Sinlaku and Jangmi. Positive (italic) numbers indicate when a degradation of the mean track forecast error of DROP compared to NoObs is obtained.

The main improvements of the track forecast errors for Typhoon Sinlaku are achieved at the early phase of the typhoon before landfall on 14 Sept 2008 (Fig. 3.4a). Shortly after landfall, Sinlaku reaches its easternmost position and recurves later the same day. In the period before landfall, track forecast errors are smaller in DROP from +60 h onwards, statistically significant from +72 h onwards. Errors of DROP and NoObs are similar after

landfall and recurvature, respectively (Fig. 3.4b). The number of cases with longer forecast lead times is reduced as track forecasts of Sinlaku are only evaluated until 12 UTC 20 Sept 2008.

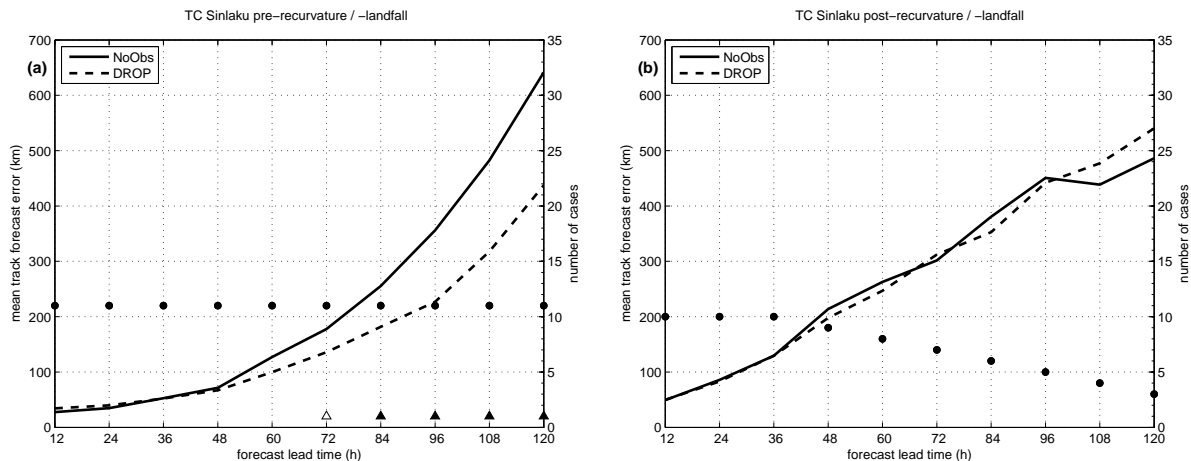


**Figure 3.4:** As in Fig. 3.2a, but valid for Typhoon Sinlaku (a) before landfall (00 UTC 09 Sept - 00 UTC 14 Sept 2008) and (b) after landfall (12 UTC 14 Sept - 00 UTC 19 Sept 2008).

Improvements found for the whole period of Sinlaku and Jangmi are considerably influenced by the large improvements found during the early phase of Sinlaku. At this phase, large uncertainties of track forecasts are related to the landfall on Taiwan and recurvature scenario of the system as identified from the spread in the operational ECMWF ensemble prediction system (EPS) (Fig. 3.5a). The increased spread of the EPS suggests that the track forecasts are sensitive to changes in the initial condition in the TC environment. The assimilation of additional T-PARC observations affects the track forecast and the landfall and recurvature scenario is predicted more accurate compared to the reference experiment. After landfall and recurvature of Sinlaku, the EPS uncertainty in the track forecasts is reduced (Fig. 3.5b) as all member of the ECMWF EPS predict a similar northeastward movement of Sinlaku. The lower influence of the additional TC observations during this stage is likely related to smaller forecast errors and the higher importance of the midlatitude flow.

In contrast to the cycled experiment DROP, the uncycled experiment DROP\_UnCy shows little improvement compared to NoObs (Fig. 3.6). Note that the number of evaluated cases is reduced since only those times are considered when extra observations are available. This different sample of cases also leads to slightly different results for DROP and NoObs (compare Fig. 3.2a). The comparably low improvement of DROP\_UnCy implies that the information of the observations transported via the background in DROP provides valuable information which has a positive influence on the forecasts even on days when no adaptive

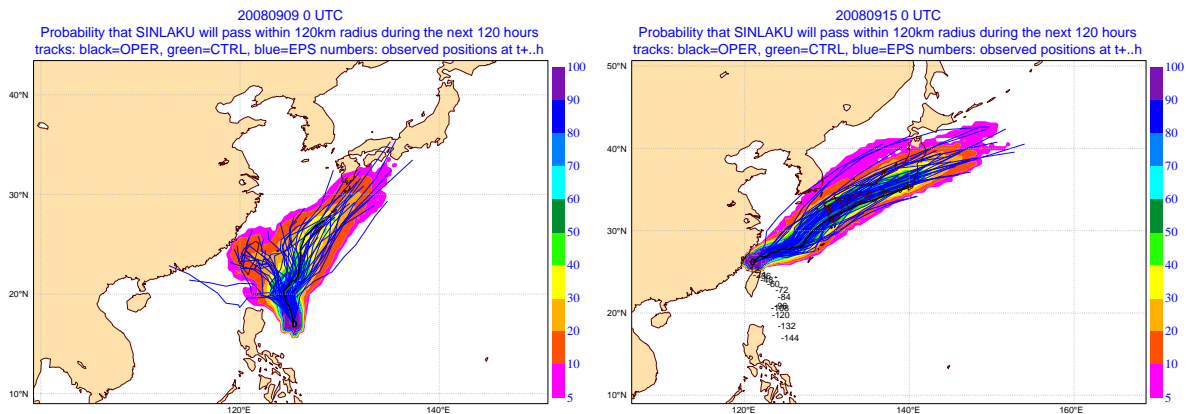


**Figure 3.5:** Strike probability map of Typhoon Sinlaku produced by the operational ECMWF EPS valid on (a) 00 UTC 09 Sept 2008 and (b) 00 UTC 15 Sept 2008.<sup>1</sup>

observations are assimilated.

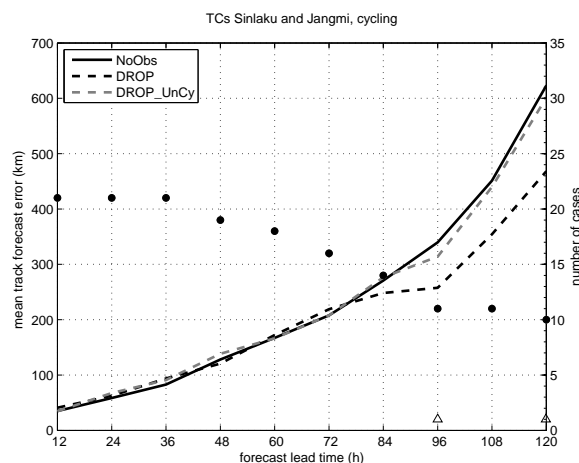


**Figure 3.6:** As in Fig. 3.2a, but the DROP\_UnCy (grey, dashed) experiment is included and only times are evaluated when additional observations are available. Empty (filled) triangles show forecast lead times when the mean track error differences of DROP and NoObs are significant at 90% (95%) confidence level.

### 3.4 Importance of correct observation times

In the operational ECMWF assimilation system, significant differences were discovered between the time T-PARC dropsondes were launched from the aircraft and the time they

<sup>1</sup>Figure available at [http://www.ecmwf.int/products/forecasts/d/charts/medium/tropcyclones/Forecast/strike!2008!19W\\_SINLAKU\\_04](http://www.ecmwf.int/products/forecasts/d/charts/medium/tropcyclones/Forecast/strike!2008!19W_SINLAKU_04)

were assimilated. These time differences were as large as four hours for single dropsondes (Fig. 3.7a). The largest values were found for sondes released by the WC-130 and NRL P-3 aircraft during flights in the centre region of Typhoon Sinlaku. The discovered time differences, that resulted from wrong time stamps in the header of the dropsonde data, were corrected retrospectively for all dropsondes used in OSEs for the T-PARC period. Note that not only T-PARC dropsondes were affected and dropsondes released in the Atlantic basin had similar time errors. However, the time errors did not occur at other weather centres due to the use of a different (correct) time stamp and hence, the time stamp used in the operational procedure at ECMWF was changed in July 2009.

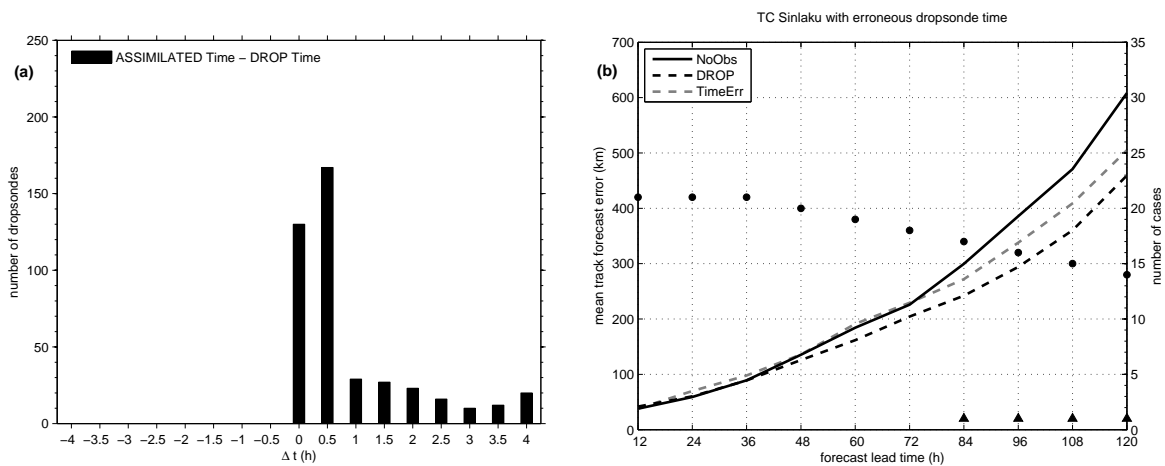


**Figure 3.7:** (a) Histogram of the difference between assimilation and launch time of T-PARC dropsondes in the period 00 UTC 09 Sept - 00 UTC 19 Sept 2008. (b) As in Fig. 3.3a, but including the mean track forecast errors for Typhoon Sinlaku of TimeErr (grey, dashed). Black dots represent the number of cases evaluated at each forecast lead time.

Particularly in the vicinity of a TC, strong gradients of wind and moisture and varying atmospheric conditions within short time scales can be present. Thus, dropsonde observations with an erroneous time may deteriorate some of the forecasts. An additional experiment, called TimeErr, is setup which is similar to DROP except that the erroneous dropsonde times are used. TimeErr is performed for the period between 00 UTC 09 Sept 2008 and 00 UTC 19 Sept 2008 to address the influence of the correct observation time on the track forecasts of Typhoon Sinlaku. The assignment of a wrong time to the dropsonde observation limits the forecast influence of the data and the mean track forecast error for Sinlaku in TimeErr is not reduced as much as in DROP even the same observations are assimilated in both experiments (Fig. 3.7b). Track improvements in TimeErr, which are not statistical significant, are achieved not until +84 h. In contrast, improvements of DROP start at shorter forecast times and are significant from +84 h onwards.

## 3.5 Discussion and conclusion

The overall influence of adaptive observations (dropsondes, extra TEMPs and SYNOPs deployed during T-PARC) on typhoon track forecasts was evaluated. Different OSEs were performed for the period of Typhoons Sinlaku and Jangmi between 09 Sept 2008 and 01 Oct 2008.

The mean 12-120 hour track forecast error for Sinlaku and Jangmi together is reduced by 15% when adaptive T-PARC observations are assimilated. While no mean improvements are found for shorter forecast lead times ( $\leq 72$  h), statistical significant improvements are present at longer forecast lead times ( $\geq 84$  h). The impact of T-PARC dropsondes is different between the two storms and between their pre- and post-recurvature stages. Forecast initialised before the recurvature / landfall of Typhoon Sinlaku, when the uncertainty of the track forecast is largest, are the most beneficial cases. The magnitude of the identified improvements is similar to values discovered in previous studies on the impact of adaptive dropsondes in the western North Pacific (Wu et al., 2007b; Yamaguchi et al., 2009). The improvements of the track forecasts in the ECMWF model are found to be smaller than in other NWP models for the T-PARC dropsondes (Weissmann et al., 2011). The already smaller track forecast errors of the ECMWF model without dropsondes, that are likely due to the extensive use of satellite data and the 4-D Var data assimilation, appear to reduce the benefit gained from targeted observations compared to other models using less satellite data and 3-D Var data assimilation.

Significant differences exist between cycled and uncycled experiments. While the cycled experiment shows large improvements, the impact in the uncycled experiment is very small. During a field campaign such as T-PARC, adaptive observations are available at numerous, but in general not at all analysis times. Due to cycling, the ‘data impact’ of the observations remains in the model system and changes the background field for successive analysis times. The model system typically remembers observations for at least 4-5 successive analysis times which corresponds to 2-3 days. Differences in the background information affect the assimilation considerably because nearly 85% of the information is provided by the background and only approximately 15% by the observations (Cardinali et al., 2004). The cycling procedure leads to an overall amplification of the forecast influence of adaptive observations, however, the amplification does not necessarily have to be positive (Irvine et al., 2009; Aberson, 2010). A disadvantage of the cycling procedure is that the influence of adaptive observations at the current analysis time can not be evaluated clearly since the differences between the experiments arise from the different set of observations as well as from the different background information used in the data assimilation.

The correction of a time error of the T-PARC dropsondes leads to a clear improvement

of TC track forecasts. Hence, an erroneous assigned dropsonde time limits the value of observation in the operational 4D-Var data assimilation system. Following these results, the correction of the dropsonde observation time is also applied in the operational ECMWF setup after the T-PARC campaign and it may be expected that the ECMWF TC track forecast error will be reduced further compared to the record-setting performance in 2008 (Fiorino, 2009).

## Chapter 4

# Strategies for adaptive tropical cyclone observations

### 4.1 Introduction

The following chapter investigates the benefit of T-PARC dropsonde observations in different locations on the basis of OSEs with the ECMWF global model. In these experiments, the division of dropsondes into different subsets should yield information about the importance of observations in certain areas relative to the position of the TC.

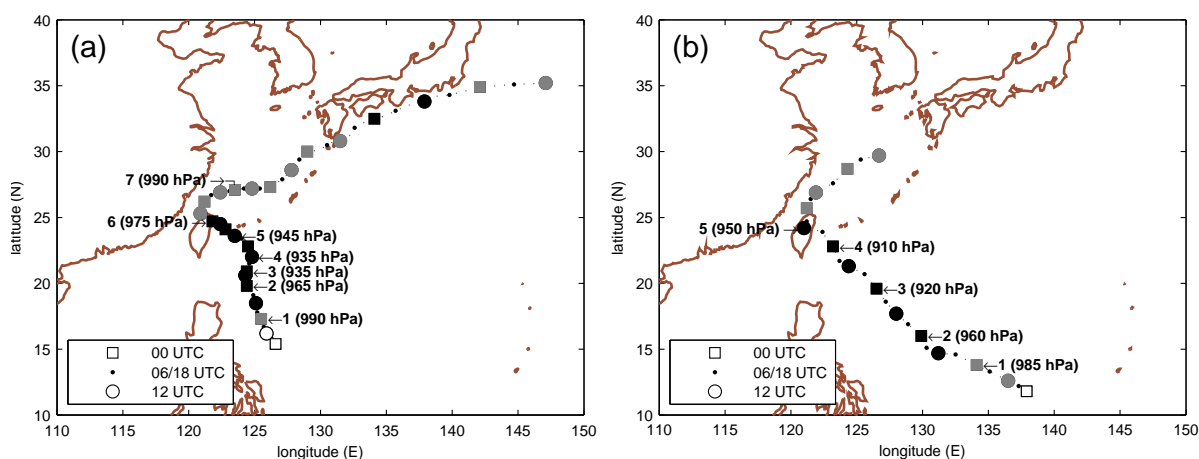


**Figure 4.1:** JMA best track data of (a) Typhoon Sinlaku from its genesis on 8 Sept 2008 until its extratropical transition on 20 Sept 2008 and (b) Typhoon Jangmi from 24 Sept 2008 until 30 Sept 2008. Rectangles indicate the position of the typhoon at 00 UTC, circles at 12 UTC and dots at 06 UTC and 18 UTC, respectively. The shading of the markers indicates the classification of the TC: “black” typhoon intensity and “grey” tropical or severe tropical storm. Times with data denial experiments are emphasised by the corresponding case number (see also Table 4.1) and the central mean sea level pressure.

Two major typhoon systems during the T-PARC period are investigated in this chapter, Typhoon Sinlaku and Typhoon Jangmi (Fig. 4.1). Sinlaku developed around 08 September 2008 east of the Philippines. The storm moved slowly northwards to the west of the subtropical anticyclone and hit Taiwan on 14 September. After recurving between Taiwan and China, Sinlaku first struggled to speed up, but then moved on towards Japan with the subtropical anticyclone to the southeast. The storm re-intensified again before passing south of Japan and then transitioned to an extratropical system. Seven cases in the period 09-16 September were chosen for OSEs (Fig. 4.1a). Typhoon Jangmi developed between Guam and the Philippines around 23 September, then moved to the northwest and struck Taiwan on 28 September. Jangmi experienced a strong weakening during landfall, recurved close to the Chinese coast and afterwards dissolved south of Japan. Five times were selected for data denial experiments in the period 25-28 September (Fig. 4.1b).

Section 4.2 gives a description of the setup of the OSEs. Results of the track and intensity forecasts of Sinlaku and Jangmi verified against the JMA best track data and statistics of the assimilation of dropsondes released in the centre and core of Typhoon Sinlaku are shown in section 4.3. The discussion and conclusion is presented in section 4.4.

## 4.2 Experimental design

The OSEs were performed using the ECMWF IFS. A detailed description of the setup is given in section 4.2. Observations of wind, temperature and specific humidity from dropsondes were fed into the ECMWF data assimilation system after correcting dropsonde timing errors that occurred in the operational ECMWF assimilation. A control run (NoObs) without any dropsonde observations was performed for the whole period of Typhoon Sinlaku and Typhoon Jangmi. Additionally, uncycled experiments initialised from the control run that use certain parts of the observations or all observations were conducted for selected cases. These cases were chosen under the conditions of a strong typhoon and a large number of dropsonde data in the area of the storm. OSEs were performed to investigate the sensitivity of the model analysis and forecast to observations taken in three distinct areas relative to the TC position. Figure 4.2 presents a schematic picture of the partitioning of the observations. The shading indicates a sensitivity pattern often highlighted by SV calculations during T-PARC with sensitivity maxima 700-1200 km away from the TC centre. The DLR Falcon mainly sampled these sensitive regions. The observations in the core and centre primarily consist of WC-130 dropsondes, while the observations in the vicinity of the typhoon were primarily taken by the DOTSTAR aircraft. In addition, the DOTSTAR aircraft also covered parts of the sensitive regions on several days. The different subsets of observations also contain a small number of NRL P-3 dropsondes in some cases. Note here

that the DOTSTAR aircraft and the DLR Falcon were flying in the upper troposphere, while the NRL P-3 and the WC-130 were mainly flying in the lower troposphere for the dropsonde deployment on the days discussed in this study. Experiments are carried out with observations in remote sensitive regions (ReObs), with observations in the vicinity of the typhoon (ViObs) and with observations in the centre and core region (CeObs).

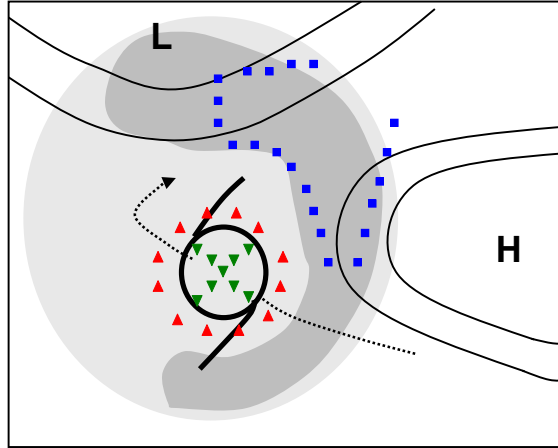


**Figure 4.2:** Idealised sketch illustrating the separation of the dropsondes into different subsets. Dropsonde positions are labeled by downward-pointing triangles (core and centre of the TC), squares (remote sensitive region) and upward-pointing triangles (vicinity of the TC), respectively. Shading indicates the typical pattern of regions with high (dark grey) and moderate (light grey) sensitivity during T-PARC period calculated by SVs. Solid lines mark possible streamlines, representing the midlatitude flow north of the TC and the subtropical anticyclone to the east. The trajectory of the TC is shown as dotted line.

In practice, this clear separation of observations is not always as unambiguous as shown in Fig. 4.2 and is partly based on a subjective assessment. An argument for the separation of the observations evolves from the targeting guidance. Several targeting guidance products, ranging from SV calculations of different models over ETKF products to adjoint calculations, were available during T-PARC. An example of two targeting guidance products valid at 12 UTC 11 Sept is shown in Fig. 4.3. Sinlaku is located southeast of Taiwan (see also Fig. 4.1) and the predicted position of landfall on Taiwan and recurvature is uncertain. Similar sensitivity patterns are frequently identified before recurvature of Typhoons Sinlaku and Jangmi. SV calculations indicate maximum sensitivity to the north and northeast of Sinlaku linked to the interface of the storm with the midlatitude flow and the edge of the subtropical ridge to the east. A second maximum upstream indicates sensitivity to the approaching trough structure over northern China. The sensitivity is lower close to the TC and a relative minimum is visible next to the TC centre. In contrast, the

ETKF computation shows a sensitivity maximum at the centre of the TC. The sensitivity decreases with distance to the storm and is elongated from the southwest to the northeast. At that targeting time, two aircraft were flying and dropsondes were released north of the TC (ReObs) and close to the centre and core of the TC (CeObs).

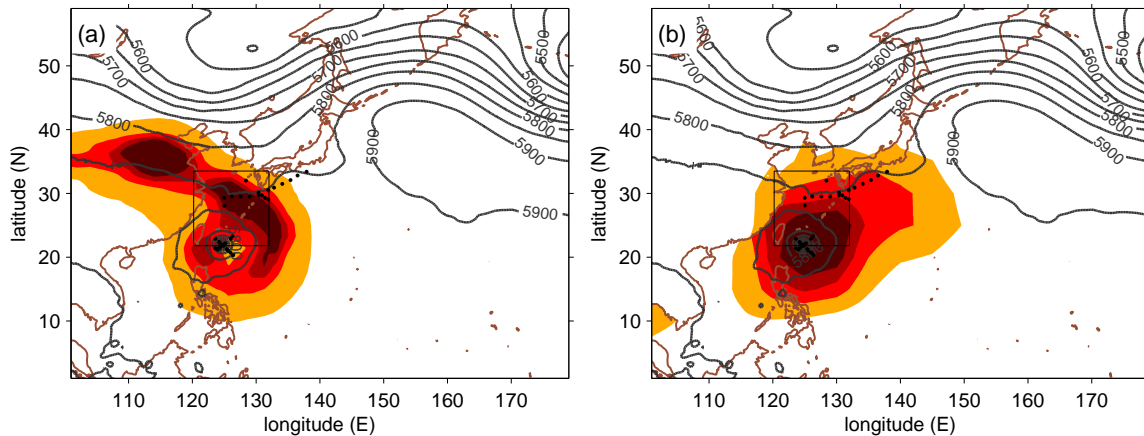


**Figure 4.3:** Targeting guidance for Typhoon Sinlaku valid at 12 UTC 11 Sept initialised at 00 UTC 09 Sept with +36 h optimization time. The areas of  $1, 2, 4,$  and  $8 \cdot 10^6 \text{ km}^2$  are shaded. (a) SV based calculation of the ECMWF model and (b) ETKF multimodel (NCEP/ECMWF/CMC) ensemble output. The verification region (black box) is centred around the expected position of the TC. Black contour lines show the geopotential height at 500 hPa and black dots the location of dropsondes.

Figure 4.4 and Table 4.1 show the available dropsonde data for all selected cases. The number of soundings used for the individual experiments varies from 9 to 37. When observations were separated into two or three subsets, an additional uncycled experiment using all observations (AllObs) was performed.

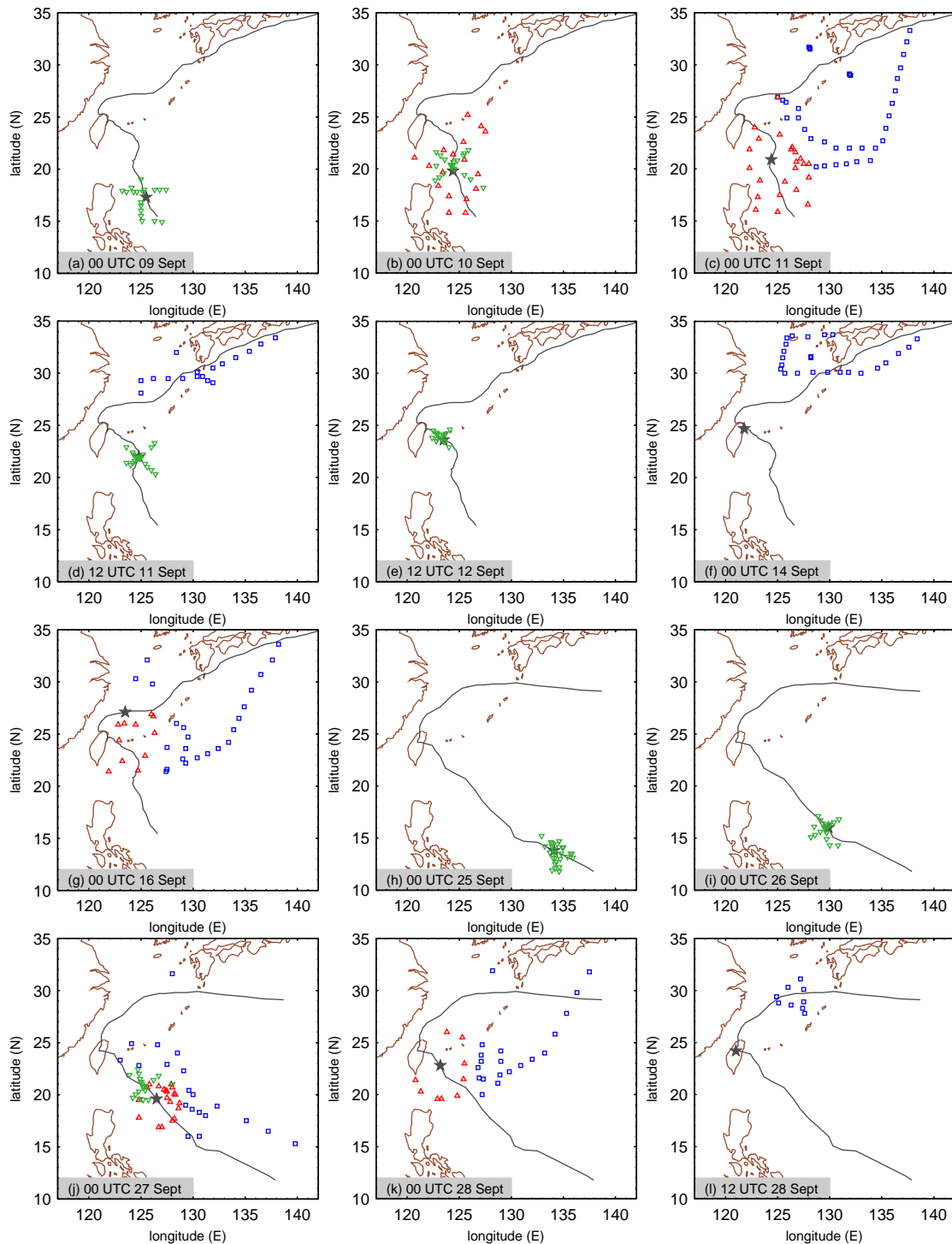


**Figure 4.4:** Position of dropsondes used in the OSEs for (a)-(g) Typhoon Sinlaku and (h)-(l) Typhoon Jangmi (see also Table 4.1); best track of the respective typhoons (solid grey line) and the actual position of the storm (grey asterisks). Note that the storm position at the nominal analysis time is displayed, while the dropsondes can be distributed within the 12-hourly assimilation window. Squares, upward-pointing triangles and downward-pointing triangles represent dropsondes of ReObs, ViObs and CeObs, respectively.

Case number	Initial date	Forecast times (h)	ReObs	ViObs	CeObs	AllObs
(1)	00 UTC 09 Sept	12-120			18	
(2)	00 UTC 10 Sept	12-120		17	20	37
(3)	00 UTC 11 Sept	12-120	37	22		59
(4)	12 UTC 11 Sept	12-120	17		19	36
(5)	12 UTC 12 Sept	12-120			22	
(6)	00 UTC 14 Sept	12-120	25			
(7)	00 UTC 16 Sept	12-108	23	11		34
(8)	00 UTC 25 Sept	12-120			26	
(9)	00 UTC 26 Sept	12-84			19	
(10)	00 UTC 27 Sept	12-84	20	20	20	60
(11)	00 UTC 28 Sept	12-60	20	9		29
(12)	12 UTC 28 Sept	12-48	9			

**Table 4.1:** Overview of number of dropsondes in different experiments. Forecast times denote the interval in which the track forecasts of the Typhoons Sinlaku and Jangmi (2008) are evaluated. Case numbers refer to the best tracks shown in Fig. 4.1.

## 4.3 Results

### 4.3.1 Assimilation statistics of TC centre and core observations

The WC-130 conducted several flights penetrating Sinlaku and Jangmi and released dropsondes in the core and eye wall region. OSEs only using these observations (CeObs) were performed four times during Typhoon Sinlaku and three times during Typhoon Jangmi (Table 4.1) to investigate the benefit of such observations.

CeObs dropsondes were often released on two straight flight legs crossing the typhoon. In the example shown in Fig. 4.5a, nearly 50% of the wind observations are detected and flagged by VarQC, which reduces the weight of observations in the analysis. In practice, the flagged observations have very low weights and are basically not used. As mentioned above the BgQC is relaxed for TC sondes and effectively inactive (Table 4.2). Similar rejection rates are also seen for other analysis times with CeObs observations.

The average wind speed innovation of each single sounding (difference between the wind speed observations from one sounding and the model background field) is plotted in Fig. 4.5b. All dropsondes show significantly higher wind speeds compared to the model

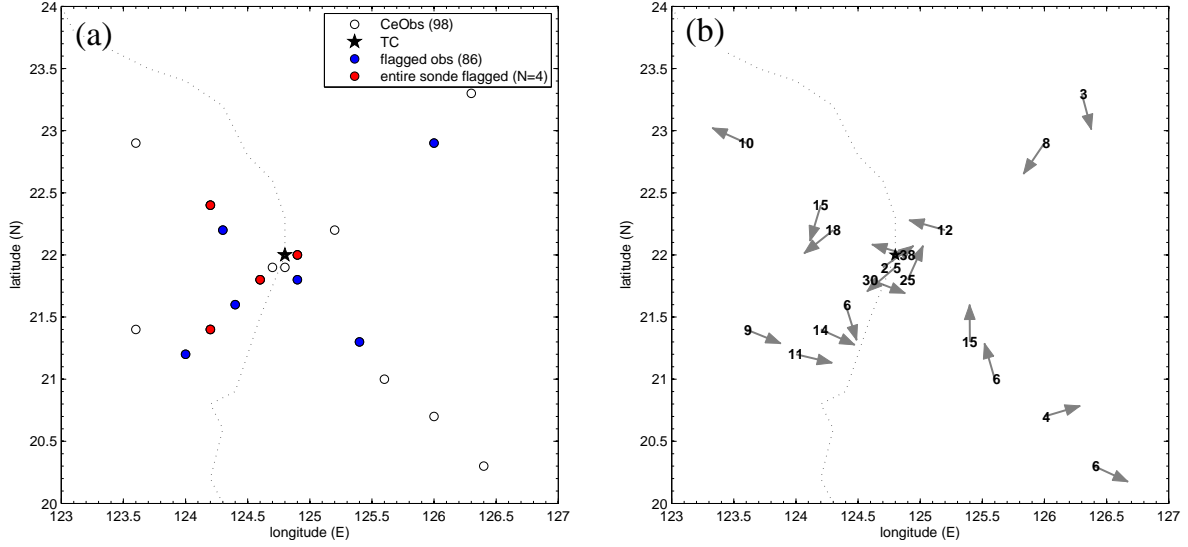


**Figure 4.5:** Wind observations of dropsondes used for the CeObs subset at 12 UTC 11 Sept. (a) Position of the dropsondes; white shading indicates that all wind observations of the sounding are used, blue shading that they are partially used, and red shading that all wind observations from the sounding are flagged by VarQC. (b) Innovations (difference of observed value and model background) averaged over every dropsonde between 650 hPa and 1000 hPa for wind speed in  $\text{m s}^{-1}$  and wind direction (grey arrows).

	all data	no flag	data flagged by	
			BgQC	VarQC
wind speed	184	98	0	86
temperature	113	98	0	15
spec. humidity	123	122	0	1

**Table 4.2:** Number of dropsonde wind, temperature and specific humidity observations included in CeObs at 12 UTC 11 Sept.

background field and enhance the developed cyclonic wind structure around the TC. The histogram of the wind speed innovations (Fig. 4.6a) shows a high number of innovations exceeding  $10 \text{ m s}^{-1}$ . Most of these large innovations are high wind speeds in the eye wall region. Innovation values of more than  $15 \text{ m s}^{-1}$  appear too extreme for the data assimilation and are rejected by VarQC. The distribution of accepted wind speed innovations still has a positive mean value of  $3.8 \text{ m s}^{-1}$  but is of more Gaussian shape as the positive extremes are rejected by the VarQC.

The vertical distribution of the wind speed innovations is shown in Fig. 4.6b. During the crossing of the TC centre, the WC-130 was flying at low levels. Thus, sounding data

are only available below 700 hPa. Innovations larger than  $10 \text{ m s}^{-1}$  can be identified above the surface layer. After the VarQC procedure, the innovation values are reduced to less than  $5 \text{ m s}^{-1}$ , but the used observations still lead to an intensification of the cyclonic wind speeds at most levels.

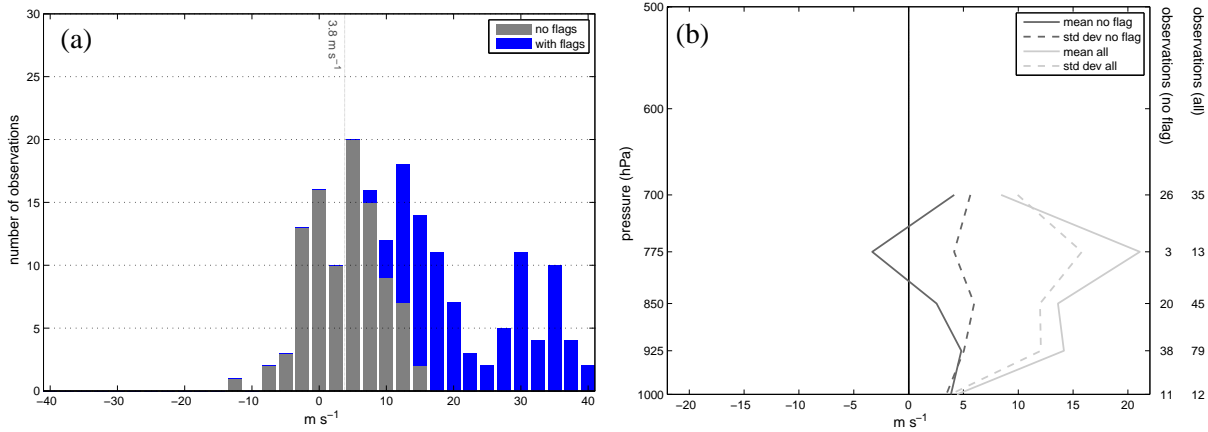


**Figure 4.6:** Innovations of observed wind speeds for soundings displayed in Fig. 4.5 at 12 UTC 11 Sept. (a) Histogram of wind speed innovations. The vertical line illustrates the mean value of used data. (b) Vertical profile of standard deviation and mean of all and used (no flag) innovations.

In contrast to wind speed, humidity and temperature observations show much lower innovations (not shown) and a larger percentage of the data are used (Table 4.2).

### 4.3.2 Typhoon track forecasts

#### Pre-recurvature period

During the pre-recurvature stage of Sinlaku (09-14 September), high forecast uncertainty is linked to the location of landfall and recurvature and to the predicted movement of the system after recurvature. This period also shows the largest influence of dropsondes on the track forecast (Fig. 4.7). In the following, individual cases, representative for the other times, are discussed.

The first case of Sinlaku (00 UTC 09 Sept, Fig. 4.7a) is at the time of the beginning intensification. CeObs produces an improvement of the predicted storm track and a 12-120 hour mean track forecast error reduction of 24% is achieved. The storm is classified as a tropical storm with a central pressure of 990 hPa (Fig. 4.1a) which causes moderate innovations of wind speed ( $< 10 \text{ m s}^{-1}$ ) and only 3 observations are flagged and rejected (Fig. 4.8a). Figure 4.8b shows that CeObs increases the low level wind speed around Sinlaku (located at  $\sim 125.5^\circ\text{E}$ ). Even though the dropsondes in CeObs are located in the

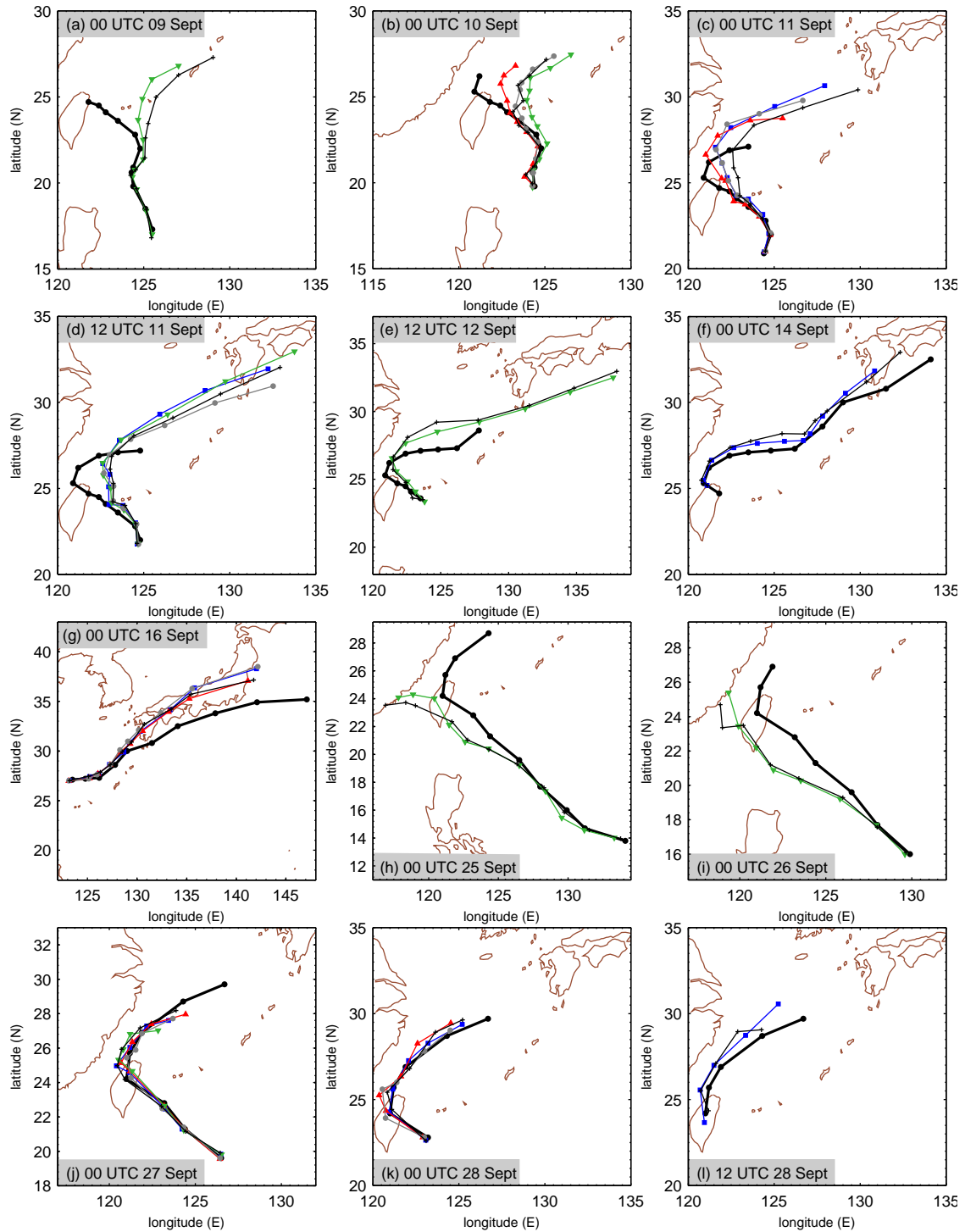


**Figure 4.7:** Track forecasts of all experiments for (a)-(g) Typhoon Sinlaku and (h)-(l) Typhoon Jangmi (see also Table 4.1). TC positions are plotted every 12 hours. Black solid dots display the best track data. Squares, upward-pointing triangles, downward-pointing triangles and circles represent forecasts of ReObs, ViObs, CeObs and Allobs, respectively. Cross symbols show the forecast of NoObs. Corresponding track forecast errors can be found in Table 4.3 and 4.4.

date	exp	12 h	24 h	36 h	48 h	60 h	72 h	84 h	96 h	108 h	120 h	Mean
00 UTC 09 Sept	CeObs	16	29	29	19	73	59	120	232	353	573	<b>150</b>
	NoObs	10	26	19	21	68	65	181	312	504	778	198
00 UTC 10 Sept	ViObs	57	24	26	61	13	18	51	134	202	219	<b>80</b>
	CeObs	18	59	47	54	80	141	197	284	467	545	189
	AllObs	3	55	46	72	24	64	155	225	370	448	146
	NoObs	45	9	7	52	28	34	141	197	338	400	125
00 UTC 11 Sept	ReObs	13	44	51	18	91	161	208	257	382	585	<b>181</b>
	ViObs	4	47	26	25	73	65	150	179	227	269	<b>106</b>
	AllObs	10	51	44	19	70	163	195	267	291	430	<b>154</b>
	NoObs	10	23	22	27	102	155	246	353	500	722	216
12 UTC 11 Sept	ReObs	23	55	19	87	176	214	296	439	634	891	<b>283</b>
	CeObs	14	40	35	89	146	216	306	474	760	1074	<b>315</b>
	AllObs	17	43	48	111	160	282	353	423	637	858	<b>293</b>
	NoObs	18	62	45	123	201	284	380	488	693	952	325
12 UTC 12 Sept	CeObs	34	42	98	147	202	292	486	709	928	1041	<b>398</b>
	NoObs	54	30	117	163	250	341	487	747	967	1084	424
00 UTC 14 Sept	ReObs	18	51	57	78	99	73	84	144	227	315	115
	NoObs	24	44	54	73	127	111	55	105	117	172	88
00 UTC 16 Sept	ReObs	48	47	55	34	217	358	422	592	566	-	260
	ViObs	41	47	50	68	209	336	436	623	571	-	265
	AllObs	33	43	49	71	232	372	508	611	570	-	277
	NoObs	43	63	48	48	196	316	413	611	525	-	252

**Table 4.3:** Track forecast errors (km) of all cases for Typhoon Sinlaku (2008). Boldface numbers indicate cases where a reduction of the mean 12 to 120 hour track forecast error compared to NoObs is achieved.

lower troposphere, the CeObs analysis increments extend into the upper troposphere and modify the wind and the temperature fields (Fig. 4.8b).

At 00 UTC 10 Sept (Fig. 4.7b), observations located in the vicinity of the storm (ViObs) lead to a much better track forecast compared to the control run. With these observations, the storm forecast is shifted further to the west, which is closer to the best track. A 12-120 hour mean track forecast error reduction of 36% is obtained. In contrast, the track forecast of CeObs shows an eastward shift of the typhoon track. The track of CeObs is worse than the one of NoObs and leads to an average 12-120 hour track forecast error increase of 51%. AllObs is still dominated by the negative effect of the CeObs observations which results in a mean 12-120 hour track forecast degradation of 17%.

The analysis of CeObs shows a stronger developed typhoon with higher wind speeds at 850 hPa on the southwestern side of the storm compared to NoObs (Figs. 4.9a,d). While this region of increased wind speed can be identified also in AllObs (Fig. 4.9c), it is not apparent in ViObs (Fig. 4.9b). The increased cyclonic low level winds in the southwestern sector of the TC apparently do not have a positive effect on the track forecast. The deep-layer environmental flow seems to be of higher importance for the steering of the

date	exp	12 h	24 h	36 h	48 h	60 h	72 h	84 h	96 h	108 h	120 h	Mean
00 UTC	CeObs	15	72	55	43	99	219	237	203	419	823	<b>219</b>
25 Sept	NoObs	36	24	30	36	104	201	217	326	502	935	241
00 UTC	CeObs	7	83	145	248	224	283	306	-	-	-	<b>185</b>
26 Sept	NoObs	15	64	141	230	114	344	391	-	-	-	186
00 UTC	ReObs	17	39	<i>45</i>	113	118	261	393	-	-	-	141
27 Sept	ViObs	7	19	<i>54</i>	81	83	232	293	-	-	-	<b>110</b>
	CeObs	11	18	<i>62</i>	79	153	369	482	-	-	-	168
	AllObs	13	37	<i>28</i>	35	118	314	367	-	-	-	<b>130</b>
	NoObs	18	27	<i>10</i>	109	159	299	322	-	-	-	135
00 UTC	ReObs	<i>11</i>	10	44	118	150	-	-	-	-	-	67
28 Sept	ViObs	<i>30</i>	97	66	173	211	-	-	-	-	-	116
	AllObs	<i>40</i>	66	112	159	226	-	-	-	-	-	121
	NoObs	<i>28</i>	48	26	69	144	-	-	-	-	-	63
12 UTC	ReObs	53	41	95	170	-	-	-	-	-	-	<b>90</b>
28 Sept	NoObs	52	37	141	247	-	-	-	-	-	-	119

**Table 4.4:** Track forecast errors (km) of all cases for Typhoon Jangmi (2008). Italic number indicate that the storm was located directly over Taiwan at this time and the storm position was estimated by the minimum of the geopotential height at 700 hPa instead of the minimum MSLP. Boldface numbers indicate cases where a reduction of the mean 12 to 120 hour track forecast error compared to NoObs is achieved.

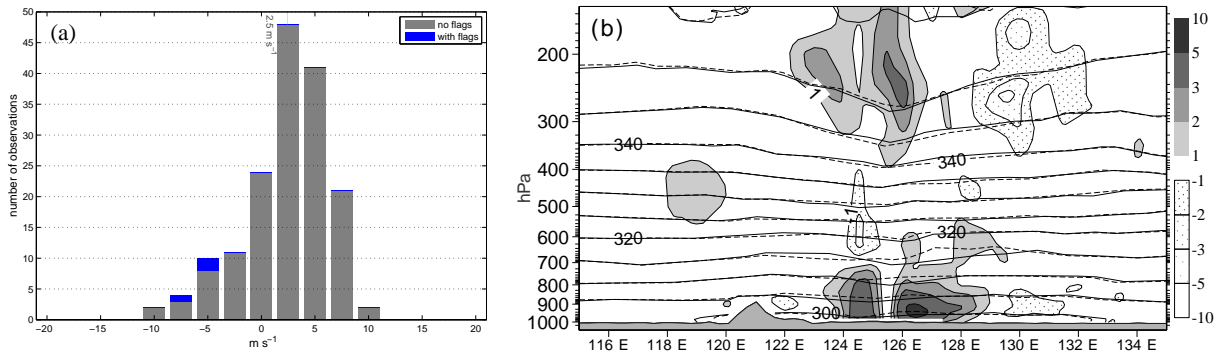


**Figure 4.8:** (a) Histogram of wind speed innovations for soundings displayed in Fig. 4.4a at 00 UTC 09 Sept. (b) Cross-section of the analysis valid at 09 UTC 10 Sept. The cross-section is located at  $16.9^{\circ}\text{N}$  which is approximately the centre of the TC in the experiments and ranges from  $115^{\circ}\text{E}$  to  $135^{\circ}\text{E}$ . The wind speed difference ( $\text{m s}^{-1}$ ) of CeObs and NoObs (shaded) are plotted with positive values indicating higher wind speeds in CeObs. Solid (dashed) lines show the analysis of the isentropes in K of CeObs (NoObs). Gray shading at the bottom represents the topography.

typhoon. Figure 4.10 illustrates the analysis of the geopotential height at 500 hPa for the experiments and NoObs as well as the deep-layer (850-300 hPa) mean wind difference between the experiments and NoObs. CeObs (Fig. 4.10a) shows a less distinct edge of the subtropical high east of Sinlaku and a larger eastward flow component southeast of the

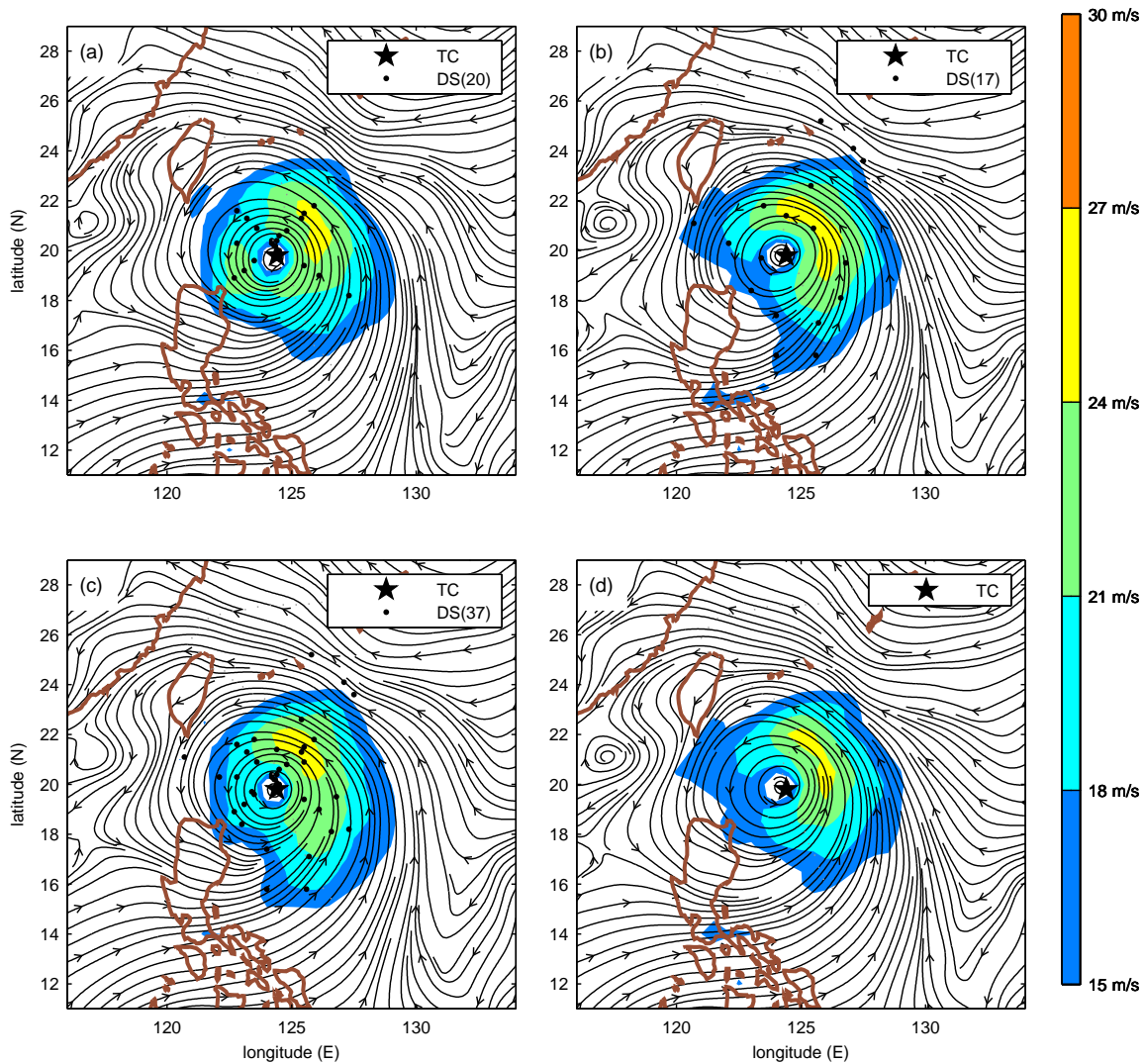


**Figure 4.9:** Analysis of streamlines and wind speed (shading) at 850 hPa at 00 UTC 10 Sept for (a) CeObs, (b) ViObs, (c) AllObs and (d) NoObs. The best track position of the TC is indicated by a black asterisk and the location of the dropsondes by black dots.

storm than NoObs. In ViObs (Fig. 4.10b), the flow southeast of the storm contains a larger westward component, which seems to shift the track further to the west and produces a better track forecast. A more northward wind component to the southeast of Sinlaku can be identified in AllObs (Fig. 4.10c). The ECMWF SV calculation also shows a band of maximum sensitivity south and east of Sinlaku (Fig. 4.11a), which confirms the sensitivity

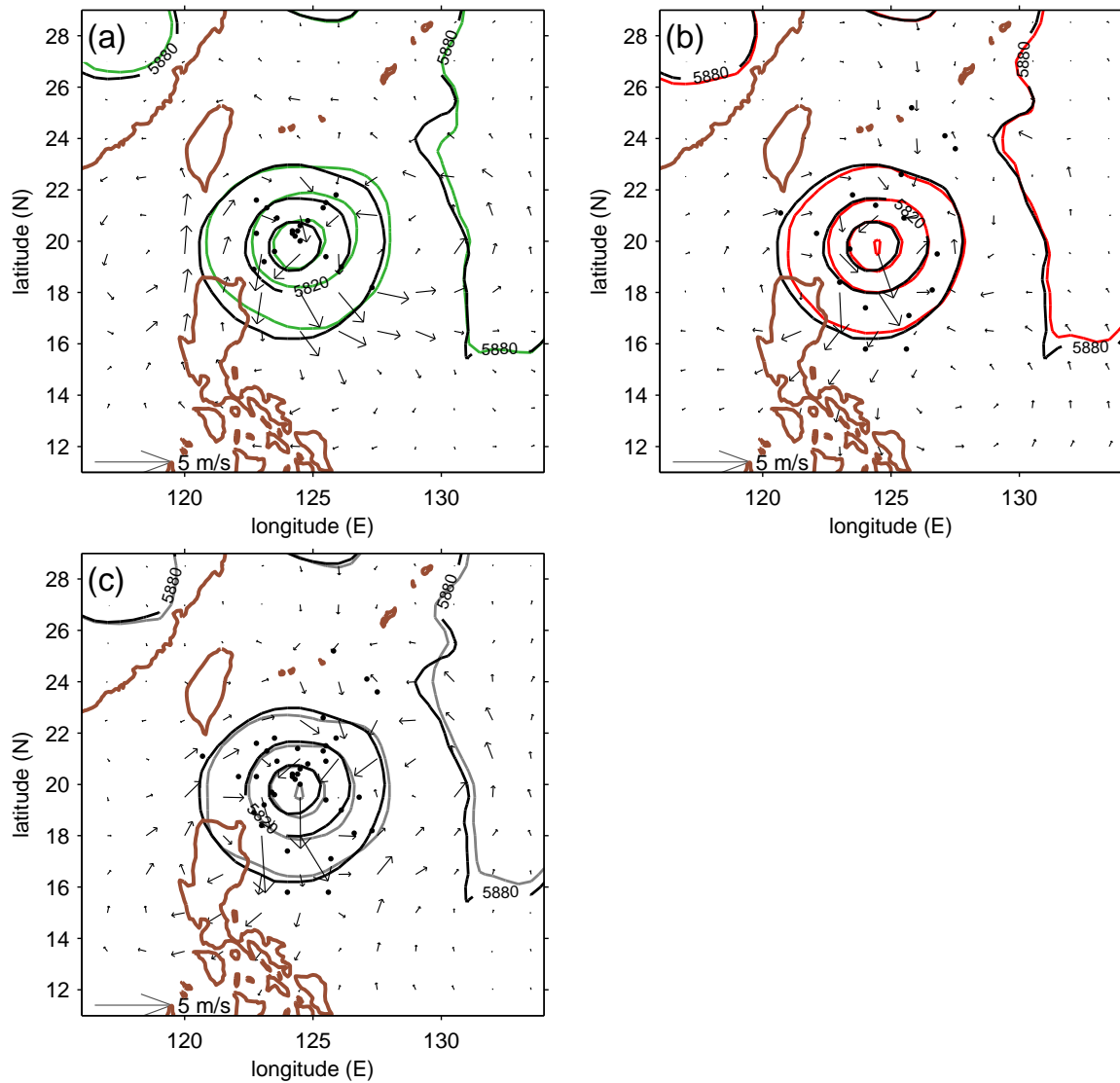


**Figure 4.10:** Analysis valid at 00 UTC 10 Sept for (a) CeObs, (b) ViObs and (c) AllObs. The geopotential height at 500 hPa is plotted with coloured contour lines for the corresponding experiments and with black contour lines for NoObs. Arrows indicate the difference of the deep-layer (850-300 hPa) mean wind field between the experiments and NoObs. The position of drizzle is indicated by black dots.

of the steering flow in the region south and east of Sinlaku.

The +72 h forecasts of the geopotential height at 500 hPa and the deep-layer mean wind is displayed in Fig. 4.12. The time step corresponds to the time when the track forecasts of the different experiments start to diverge (compare also Fig. 4.7b). The forecast shows differences of the edge of the subtropical high to the east of Sinlaku as well as of the position

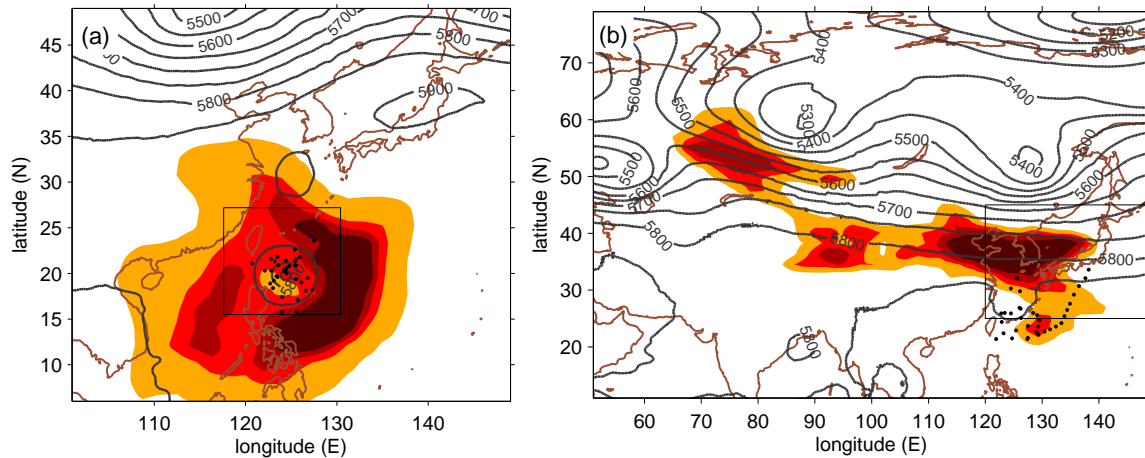


**Figure 4.11:** Targeting guidance based on SV calculation of the ECMWF model for Typhoon Sinlaku valid at (a) 00 UTC 10 Sept initialised at 00 UTC 08 Sept with +48 h optimization time, and (b) 00 UTC 16 Sept initialised at 00 UTC 14 Sept with +72 h optimization time. The areas of 1, 2, 4, and  $8 \cdot 10^6$  km<sup>2</sup> are shaded. The verification region is shown by a black box. Black contour lines show the geopotential height at 500 hPa and black dots the location of dropsondes.

of the storm. The subtropical high is developed weakest in CeObs (Fig. 4.12), which allows Sinlaku to move to the northeast. Highest wind speeds of the deep-layer mean wind are found east and northeast of Sinlaku in CeObs supporting the northeastward movement. Comparing AllObs and ViObs (Figs. 4.12b,c), one can identify differences in the structure of the storm and slightly higher wind speeds in ViObs west of Sinlaku, which seem to be responsible for the smaller track forecast errors in ViObs.

Observations in the vicinity of the typhoon again lead to an improved track forecast of Sinlaku initialised at 00 UTC 11 Sept (Fig. 4.7c). The track forecast of the control run is already very accurate up to +48 h, but the track forecast from 2 days onwards is improved with the ViObs observations. The landfall scenario of Sinlaku at the northern tip of Taiwan is predicted correctly and also the representation of the motion during recurvature is more similar to the best track scenario. ReObs at the same time shifts the track closer to the best track, but keeps the storm a little further to the east during recurvature (Fig. 4.7c). Again, the combination of the two subsets does not show the best performance and the 12-120 hour mean track forecast error reduction of AllObs is 28%, while 16% can be achieved with ReObs and 51% with ViObs. Despite the improvement of the track until the recurvature of the storm, the model seems to have problems with the propagation of Sinlaku after recurvature. From +84 h onwards, a timing error of all track forecasts is observed (Fig. 4.7c). Even if the track forecast error is reduced with extra observations, the error due to the acceleration of the storm is large and dominates.

Experiments for the pre-recurvature period of Typhoon Jangmi do not show such a

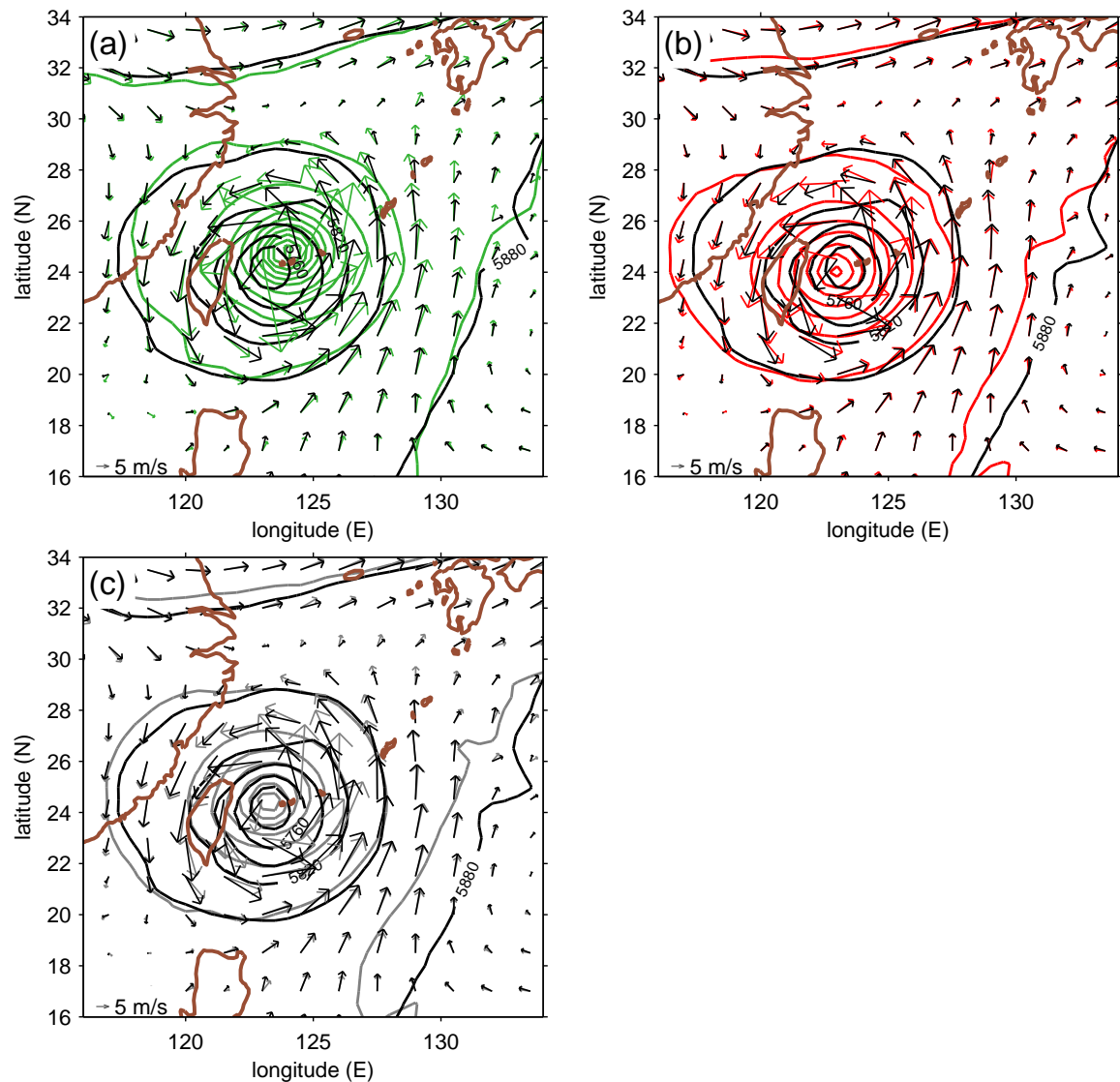


**Figure 4.12:** +72 h forecast initialised at 00 UTC 10 Sept for (a) CeObs, (b) ViObs and (c) AlloObs. The geopotential height at 500 hPa is plotted with coloured contour lines for the corresponding experiments and with black contour lines for NoObs. Coloured arrows indicate the deep-layer (850-300 hPa) mean wind field of the experiments and black arrows of NoObs.

positive influence as for Sinlaku. The southwestward bias of the track forecast is hardly corrected in CeObs during the early stages (Figs. 4.7h,i). However, no ViObs observations are available for these two cases. Results at 00 UTC 27 Sept indicate that the track forecast of NoObs is very accurate and landfall is predicted at the correct position. After landfall, all the experiments struggle to accelerate Jangmi. These propagation errors of Sinlaku and Jangmi after landfall and recurvature are likely linked to model deficiencies of the

land interaction of the typhoon and the connected structure change on its way over land rather than errors in the initial conditions. However, a better representation of the TC in the initial conditions due to extra observations can also lead to a more correct structure and track modification during the land passage (Wu, 2001). When the landfall point is represented best in the model, the errors due to land interaction can also be minimised resulting in smaller timing errors, as in ViObs initialised at 12 UTC 11 Sept.

### **Post-recurvature period**

The influence of the observations after recurvature is generally smaller than before recurvature. In several cases (Figs. 4.7f,g,l), NoObs already shows a very accurate track forecast. Slight modifications of the track forecast can be achieved with different subsets of observations, but no striking feature can be identified. During this stage of the TC propagation, the flow field upstream in the midlatitudes becomes more important for the track forecast and the influence of dropsondes in the TC environment seems to weaken.

Errors in the predicted upstream flow field appear to dominate the cases in the post-recurvature period of Sinlaku. The track forecast of ViObs, ReObs, AllObs and NoObs at 00 UTC 16 Sept is very accurate up to +48 h (Fig. 4.7g) with track errors less than 70 km (Table 4.4). After +48 h, the track errors of all experiments increase significantly, but there is only little difference between the experiments. Figure 4.13 shows that none of the experiments predicts the short wave trough and the flow structure over northern China at +48 h correctly. The differences between the forecasts of the experiments and NoObs seem negligible compared to the differences between the forecasts and the verifying analysis. The forecast error related to the trough structure evolves from a region far upstream over Western Siberia, which is also indicated to be sensitive by ECMWF SV calculations (Fig. 4.11b). This error is not affected by changes in the initial conditions close to the storm, which explains the low influence of dropsondes next to Sinlaku in this case.

The propagation error of Sinlaku after recurvature in the forecast initialised at 12 UTC 11 Sept is to some extent also related to errors in the upstream midlatitude flow (not shown).

### **Overall influence**

Scatter diagrams summarising the results for all individual cases are displayed in Fig. 4.14. The ViObs subset leads to the highest reduction of the track forecast errors. Large values of track error reduction could be achieved in most cases and the linear fit as well as the averaged values indicate a positive influence especially from 2 days onwards. In CeObs, the

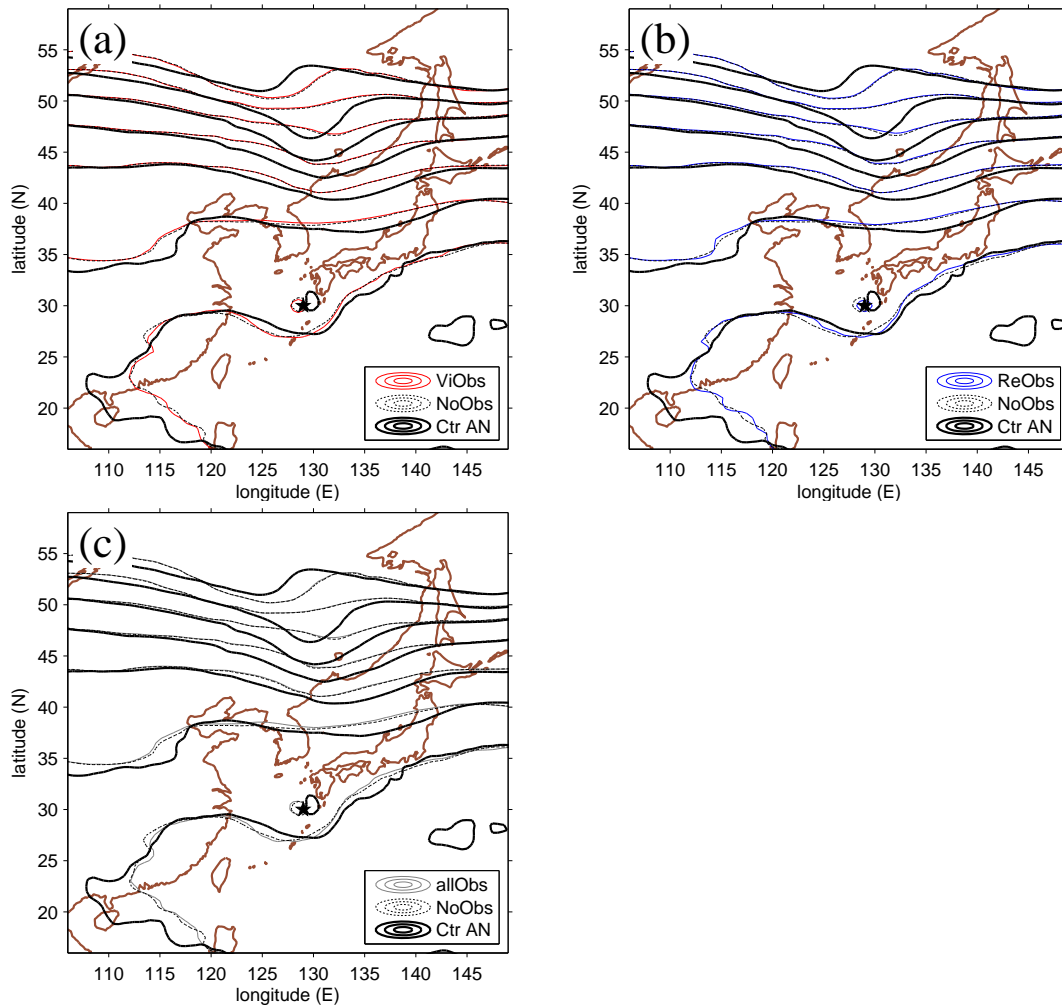


**Figure 4.13:** 500 hPa geopotential height field valid at 00 UTC 18 Sept. The +48 h forecast (solid coloured line) initialised at 00 UTC 16 Sept of (a) ViObs, (b) ReObs and (c) AllObs is compared against NoObs (dashed black line) and the verifying analysis (solid black line). The best track position of the TC is indicated by a black asterisk.

points are distributed around the diagonal. Average values as well as the linear fit show a slight positive influence of these observations overall, but large positive and negative outliers are apparent. For ReObs, the overall influence is rather neutral with a slight positive tendency, comparable to the CeObs results. Combining the subsets together does not automatically improve the track forecast more than when using only one subset. AllObs also shows a positive influence on average, but not as large as ViObs.

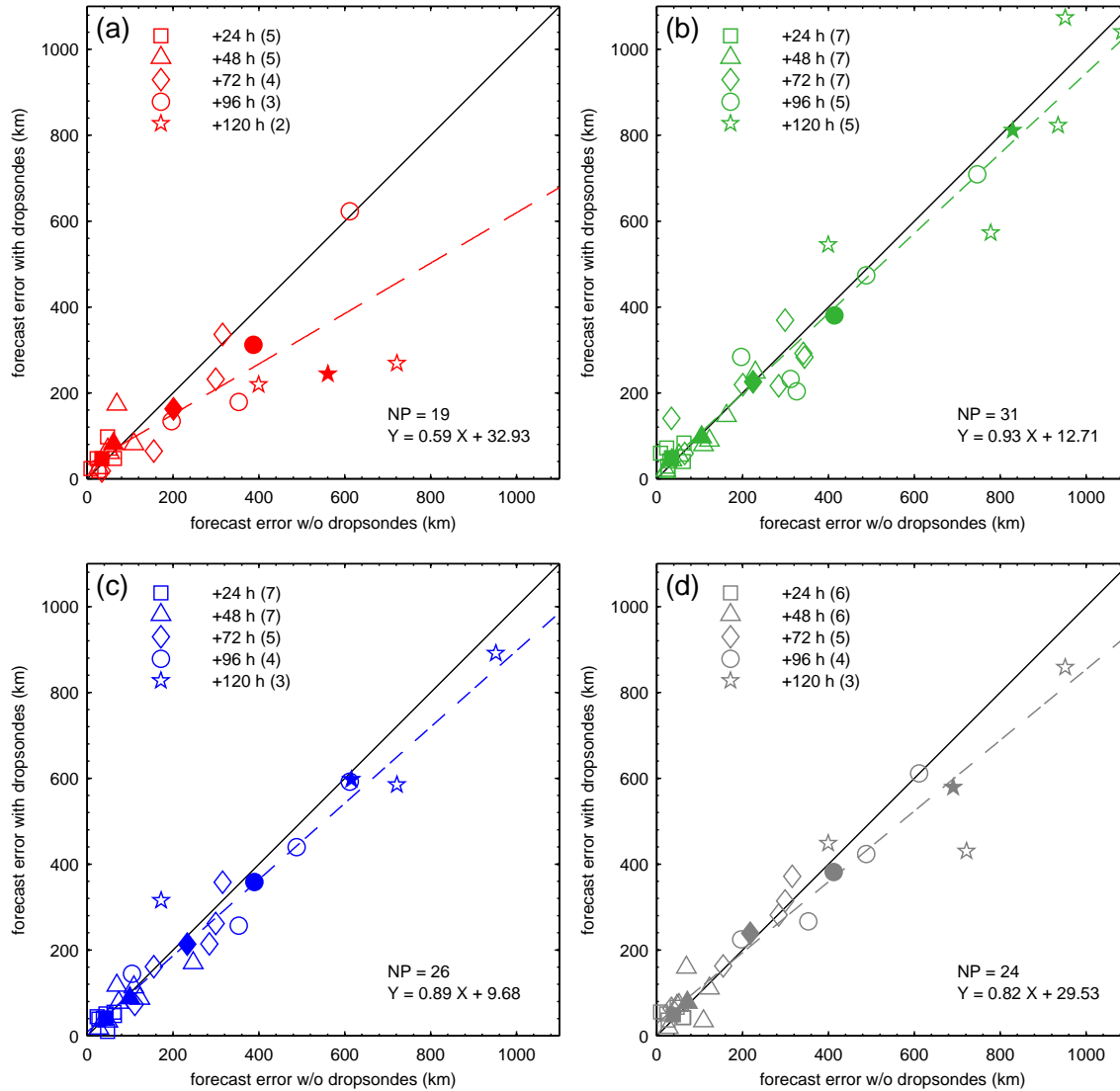


**Figure 4.14:** Scatter plots of track forecast errors of experiments against the control run. The x-axis shows the track errors of NoObs, and the y-axis the track errors of (a) ViObs, (b) CeObs, (c) ReObs and (d) AllObs. The solid black line represents the diagonal with values below indicating an error reduction and values above an error increase compared to the control run. Different markers indicate different forecast times. Filled markers represent mean values for the respective forecast step. The slope, the zero offset and the used number of points (NP) of the linear regression line (coloured dashed line) are displayed in the lower right.

### 4.3.3 Typhoon intensity forecast

The correct intensity forecast of the TC is of high importance. Large errors in the models are expected as global models with a resolution of 25 km or less can not fully resolve the

strong pressure gradient of a TC.

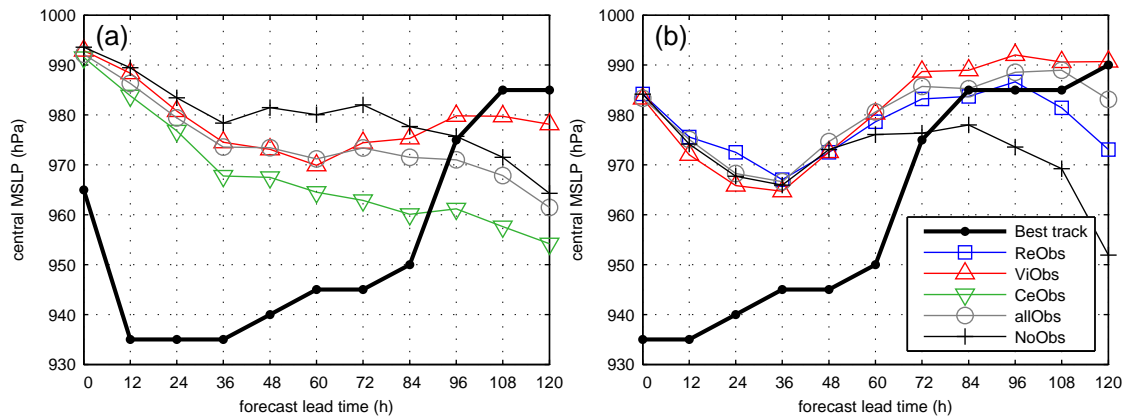


**Figure 4.15:** Best track data and central MSLP values of the experiment and control forecasts initialised at (a) 00 UTC 10 Sept and (b) 00 UTC 11 Sept.

Figure 4.15 shows two examples of central MSLP forecasts for Typhoon Sinlaku. According to best track data, Sinlaku reaches its minimum pressure of 935 hPa between 12 UTC 10 Sept and 12 UTC 11 Sept. All central MSLP forecasts show large errors up to 40 hPa during the most intense period. At 00 UTC 10 Sept (Fig. 4.15a), CeObs decreases the central pressure and the pressure error is reduced more than 10 hPa compared to NoObs. When Sinlaku is closer to land and begins to weaken at +84 h and +60 h, respectively, it is obvious that the correct track forecast has an essential influence on the central pressure. Even though CeObs reduces the central MSLP error in the short-range, the TC does not weaken from 3 days onwards due to the wrongly predicted track. In contrast, the improved track forecast of ViObs is partly capable of decaying the system because ViObs predicts Sinlaku closer to its real position near Taiwan (compare Fig. 4.7b). The experiments starting at 00 UTC 11 Sept (Fig. 4.15b) only have a limited influence on central MSLP values during the most intense period of Sinlaku. Observations in the vicinity of the typhoon (ViObs) lead to the largest reduction of the central MSLP error. When the system begins to weaken after +60 h, larger improvements of the experiments are visible. These improvements, however, do not arise from a better intensity forecast in the short-range but rather from a better track forecast as for this case all experiments produce a track error reduction (see also Fig. 4.7c).

## 4.4 Discussion and conclusion

Data denial experiments were conducted with the ECMWF global model to assess the influence of targeted dropsonde observations on typhoon track forecasts during T-PARC. The observations were separated into three subsets to investigate the influence of observations from different locations relative to the TC.

Observations in the vicinity of the TC (ViObs) lead to the largest track error reduction. Observations of this subset were mainly collected by the Taiwanese Astra Jet operated under the DOTSTAR research programme. Previous studies with different models and different typhoon systems also showed a positive influence of these observations (Wu et al., 2005; Yamaguchi et al., 2009). One very important part of the flight strategy in the DOTSTAR programme is to circumnavigate the storm during every flight mission, besides often sampling parts of sensitive regions. The ViObs subset for all cases, except at 00 UTC 16 Sept, consists of observations that are located in a complete circle around the outer domain of the storm. Findings from Peng and Reynolds (2006) and Reynolds et al. (2009) that track forecasts of TCs are sensitive to changes in the initial conditions at an annulus around the storm center at approximately 500 km are consistent with the positive influence of the ViObs observations.

Even if a large fraction of the remote dropsondes (ReObs) is located in areas indicated to be of increased sensitivity by SV computations, results from this experiment do not show a large improvement of the track forecast. Observations in remote sensitive regions mainly influence the analysis fields close to the subtropical anticyclone or in the midlatitudes, whereas the structure of the TC itself is only marginally affected. Changes to the remote environment of the TC do not have a large influence on the track forecasts of Sinlaku and Jangmi. The low influence could be related to small analysis errors and a comparably good representation of the large scale flow around the TC in the ECMWF model due to the extensive use of satellite observations. Furthermore, the low resolution of the SV computations ( $T_L95$  at ECMWF during T-PARC) might not correctly reflect sensitivity patterns. There are indications that sensitivity maxima shift closer to the storm itself with an increased resolution of SV calculations (Lang et al., 2011). Finally, the sub-optimal sampling of the remote sensitive regions, with only parts of high and moderate sensitive regions covered, could also be a reason for the small influence of these dropsondes (Aberson, 2003).

The ECMWF data assimilation system seems to be capable of handling extreme observations in the TC centre (CeObs). The quality control works reliably and a large fraction of the data are flagged and rejected to minimise unrepresentative structures in the model. However, in terms of track forecast errors the influence is neutral on average.

There is a significant case to case variability with these observations and large positive (e.g. 00 UTC 09 Sept) as well as negative (e.g. 00 UTC 10 Sept) cases can be identified. Despite the information potentially provided by these data, future data assimilation systems have to solve several issues to fully exploit these observations. Unrealistic structures in the model analysis are sometimes introduced by the position offset of dropsondes. Up to now, dropsonde data are assimilated with one fixed position, but there can be a significant shift from the launch position during the descend in particular when they are placed in the eye wall region (Aberson, 2008). Additionally, incomplete sampling of the TC centre with dropsondes can introduce unrealistic asymmetries in the model resulting in wrong track forecasts. Track forecast degradations with dropsonde data from the centre region have been found with the NCEP GFS model and no dropsonde data within a radius of 111.1 km (or 3 times the specified radius of maximum wind, whichever is larger) are used in the data assimilation system of the GFS as a consequence (Aberson, 2008).

An average positive influence with AllObs is obtained, but not obligatory the most beneficial results are achieved when combining all available observations.

Large differences in the results of the experiments in the pre- and post-recurvature period of a recurving TC are detected. During the pre-recurvature period, a larger influence of the observations can be identified independent of the dropsonde subsets. Model errors in the structure change of the TC during landfall are expected, but improving the analysis of the typhoon and better forecasting the landfall point can minimise errors due to land interaction (Wu, 2001). The influence of dropsondes for typhoon targeting was limited after recurvature and the representation of the upstream midlatitude flow field becomes more important for the propagation of the TC. Reynolds et al. (2009) showed that in cases of recurving TCs, sensitivity can be found to the northwest of the TC and sometimes can be located as far as 4000 km upstream over the Asian continent. For these cases, a modification of the initial conditions next and in the environment of the TC through dropsondes can only have a limited influence on the track forecast. Results may be different for other observational data types as e.g. the Doppler wind lidar (Weissmann et al., 2005), which was operated on board the DLR Falcon during T-PARC. Weissmann and Cardinali (2007) and Weissmann et al. (2011) demonstrated the value of this new type of observations for ECMWF forecasts in the tropics and the midlatitudes.



## Chapter 5

# Adaptive DIAL humidity observations

### 5.1 Introduction

This chapter focuses on the assimilation of the high-resolution DIAL water vapour observations in the ECMWF model using the operational 4D-Var data assimilation system. The WALES demonstrator measured a unique sample of about 3900 DIAL water vapour profiles during 25 research flights in the period 26 August to 01 October 2008. The quality of the DIAL observations is assessed by comparison with independent dropsonde humidity observations and model output fields. The analysis and forecast influence of the additional DIAL observations is evaluated.

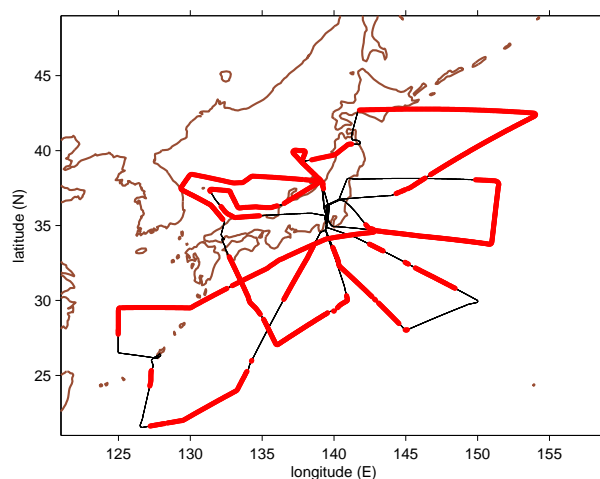


**Figure 5.1:** T-PARC flight tracks of the DLR Falcon (thin black line) used for the study. Thick red lines indicate the location of observed DIAL profiles.

Out of all flights during T-PARC, eight cases (Fig. 5.1) that show the highest observational coverage and are representative for different weather regimes, are selected for the study (Table 5.1). These cases include flights for typhoon targeting and the investigation of ET of the two major typhoons during T-PARC, Sinlaku and Jangmi. Additionally, flights for the purpose of observation targeting to improve midlatitude forecasts or the observation of tropical water vapour export are considered. From these eight flights, 47,700 DIAL observations are available which constitute 65% of DIAL observations from all 25 T-PARC flights.

case	date	objective	DIAL observations
1	00 UTC 02 Sept	midlatitude targeting	6861
2	00 UTC 09 Sept	tropical water vapour export	3787
3	12 UTC 11 Sept	targeting for Typhoon Sinlaku	7190
4	00 UTC 19 Sept	ET of Typhoon Sinlaku	8537
5	00 UTC 21 Sept	ET of Typhoon Sinlaku	7731
6	00 UTC 28 Sept	targeting for Typhoon Jangmi	3545
7	00 UTC 01 Oct	ET of Typhoon Jangmi (1)	4737
8	12 UTC 01 Oct	ET of Typhoon Jangmi (2)	5312

**Table 5.1:** Overview of selected cases and number of DIAL observations.

The assimilation setup is described in section 5.2. General results are presented in section 5.3 followed by a case study in section 5.4. Section 5.5 discusses and summarises the results.

## 5.2 Setup of assimilation experiments

The assimilation experiments are performed using the early 2010 operational version of the ECMWF system (cycle 36r1). In contrast to the operational setup, the experiments are conducted using a reduced horizontal resolution of  $T_L799$  ( $\sim 25$  km) and 91 vertical levels (L91).

### 5.2.1 Precipitable water content

The precipitable water content (PWC) in certain layers is used as input for the assimilation experiments since an observation operator  $H$  is already available (originally developed to assimilate data from the solar backscattering UV (SBUV) instrument). The DIAL system

measures the number density of water molecules  $N_w$  [ $\text{m}^{-3}$ ], which is converted to absolute humidity  $\rho_w$  [ $\text{kg m}^{-3}$ ]

$$\rho_w = N_w \cdot \frac{m_{H_2O}^*}{N_A} \quad (5.1)$$

with the molecular mass of water  $m_{H_2O}^* = 18.015 \text{ g mol}^{-1}$  and the Avogadro constant  $N_A = 6.022 \cdot 10^{23} \text{ mol}^{-1}$ . No estimation of other parameters is needed to derive the variable in contrast to e.g. specific humidity where additional temperature and pressure information is required (Behrendt et al., 2007a). Absolute humidity  $\rho_w$  is multiplied by the vertical resolution of the measurements to get vertically resolved profiles of PWC [ $\text{kg m}^{-2}$ ].

$$PWC(z) = \rho_w \cdot \Delta z \quad (5.2)$$

The sum of vertically resolved PWC over the whole atmosphere gives the total water column. PWC is a function of the altitude and depends on the vertical resolution  $\Delta z$  of the data. The DIAL data are averaged to a vertical resolution of  $\Delta z = 300 \text{ m}$  for the assimilation experiments. The vertical coordinate is converted from geometric height to pressure using temperature, pressure, and specific humidity from the operational ECMWF analysis.

### 5.2.2 Experiments

A control experiment (CNTL) is performed as reference run that uses all operational but no DIAL observations. Over the northern West Pacific basin, humidity information is mainly provided by microwave sounding instruments (AMSU-B, MHS, SSM/I, AMSR-E) and infrared sounders (GOES, HIRS, AIRS and IASI) (Andersson et al., 2007). Two experiments are conducted assimilating the DIAL observations together with the operational set of observations: ALL\_DIAL with the full resolution of DIAL observations, and AV\_DIAL, where five DIAL profiles are horizontally averaged. With the given horizontal resolution of the measurements of 5-7 km, averaging five profiles produces a spatial scale similar to the ECMWF model ( $\sim 25 \text{ km}$ ). In all experiments, dropsonde observations are not assimilated, first to avoid interaction between dropsonde and collocated DIAL humidity observations, and second to be used as independent validation of the DIAL observations. The experiments using DIAL observations are performed in an uncycled mode with the model background for each assimilation cycle being provided by CNTL, which restricts the influence of the DIAL observations to one particular assimilation time.

### 5.2.3 Error specification

The instrument error of the DIAL can be estimated to be  $< 5\text{-}7\%$  (Poberaj et al., 2002; Wirth et al., 2009). In ALL\_DIAL, the observation error standard deviation is set to 40% to account also for the representativeness error which was estimated from comparison with error statistics of radiosonde humidity observations. The observation error standard deviation is proportional to  $1/\sqrt{N_{obs}}$  assuming that the observation errors are independent, which reduces the observation error standard deviation to  $\sim 15\%$  at grid box length scale given the horizontal resolution of 5-7 km of the observations. Hence, the error standard deviation of 15% is assigned to the observations in AV\_DIAL, where the observations are averaged to the model resolution (see Table 5.2). The background error is set to be twice as large as the observation error for the BgQC to assure that a large percentage of DIAL observations enters the minimisation process and are not rejected prior to the assimilation.

Exp	observation		BgQC flag				VarQC weight (%) class			
	number	error	0	1	2	3	0-25	25-50	50-75	>75
ALL_DIAL	47700	40%	45967	488	<i>320</i>	<i>925</i>	<i>884</i>	803	9989	34779
AV_DIAL	9524	15%	8492	318	<i>160</i>	<i>554</i>	<i>1256</i>	653	2884	3917

**Table 5.2:** Number of DIAL observations marked during the different observation quality control steps. For the assimilation, only observations are considered that get a VarQC weight larger than 25%: ALL\_DIAL = 45571, AV\_DIAL = 7454. Italic fonts indicate that the observations are regarded as ‘false’.

## 5.3 Results

### 5.3.1 Comparison of DIAL and dropsonde observations

During all T-PARC Falcon flights, dropsondes of the type Vaisala RD-93 (Hock and Franklin, 1999) were deployed in regular intervals. The observations are compared with DIAL observations, whenever they are available within a circle of 5 km radius from the dropsonde launch position. The DIAL system measures the number of water molecules per volume  $N_w$  which is converted into absolute humidity  $\rho_w$  using Eq. 5.1. The dropsonde system measures pressure, temperature (T) and relative humidity (f), and the absolute humidity is computed using

$$\rho_w = \frac{e}{R_w \cdot T} = \frac{e_s(T) \cdot f}{R_w \cdot T}$$

with the gas constant for water vapour ( $R_w = 461 \text{ J K}^{-1} \text{ kg}^{-1}$ ) and applying the Clausius-Clapeyron equation (see e.g. Bohren and Albrecht, 1998) to calculate the saturation water vapour pressure  $e_s(T)$ . The dropsonde observations are quality controlled using different post-processing methods including automatic sounding quality-control software and visual examination of the data (Wang et al., 2010).

DIAL and dropsonde profiles are vertically averaged to the resolution of 25 m, which is slightly larger than the raw vertical resolution of dropsonde (5-10 m) and DIAL (15 m) observations, to create homogeneous height bins for the comparison of the two data sets. However, the presented results are not sensitive to the choice of the used height interval. Considering all the T-PARC flights of the DLR Falcon, 39,410 data points from 157 collocated profiles are used for the comparison. Figure 5.2a shows a linear relation (correlation coefficient 0.987) between DIAL and dropsonde absolute humidity observations. Larger deviations from the linear relation are found for low humidity values ( $< 0.5 \text{ g m}^{-3}$ ). The comparison of individual profiles shows a good agreement among the two observations as demonstrated in Figs. 5.2b,c.

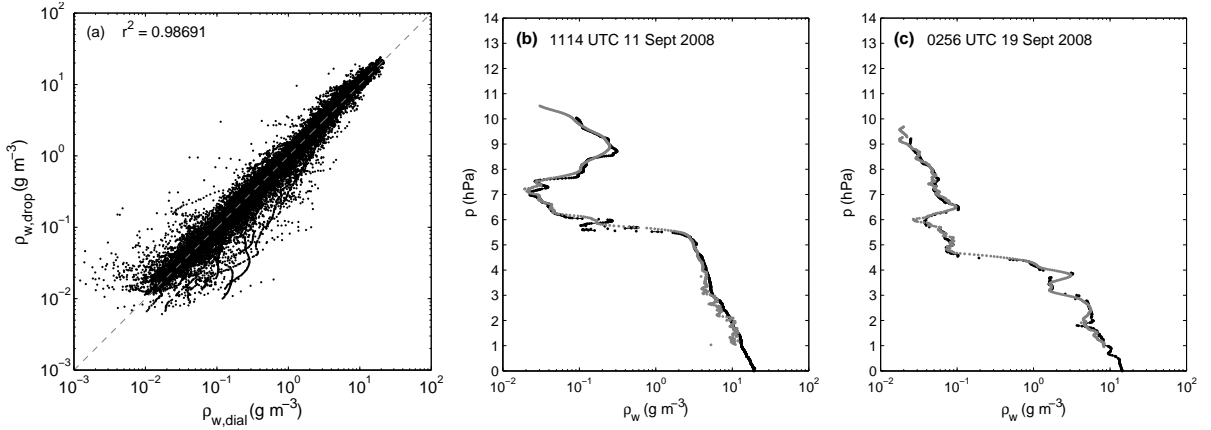


**Figure 5.2:** Comparison of DIAL and dropsonde observations of absolute humidity: (a) scatter plot of all 39,410 observations between 26 Aug and 01 Oct 2008, and (b), (c) two selected DIAL (grey) and dropsonde (black) profiles.

The absolute humidity difference is defined in absolute values as

$$d_{-\rho_w,abs} = \rho_{w,dial} - \rho_{w,drop} ,$$

and in relative values as

$$d_{-\rho_w,rel} = \frac{\rho_{w,dial} - \rho_{w,drop}}{0.5 \cdot (\rho_{w,dial} + \rho_{w,drop})} .$$

The relative difference takes into account the strong altitude dependence of moisture. The mean value (bias) of absolute and relative differences is calculated for all height intervals (Figs. 5.3a,b). Negative values indicate that the DIAL observations are drier than the dropsonde observations. In terms of bias of absolute differences (Fig. 5.3a), observations from both instruments are in agreement in the upper troposphere, whilst in the lower troposphere, the absolute bias is negative below 5 km (above mean sea level) and increases up to  $-1 \text{ g m}^{-3}$  at the ground. The relative bias reaches values between  $-5\%$  and  $-10\%$  below 2 km. In contrast to the absolute bias, the relative bias (mean relative difference) is close to zero between 2-5 km (Fig. 5.3b). In addition, a median and the lower and upper quartiles of the relative differences are shown in Fig. 5.3b. The smaller relative bias (than absolute bias) is presumably due to outliers as the values in several layers are close to the upper quartile of relative differences between 2-7 km. The 1000 m running average of the relative median also shows negative values between 2-5 km which is in better agreement with the absolute bias.

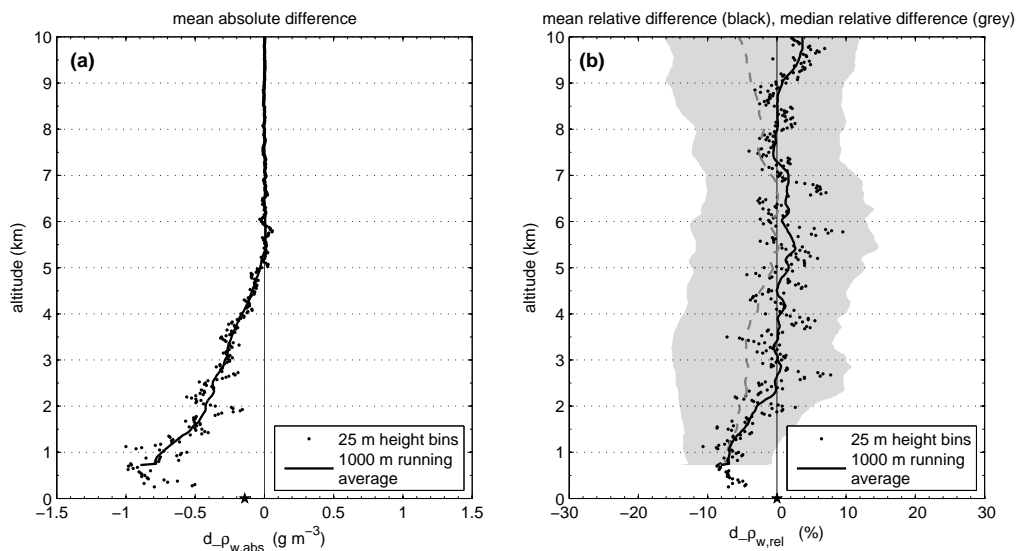


**Figure 5.3:** Vertical distribution of (a) the mean absolute and (b) the mean relative differences between DIAL and dropsonde observations of absolute humidity for the same data set as in Fig 5.2a. The solid black line represents a 1000 m running average and the asterisk mark the overall bias of all observations. In (b) the dashed grey line in displays the 1000 m running average of the median of the relative differences and the grey shading the lower and upper quartiles of the relative differences.

A mismatch between the location of dropsonde and DIAL observations might produce a larger standard deviation of the differences between the two observations (Sun et al., 2010), but should not result in an increased bias. The identified systematic differences between dropsonde and DIAL observations in the lower part of the troposphere seem to

be mainly caused by the DIAL observations since dropsonde observations were shown to be largely unbiased (Wang, 2005). However, a dropsonde bias in the range of several percent can not be excluded. Larger errors of DIAL observations can occur in the tropical boundary layer and the lower part of the troposphere (Poberaj et al., 2002). Due to the high water vapour content in the tropics, a very weak water vapour absorption line located at 935.449 nm wavelength (see Fig. 1 in Wirth et al., 2009) had to be selected to probe the lowest part of the atmosphere. The total absorption at this wavelength is affected by the pressure broadened wings of nearby strong absorption lines. Both pressure broadening by air molecules and self broadening by water vapour are taken into account during processing, but the accuracy of the absorption cross sections calculated from the line parameters given by the HITRAN 2006 spectroscopic database at these extremely high humidity values is not sufficiently known and may reach values in the range of the observed bias. The bias of all data is in absolute terms  $-0.142 \text{ g m}^{-3}$  with a standard deviation of  $\pm 0.636 \text{ g m}^{-3}$  and in relative terms 0.0% with a standard deviation of  $\pm 30.7\%$ .

### 5.3.2 Assimilation statistics of the DIAL experiments

The numbers of observations identified by the different screening steps of the assimilation system are summarised in Table 5.2. In ALL\_DIAL more than 97% of the observations pass the BgQC and enter the assimilation procedure being classified as correct or probably correct observation (flags 0 and 1) while in AV\_DIAL the rejection rate is slightly higher and 92.5% pass the BgQC. These numbers seem reasonable taking into account the smaller observation error variances assigned in AV\_DIAL. Similarly, 98% of the observations in ALL\_DIAL are considered as ‘correct’ in the VarQC (weight larger than 25%) compared to 85% of the observations in AV\_DIAL. The quality control is more active for AV\_DIAL compared to ALL\_DIAL. The observation error standard deviation of 15% in AV\_DIAL, that is based on the assumption of independent observation errors, may be too small. This is also indicated by the diagnosed observations error standard deviations of 28% for ALL\_DIAL and 21% for AV\_DIAL calculated a posteriori from the assimilation statistics following Desroziers et al. (2005). The instrumental error of the DIAL system is horizontally uncorrelated but the representativeness error seems to be correlated at the horizontal resolution of 5-7 km of the DIAL observations.

The background and analysis departures are the difference in observation space between observation and model background and observation and analysis, respectively:

$$\mathbf{d}_{bg} = \mathbf{y} - H [\mathbf{x}^b],$$

$$\mathbf{d}_{an} = \mathbf{y} - H [\mathbf{x}^a].$$

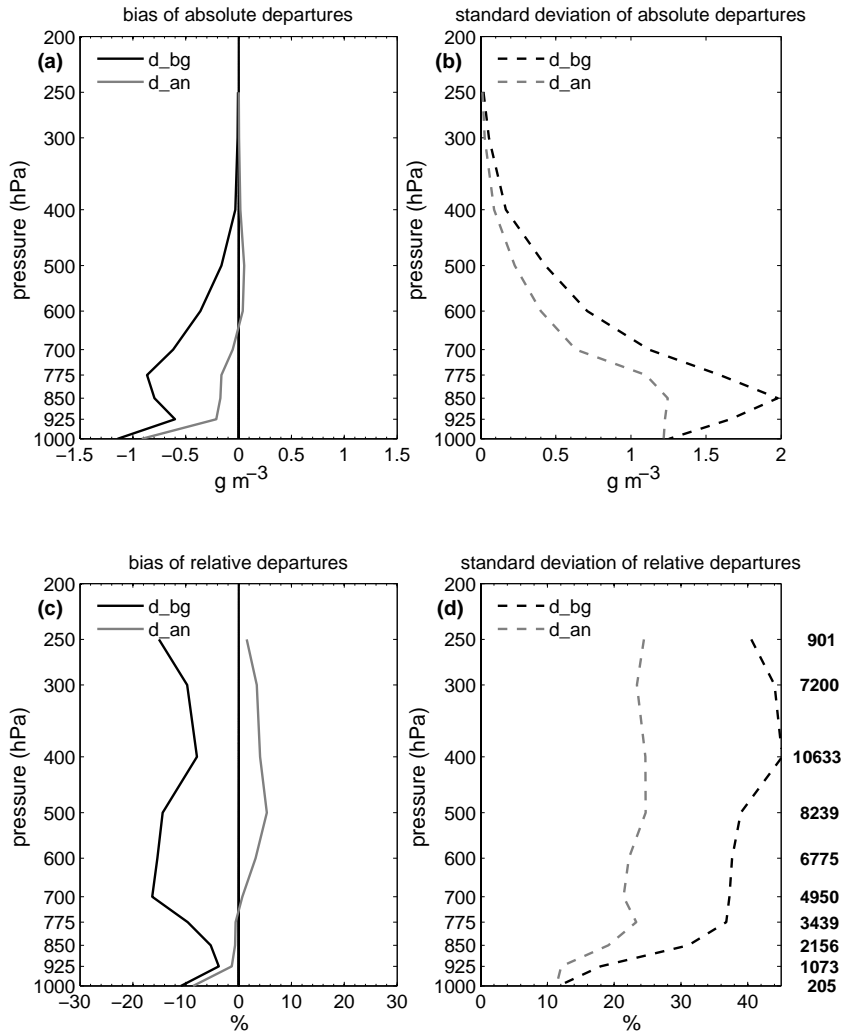


**Figure 5.4:** Vertical distribution of background departures  $d_{bg}$  (black) and analysis departures  $d_{an}$  (grey) for DIAL observations in ALL\_DIAL: (a) absolute bias, (b) absolute standard deviation, (c) relative bias and (d) relative standard deviation. Only data are considered that passed the BgQC and get a weight of at least 25% in the VarQC. The number of DIAL observations considered for each pressure interval are displayed to the right.

The bias and the standard deviation for the background and analysis departures of absolute humidity for ALL\_DIAL is shown in Fig. 5.4. Absolute humidity is derived from PWC dividing by the vertical resolution  $\Delta z = 300$  m (Eq. 5.2). A negative bias of background departures is seen in the lower troposphere with maximum values close to  $-1 \text{ g m}^{-3}$  (Fig. 5.4a). The bias of the analysis departures is much smaller and close to zero except in the boundary layer region. The standard deviation of analysis departures is also reduced compared to the background value, which indicates that the assimilation is using infor-

mation from DIAL observations and the observations actively contribute to the analysis (Fig. 5.4b). To include the decrease of water vapour with height, relative background and analysis departures are defined as the absolute departure value divided by the mean value of observation and model field. A much more homogeneous distribution in the vertical is identified for the bias of these relative departures (Fig. 5.4c). The bias of the relative background departures varies between -5% and -15% over the whole troposphere, while the bias of the relative analysis departures is less than 5% with negative values below 775 hPa and positive ones above (Fig. 5.4c). The standard deviation of the relative departures reaches a maximum in the upper troposphere (Fig. 5.4d) different to the absolute standard deviation which peaks around 850 hPa. The sample available reduces rapidly at lower levels. The results for AV\_DIAL are overall similar, but with smaller biases and standard deviations (not shown).

Table 5.3 summarises the bias and standard deviation (stddev) for both experiments. The negative bias between the observations and the model background indicates that the model is systematically moister than the DIAL observations. The moisture in the model fields is reduced when the DIAL observations are assimilated as shown by the analysis departures.

Exp	abs bias $\pm$ stddev ( $\text{g m}^{-3}$ )		rel bias $\pm$ stddev (%)	
	d_bg	d_an	d_bg	d_an
ALL_DIAL	$-0.281 \pm 0.888$	$-0.015 \pm 0.543$	$-11.4 \pm 40.2$	$2.9 \pm 23.2$
AV_DIAL	$-0.242 \pm 0.773$	$-0.036 \pm 0.423$	$-7.1 \pm 30.0$	$0.7 \pm 13.4$

**Table 5.3:** Bias and standard deviation (stddev) of DIAL absolute humidity observation departures.

### 5.3.3 Analysis impact

#### Analysis verification with dropsondes

The DIAL analysis impact is verified using independent dropsonde humidity observations, which are monitored passively, i.e. do not influence the analysis. These observations are the best available source of humidity information since other observing systems as for example satellite humidity observations have poor effective vertical resolution in the troposphere. Model analyses of CNTL, ALL\_DIAL and AV\_DIAL are compared to dropsonde observations in terms of root mean square (RMS) differences. A smaller RMS difference of ALL\_DIAL and AV\_DIAL indicates a more accurate analysis. Regarding the absolute

humidity analysis, RMS differences are, on average, smaller in ALL\_DIAL ( $1.11 \text{ g m}^{-3}$ ) and AV\_DIAL ( $1.14 \text{ g m}^{-3}$ ) than in CNTL ( $1.20 \text{ g m}^{-3}$ ), which is equivalent to an accuracy increase with respect to CNTL of 7.5% and 5%, respectively (Fig. 5.5a). In two cases, the DIAL experiments show slightly larger RMS differences compared to CNTL, whereas in four cases smaller values are seen. For wind and temperature variables, RMS differences for the DIAL experiments are also reduced compared to CNTL in the order of 2-3% (not shown).

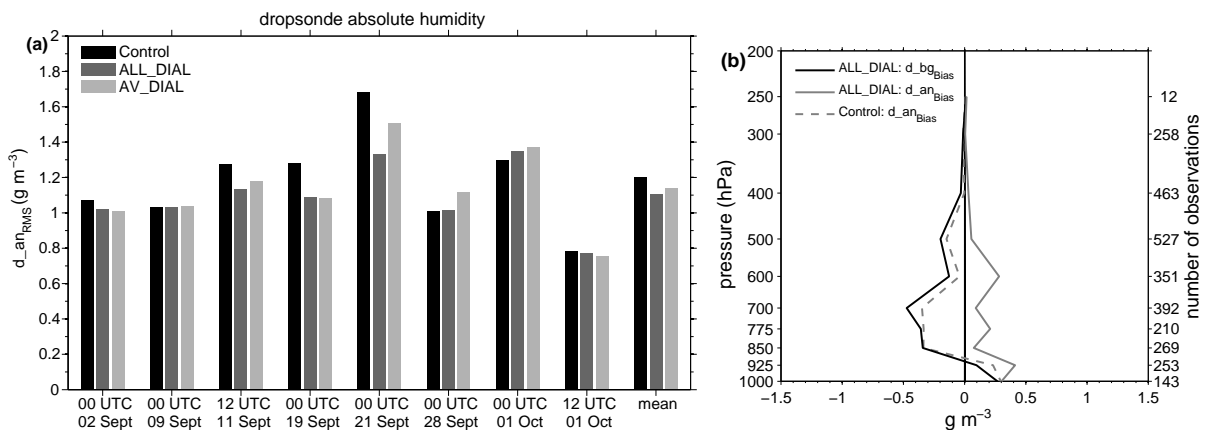


**Figure 5.5:** (a) Root mean square (RMS) differences of absolute humidity of dropsonde observations and model analyses of CNTL, ALL\_DIAL and AV\_DIAL in  $\text{g m}^{-3}$ . (b) Vertical distribution of absolute bias of background departures (d.bg) and analysis departures (d.an) for dropsonde absolute humidity compared to ALL\_DIAL and CNTL. Note that the background departures are the same for ALL\_DIAL and CNTL. The number of dropsonde observations considered for each pressure interval are displayed to the right.

Background and analysis departures of dropsonde observations are also used to analyse systematic errors. The bias of absolute humidity dropsonde observation departures for ALL\_DIAL and CNTL is shown in Fig. 5.5b. The bias of dropsonde background departures is negative for all levels above 850 hPa, similar to the background departures of DIAL observations (compare with Fig. 5.4a). This suggests that the model background is systematically too moist since dropsonde and DIAL observations match in the upper and middle troposphere (compare Fig. 5.3b). In the lower troposphere, the bias of dropsonde background departures is smaller and becomes positive in the boundary layer (Fig. 5.5b). The different behaviour of dropsonde and DIAL background departures at low levels agrees with the systematic difference between the two observations at those levels (Fig. 5.3). Using the bias of the background departures of dropsonde ( $-0.158 \text{ g m}^{-3}$ ; Fig. 5.5b) and DIAL ( $-0.281 \text{ g m}^{-3}$ ; Table 5.3) observations, a bias of the difference between DIAL and dropsonde observations can be calculated ( $-0.123 \text{ g m}^{-3}$ ). This value is similar to the

one computed for all available DIAL and dropsonde observations ( $-0.142 \text{ g m}^{-3}$ ), despite the different vertical resolution and different sample, which implies that the bias between dropsonde and DIAL observations is not sensitive to the vertical resolution and the used sample. The fact that the bias of dropsonde analysis departures is positive in ALL\_DIAL compared to a negative bias in CNTL, illustrates the drying effect of DIAL observations (Fig. 5.5b).

### Analysis influence

The analysis departures of satellite and radiosonde humidity observations are not affected considerably by the assimilation of DIAL humidity observations. Additionally, the Degree of Freedom for Signal (DFS) is calculated for the DIAL experiments, which estimates the information content provided by the observations during the assimilation (Cardinali et al., 2004). The DFS depends on the observations' influence as well as on the number of observations. Table 5.4 lists the estimated DFS and mean observation influence from all satellite, radiosonde and DIAL humidity observations. DIAL observations have the largest influence among all other remote sensing and radiosonde humidity observations, which confirms the strong influence of the adaptive DIAL observations in the humidity analysis with respect to the other humidity observations.

	DIAL	HIRS	MTSAT	AMSU-B	MHS	AMSR-E	SSM/I	MERIS	TEMP
mean OI	0.71	0.07	0.16	0.04	0.13	0.01	0.002	0.16	0.16
observation number	46455	89766	29192	90675	16617	85494	74307	640	9775
DFS	32957.0	5935.8	4803.2	3848.5	2114.2	544.0	211.1	102.7	1527.9
DFS in % of total	63.3	11.4	9.2	7.4	4.1	1.0	0.4	0.2	2.9

**Table 5.4:** Mean observations influence (OI) and Degree of Freedom for Signal (DFS) for DIAL, satellite and TEMP humidity observations in ALL\_DIAL over the western North Pacific basin ( $15^\circ\text{N}$ - $55^\circ\text{N}$ ,  $110^\circ\text{E}$ - $160^\circ\text{E}$ ).

Additionally, the influence of the DIAL observations on the analysis is shown based on analysis increments of total column water vapour (TCWV). TCWV is an integrative measure of the water vapour in the atmosphere and is strongly determined by the lowest part of the troposphere, that contains most of the water vapour. Figure 5.6 shows the mean TCWV increments averaged over all cases for CNTL and the difference of the mean increments between ALL\_DIAL and CNTL at the beginning of the assimilation window (either 09 UTC or 21 UTC). The increments of CNTL exhibit positive and negative areas, which indicates that the assimilation system is not systematically adding or removing water vapour. The difference of the increments between ALL\_DIAL and CNTL shows broad regions with negative values leading to more negative TCWV increments when using

the DIAL observations. The drying effect of the DIAL observations is in agreement with the previous diagnostic assessment that shows that DIAL observations, on average, are drier than the model background and close to the model analysis after assimilation. Mean analysis increments for wind and temperature (not shown) are noisy and not systematic. The analysis increments of AV\_DIAL (not shown) are similar to ALL\_DIAL.

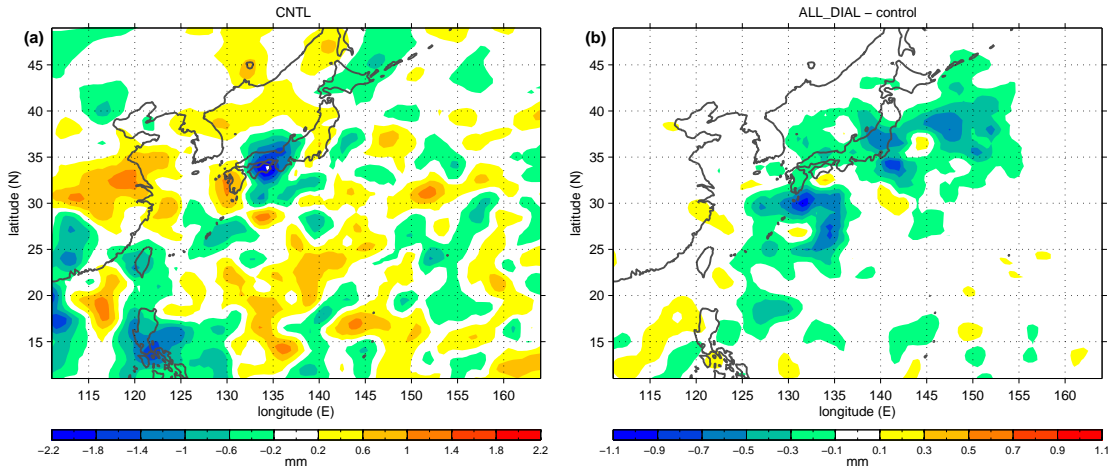


**Figure 5.6:** Mean analysis increments of TCWV for the selected eight cases of (a) CNTL and (b) the difference between the mean increments of ALL\_DIAL and CNTL in mm.

### 5.3.4 Forecast impact

The forecast impact of the DIAL observations is addressed in terms of TE. TE is an integrated measure of the forecast error and includes information about wind ( $u,v$ ), temperature ( $T$ ) and specific humidity ( $q$ ) (see also section 2.4). The analysis fields of CNTL are used as verification for all calculations. The improvement or reduction of the TE error is defined as the difference of the TE error of the DIAL experiments against CNTL, with negative values indicating improvement by assimilating DIAL observations

Figure 5.7 displays the TE error reduction of AV\_DIAL with respect to CNTL averaged over a geographical domain covering the western North Pacific basin ( $15^{\circ}\text{N}$ - $60^{\circ}\text{N}$ ,  $115^{\circ}\text{E}$ - $160^{\circ}\text{W}$ ) for all eight cases. In six cases, the values are small and range from  $-1.5 \text{ m}^2 \text{ s}^{-2}$  to  $+1.5 \text{ m}^2 \text{ s}^{-2}$ , but improvements up to  $-4 \text{ m}^2 \text{ s}^{-2}$  are identified for the forecasts initialised on 19 Sept and 21 Sept. The relative differences of AV\_DIAL and CNTL are generally in the range of  $\pm 2\%$ , except for the +48 and +60 h lead time of forecasts initialised on 19 Sept and 21 Sept which show improvements up to  $-6\%$ . Results for ALL\_DIAL (not shown) are similar to AV\_DIAL, but with slightly smaller improvements.

Three research flights were conducted during the lifetime of Typhoon Sinlaku (Table 5.1:

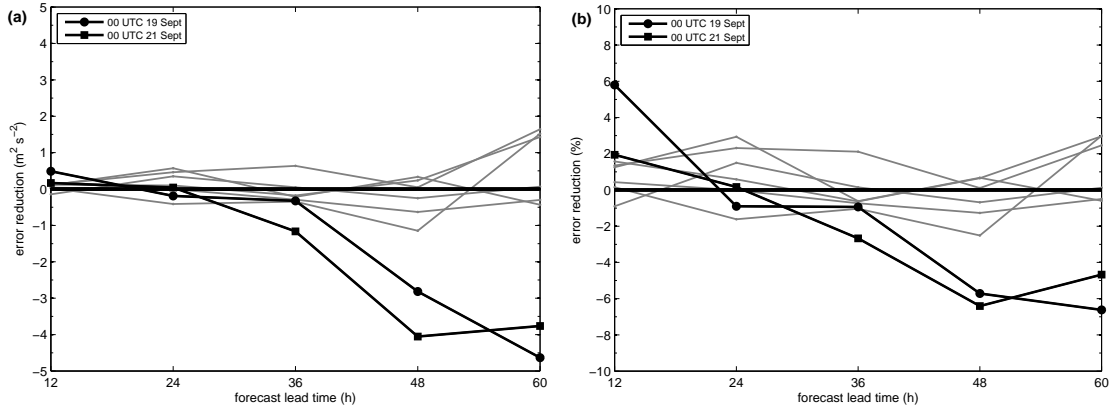


**Figure 5.7:** (a) Absolute and (b) relative reduction of TE forecast errors for AV\_DIAL compared to CNTL over the western North Pacific basin ( $15^{\circ}\text{N}$ - $60^{\circ}\text{N}$ ,  $115^{\circ}\text{E}$ - $160^{\circ}\text{W}$ ). Grey lines represent the six cases with small forecast impact. The forecasts are verified with the CNTL analysis. Negative values indicate reduced errors in AV\_DIAL.

case 2,3,4) and one during Typhoon Jangmi (Table 5.1: case 6). For these cases, typhoon track forecasts of the DIAL experiments are verified against the JMA best track data. The influence of the DIAL observations is small and the mean track forecast errors of ALL\_DIAL and AV\_DIAL are similar to the ones of CNTL (Fig. 5.8). The reason for this low influence may be that, due to the signal absorption in clouds, the nadir-pointing DIAL cannot provide information on water vapour in the convectively active environment of the storm that would likely be more influential on the dynamical evolution of the system.

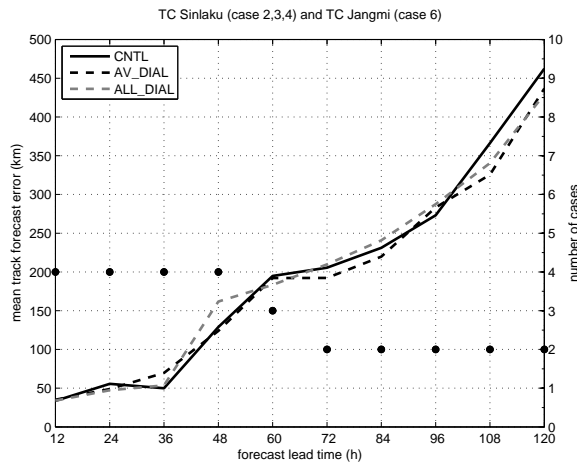


**Figure 5.8:** Mean track forecast errors (km) for ALL\_DIAL, AV\_DIAL and CNTL. Black dots represent the number of cases evaluated at each forecast lead time. Typhoon track forecasts are evaluated for three cases of Typhoon Sinlaku and for one case of Typhoon Jangmi.

## 5.4 Case study: 19 September 2008

Out of the eight cases, 19 Sept 2008 is selected for a detailed case study due to the large influence of DIAL observations compared to the other cases. The objectives of the flight were to examine the ridge building that was triggered by the outflow of Typhoon Sinlaku and the interaction of the storm with the midlatitude jet (Fig. 5.9a). At analysis time, Typhoon Sinlaku is located at about  $134^{\circ}\text{E}$ ,  $32.5^{\circ}\text{N}$  close to the south coast of the main island of Japan. The flight track starts at the jet entrance region next to the northern tip of Japan (Fig. 5.9a, labels 1,2), continues eastwards along the jet streak (label 3) and cuts through the jet maximum on the way back (label 4). The flight track is also partially located in sensitive regions highlighted by ECMWF SV-based calculations (not shown). The TCWV field shows a sharp north-south gradient to the east of Japan which is partially crossed on the last flight leg (Fig. 5.9a). A tongue of moist air ( $28 \text{ mm} \leq \text{TCWV} \leq 34 \text{ mm}$ ) extends further to the north and is located downstream of an approaching trough to the north.

The height-distance transect of DIAL observations is shown in Fig. 5.9b. In the first third of the flight (labels 1,2), PWC values greater than  $1.5 \text{ kg m}^{-2}$  are observed in the lower troposphere up to 775 hPa. Further to the east, the layer of large PWC values increases its vertical extension and the upper boundary reaches 600 hPa next to the easternmost point of the flight track (label 3). This moist layer shows vertical as well as horizontal fluctuations. The vertical extent of the moist layer is reduced to 700 hPa on the flight leg back to Japan. During the end of the flight track (label 4), the aircraft enters a region with strong convective activity and a pronounced vertical transport of moisture from the ground up to 350 hPa is identified. The observational gaps (white regions in the transects) are caused by the full absorption of the lidar signal in clouds. Figure 5.9c shows the same transect as Fig. 5.9b, but analysis increments of PWC for AV\_DIAL. Negative analysis increments occur in the moist layer close to the ground for most of the transect, which indicates a drying effect of the DIAL observations on the analysis in this region. However, at the jet entrance region (label 2) the DIAL observations lead to an increase of moisture at 700 hPa in a region with a less pronounced vertical moisture gradient. The vertical transport of moisture at the end of the flight track (label 4) is influenced by DIAL observations and an increase of moisture is seen in the layer between 775 hPa and 550 hPa followed by a decrease above 500 hPa.

Analysis differences of absolute humidity at 850 hPa between AV\_DIAL and CNTL (Fig 5.10a) are related to the area of moist air extending to the north and to the gradient of moisture east of Japan, where AV\_DIAL is drier than CNTL as expected from the analysis increments (compare Fig. 5.9c). In the region east of Typhoon Sinlaku, AV\_DIAL

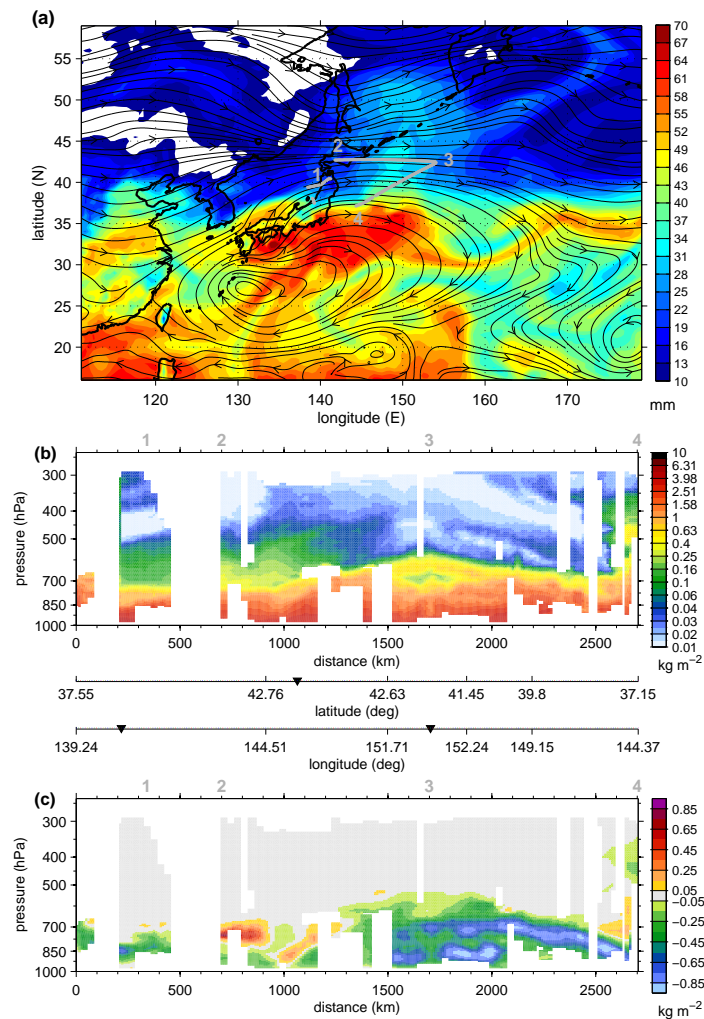


**Figure 5.9:** (a) Streamlines at 200 hPa and TCWV for the CNTL analysis at 00 UTC 19 Sept. The direction of the flight track (grey line) is clockwise. Height-distance transect of (b) the DIAL PWC observations and (c) PWC analysis increments of AV\_DIAL for the 00 UTC 19 Sept assimilation time sampled between 2257 UTC 18 Sept and 0436 UTC 19 Sept. Bold grey numbers label different sections of the flight track.

also shows areas with higher moisture content at low levels. At +12 h forecast lead time, the differences between AV\_DIAL and CNTL are transported downstream to the east and stretch from Sinlaku to another low pressure system over the central North Pacific (Fig. 5.10b). In addition, a broad region of negative forecast differences is seen downstream of the trough centred over the Sea of Okhotsk and the Kamchatka Peninsula, where the AV\_DIAL forecast generally is drier than the CNTL forecast. This humidity difference affects the geopotential height and wind fields at 500 hPa next to the intensifying trough and a less intense system is forecast in AV\_DIAL at +24 h (Fig. 5.11a). From +24 h on-

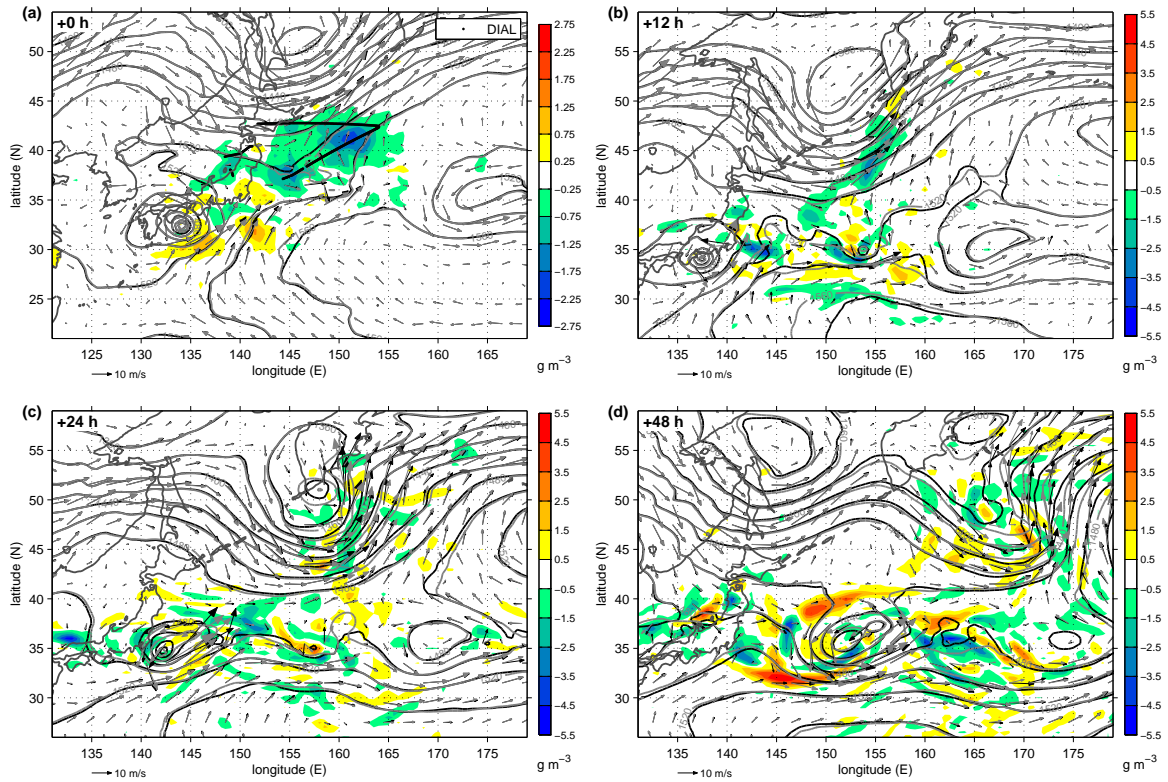


**Figure 5.10:** Absolute humidity difference ( $\text{g m}^{-3}$ ) at 850 hPa between AV\_DIAL and CNTL (a) for the analysis at 00 UTC 19 Sept, and for (b) +12 h, (c) +24 h and (d) +48 h forecasts initialised at 00 UTC 19 Sept. Lines (arrows) represent the geopotential height (wind field) at 850 hPa: AV\_DIAL is shown in black and CNTL in grey. Note the different color scaling in (a).

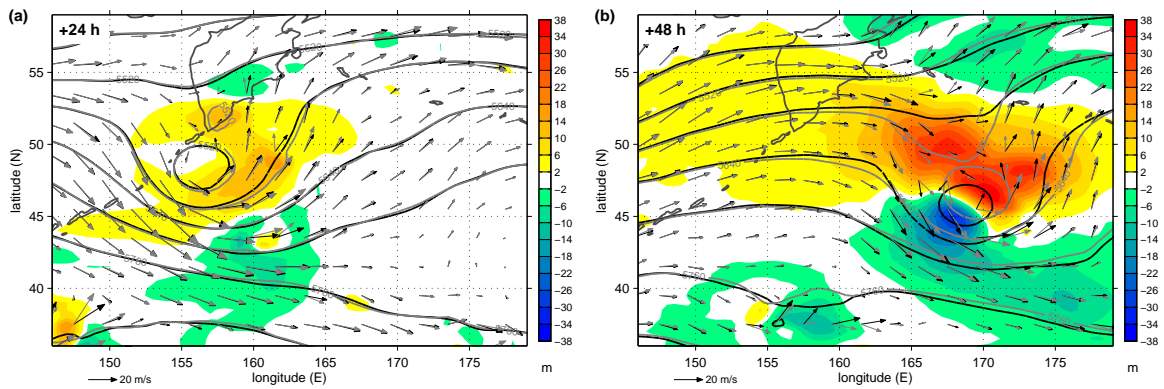


**Figure 5.11:** Forecast difference of geopotential height (m) at 500 hPa between AV\_DIAL and CNTL for (a) +24 h and (b) +48 h forecasts initialised at 00 UTC 19 Sept. Lines (arrows) represent the geopotential height (wind field) at 500 hPa: AV\_DIAL is shown in black and CNTL in grey.

wards, humidity differences do not grow much in amplitude, but change their structure and become inhomogeneous with alternating positive and negative areas (Fig. 5.10c). Higher values of moisture in AV\_DIAL are located west of ex-Sinlaku at +48 h (Fig. 5.10d) and forecast differences also spread to the east and polewards. The development of the poleward trough is modified and a less pronounced system that is shifted further to the south is seen in the AV\_DIAL forecast (Fig. 5.11b).

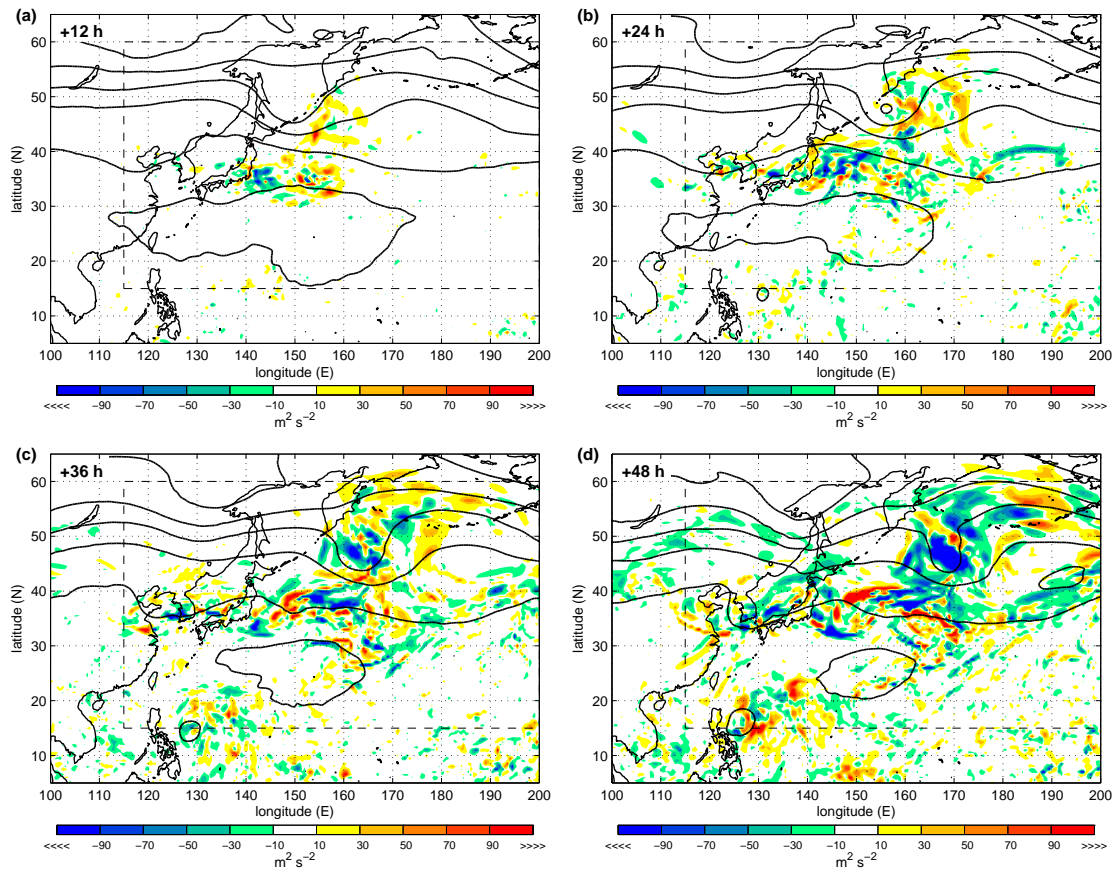


**Figure 5.12:** Geographical maps of TE forecast error reduction ( $\text{m}^2 \text{s}^{-2}$ ) for the AV\_DIAL experiment compared to the control run for (a) +12 h, (b) +24 h, (c) +36 h and (d) +48 h forecasts initialised at 00 UTC 19 Sept. The forecasts are verified with the CNTL analysis. The analysis of 500 hPa geopotential height of the CNTL experiment is shown as solid line and the geographical domain used for the averaging of the TE improvement as dashed line.

The TE error of the AV\_DIAL forecast is reduced compared to CNTL forecast from +24 h to +60 h (Fig. 5.7). The signal in the TE error is related to the region where the largest humidity and geopotential differences are found (Fig. 5.12), but also noise starts to appear further to the south that is not directly linked to the observation influence. Differences of TE error close to ex-Sinlaku and the trough to the north grow strongest

and at +48 h a clear TE error reduction of the AV\_DIAL forecast is seen related to the poleward trough. The changes of the humidity, geopotential and wind field of the trough, caused by the initial changes in the moisture distribution of AV\_DIAL (Fig. 5.10a), are reducing the TE error of the AV\_DIAL forecast considerably (Fig. 5.12d). Note that the evolution on 21 Sept 2008 (Fig. 5.12), the second case with a clear positive forecast impact, is similar but the modification of the humidity analysis connected with the remnants of Sinlaku is more important for the forecast improvements.

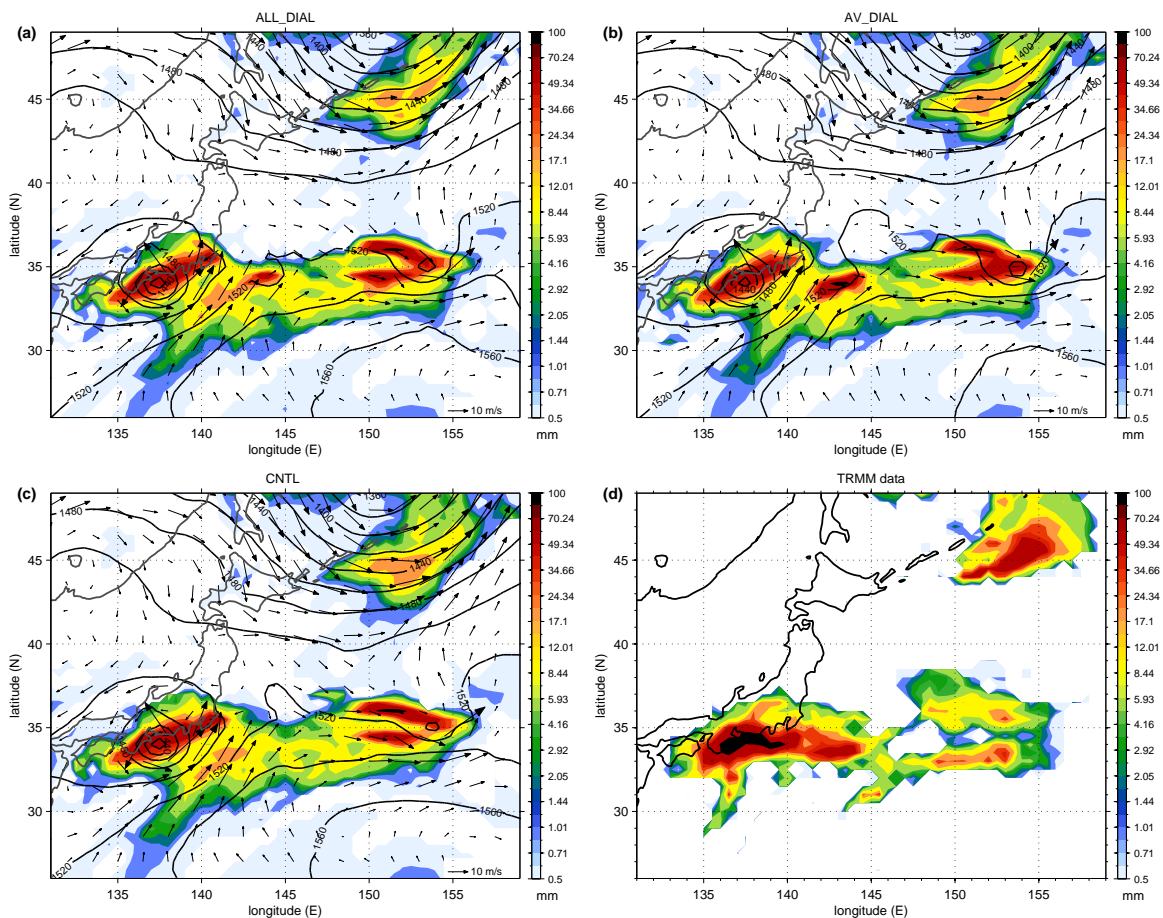


**Figure 5.13:** +12 h forecast of 12-hourly rainfall (colour shading), geopotential height (black line) and wind field (black arrows) at 850 hPa initialised at 00 UTC 19 Sept for (a) ALL\_DIAL, (b) AV\_DIAL and (c) CNTL. (d) The 12-hourly rainfall derived from the Tropical Rainfall Measuring Mission (TRMM) data (3B42 V6)<sup>1</sup>.

Changes in the moisture analysis also affect the precipitation forecast. The accumulated 12-hourly rainfall forecast from ALL\_DIAL, AV\_DIAL and CNTL as well as the rainfall product derived from Tropical Rainfall Measurement Mission (TRMM) data (3B42 V6) are displayed in Fig. 5.13. The rainfall forecast of the experiments generally looks reasonable

and agrees with the TRMM observations. Larger differences occur at the eastern side of Typhoon Sinlaku around 34°N, 142.5°E, where the precipitation forecast of AV\_DIAL seems to fit the TRMM based data best while no distinct differences between forecasts are found in other regions.

## 5.5 Discussion and conclusion

A large data set of about 40,000 high-resolution humidity observations measured by a four-wavelength DIAL system installed on-board of the DLR Falcon aircraft is assimilated into the ECMWF global model using a version of the operational 4D-Var assimilation system.

A detailed comparison of the DIAL observations to dropsonde humidity observations is performed. Single profiles of both observing systems show good agreement. Moist layers and sharp gradient are represented correctly. In the statistical comparison, a bias between DIAL and dropsonde observations is found, especially in the lower troposphere, where DIAL observations are drier than the dropsondes. The overall bias of absolute humidity is  $-0.142 \text{ g m}^{-3}$ . While the overall relative bias is less than  $-0.01\%$ , a relative dry bias of  $\sim -4.2\%$  is seen from the ground up to 3 km. This value is comparable to results from an intercomparison study during COPS, when a dry bias of the DLR DIAL system of  $-2.23\%$  was found compared to other water vapour lidar observations (Bhawar et al., 2011). Larger errors of the DIAL system close to the ground may result from the selected weak water vapour absorption line leading to reduced accuracy.

The assimilation of DIAL observations enables the comparison of model output fields and observations against each other. Background and analysis departures are directly calculated in the assimilation system, which minimises interpolation errors as no additional interpolation steps are needed as in previous studies of Flentje et al. (2007) and Schäfler et al. (2011a). Using all DIAL observations from eight selected cases, a bias between the model background (i.e. short-range model forecast) and the observations of  $-0.281 \text{ g m}^{-3}$  ( $-11.4\%$ ) is found with the model background being moister than the observations. The relative bias against the model background is consistent at all heights and confirms the findings of Flentje et al. (2007) and Schäfler et al. (2011a), who discovered a bias in the range of 0-11% and 17.1%, respectively. These studies considered single flights located in different regions of the globe while this study uses a larger data set within the same geographical region. Dropsondes also show a negative bias against the model background in the middle and upper troposphere, similar to the DIAL observations. This suggests a

---

<sup>1</sup>The TRMM data were acquired using the GES-DISC Interactive Online Visualization ANd aNalysis Infrastructure (Giovanni) as part of the NASA's Goddard Earth Sciences (GES) Data and Information Services Center (DISC).

moist model bias in these layers. In the lower troposphere, dropsondes indicate a dry bias of DIAL observations.

DIAL observations can only be made in cloud free regions as lidar systems operate in the visible and near infrared spectra and can not penetrate optically thick clouds or rain. This inhomogeneous distribution of water vapour observations may also contribute to the identified bias of the DIAL observations. It was highlighted before that the ECMWF model in rainy or nonrainy areas can have opposite humidity biases of 5-10% of TCWV (Marécal et al., 2001, 2002). When satellite humidity data were only used in rain-free conditions, extrapolation of information into rainy areas often degraded the analysis by increasing the bias (Andersson et al., 2005).

The DFS of DIAL is the largest compared to that of radiosonde and satellite humidity observations. On average, DIAL observations reduce the moisture content of the analysis. The accuracy of the analysis of ALL\_DIAL, AV\_DIAL and CNTL is evaluated by using independent dropsonde humidity observations. On average, the RMS differences between these dropsonde observations and ALL\_DIAL and AV\_DIAL analyses are reduced by 7.5% and 5%, respectively, compared to CNTL.

In general, a smaller forecast influence of humidity observations compared to pressure, wind or temperature is expected whenever diabatic processes do not affect the model dynamics explicitly and are not important for the forecast. In the experiments performed, DIAL observations only lead to a clear positive forecast impact in two out of eight cases, whereas the influence in the other six cases is less than  $\pm 2\%$ . The observing system experiments in Bengtsson and Hodges (2005) and Andersson et al. (2007) denied either a subset of humidity observations or all humidity observations completely. In contrast, the experiments in this study use the operational observational network with a few million observations each day plus a limited set of additional DIAL observations ( $\sim 3500$  to 8500 per day). Even when using all additional T-PARC dropsonde observations (wind, temperature and humidity), a limited impact on midlatitude forecasts in the ECMWF was found, in particular with the uncycled setup (Weissmann et al., 2011). A cycled experiment, that assimilates all DIAL observations, was also performed within this study. However, no results of the cycled experiment are shown since the assimilation statistics of DIAL and other humidity observations are not modified considerably, the forecast influence is comparable to the uncycled ALL\_DIAL experiment and the influence of the DIAL observations is easier to track in the uncycled case.

In some cases, changes to the moisture fields can affect the dynamics considerably as seen on 19 Sept 2008. DIAL observations modify the humidity analysis at an apparently sensitive region of a distinct north-south humidity gradient and next to a tongue of moist air extending polewards to a developing midlatitude low-pressure system. These changes

of the humidity influence the forecast and lead to a reduction of the TE forecast error up to -6% from +24 h onwards.

The TC track forecast is not affected significantly by the DIAL observations in contrast to previous studies with LASE data (Kamineni et al., 2006; Biswas and Krishnamurti, 2008). The smaller influence on TC track forecasts is likely related to the fact that the LASE data studies apply a different assimilation procedure and use the Florida State University global spectral model, whereas this study uses the operational ECMWF model system with millions of satellite data assimilated. The influence of additional observations on TC forecasts strongly depends on the assimilation and forecasting system which is also documented in other studies (e.g. Chou et al., 2010; Weissmann et al., 2011).

DIAL observations are taken in cloud free regions, whilst convectively active and baroclinically unstable regions, where the moisture distribution plays an important role due to diabatic processes, are often covered by clouds. A high correlation between the location of clouds and meteorologically sensitive areas calculated using adjoint techniques was found by McNally (2002), which highlights the importance of observations in cloudy and rainy regions.

DIAL observations are assimilated with the full horizontal resolution (ALL\_DIAL) but also averaged to grid box scale (AV\_DIAL). Results from both experiments are similar, but the averaging setup seems to be more suitable as the bias is reduced and the forecast improvement is larger. Currently, the ECMWF 4D-Var analysis is computed at the resolution of  $T_L255$  ( $\sim 80$  km) which limits the influence of observations with finer resolution. Nevertheless, spatial high-resolution DIAL observations are potentially valuable for mesoscale models which have a horizontal model resolution similar to that of the observations and can resolve diabatic processes such as convection explicitly. For future assimilation experiments, the introduction of a bias correction of DIAL data may help to optimise the influence of the DIAL humidity observations since variational assimilation methods assume unbiased observations.



## Chapter 6

# Conclusions and outlook

An unprecedented number of dropsonde soundings and DIAL humidity profiles was sampled in the western North Pacific basin during T-PARC. The impact of these adaptive airborne observations on the forecast performance of the ECMWF model was analysed by conducting a series of different OSEs.

High impact weather events such as TCs directly affect the society. In order to minimise the cost of damage and loss of lives, authorities are crucially dependent on accurate TC track and intensity forecasts to coordinate successful evacuations and damage mitigations, especially when a TC approaches land. For example, Taiwan is particularly exposed to TCs in the western North Pacific and an average number of 4-5 storms (2003-2010) threaten the island every year and cause fatalities and tremendous costs.

The study demonstrated that the adaptive T-PARC dropsonde observations are beneficial for TC forecasts. In terms of TC track forecast errors, T-PARC dropsonde observations, on average, reduced the track forecast errors of the two Typhoons Sinlaku and Jangmi in the analysed period by 15%. The results differed for the two storms and the beneficial impact of the dropsondes was larger during Sinlaku. The impact was most beneficial in the pre-recurvature stage of the TCs when a large uncertainty in the track forecast was present. The differences of a cycled and uncycled experimental setup were significant and the improvements found in the cycled experiment were diminished in the uncycled one. In the cycled experiment, the ‘data impact’ of the observations remains in the model system and successive analyses are influenced by the latest adaptive observations and by changes to the background field resulting from previous adaptive observations. This result underlines that the cycled mode, which also represents the operational setup, is most suitable to achieve the largest overall impact of adaptive observations.

One of the main goals of this thesis was to examine in which location adaptive dropsonde observations are most beneficial for the forecast of TCs. Based on a subjective classification,

the dropsonde observations were separated into three different subsets depending on the location relative to the TC. Different uncycled experiments were conducted to assess the analysis and forecast influence of each particular set of adaptive observations.

The first set of dropsondes, launched in the vicinity of the TC, led to the largest TC track forecast improvements, especially at initial times before landfall. These sondes were located at an annulus around the TC centre at a distance of approximately 500 km. The importance of this region was also often highlighted by different targeting guidances. The second class, dropsondes deployed in SV-based sensitive areas which were not directly tied to the storm itself (distance  $\geq 700$  km), only achieved small track forecast improvements. There are indications that refinements in the calculation of SV sensitive areas relocate the maximum sensitivity closer to the storm (Lang et al., 2011), but more work would be required to gain significant results. In addition, SVs (unlike ETKF) do not consider the actual analysis error of the model system. It may be assumed, that the analysis, produced by a modern 4-D Var data assimilation system assimilating millions of satellite observations, already represents the large scale flow patterns accurately compared to regions close to the storm. This may limit the influence of adaptive observations in those distant sensitive areas. The third group consisted of dropsondes placed in the TC centre and core. These observations had a large analysis influence, and improved and deteriorated track forecasts were found with an overall neutral impact. To date, operational data assimilation schemes are not able to fully exploit the potential information of the TC centre and core observations and the risk of a forecast degradation from assimilating these data is increased in the ECMWF and other global models (Aberson, 2008; Weissmann et al., 2011).

The correct intensity forecast of a TC still remains challenging. Large intensity errors were found in this study and intensity forecasts were only slightly improved by adaptive dropsonde observations. Especially dropsondes in the centre and eye wall of the TC may have potential to improve the TC intensity forecast as they are able to fix the centre of the storm, modify the TC wind structure and reduce the central pressure of the system in the analysis.

The positive influence of dropsonde observations on the typhoon track forecasts during T-PARC is also relevant for THORPEX and contributed to the statement of the Data Assimilation and Observing Systems Working Group (DAOS WG) that ‘targeted observations aimed at improving forecasts of tropical cyclone track have provided demonstrable positive impact’<sup>1</sup>. However, considering ongoing operational surveillance programmes for tropical cyclones in the Atlantic and the western North Pacific basin, the effectiveness of adaptive observations and of sensitive area calculations has to be addressed continuously. In the future, the discovered beneficial impact of dropsonde observations in the vicinity of

---

<sup>1</sup>[http://web.sca.uqam.ca/~wgne/DAOS/DAOS3\\_meeting/21\\_DAOSWG\\_03\\_\\_ICSC8.pdf](http://web.sca.uqam.ca/~wgne/DAOS/DAOS3_meeting/21_DAOSWG_03__ICSC8.pdf)

the typhoon during T-PARC has to be analysed considering prospective refinements in the forecast models, the assimilation systems and the sensitive area calculations (Lang et al., 2011) as well as the influence of different stages of the TC and dynamical features affecting its movement (Chen et al., 2009; Kim and Jung, 2009; Reynolds et al., 2009). Further, the importance of deploying dropsondes all around the storm in contrast to only observing one side of the TC has to be assessed.

In addition, operationally available observations of the GOS such as satellite observations could be utilised as targeted observations for tropical cyclones, for example by applying sensitive-area-based satellite data thinning (Bauer et al., 2011). A 10-year research plan<sup>2</sup> was recently proposed within the NOAA Hurricane Forecast Improvement Project (HFIP). By optimising observing capabilities and providing advanced, high-resolution modelling systems, HFIP intends to further improve track forecasts, extend the operational forecast lead time out to 7 days, and push forward the accuracy of intensity forecasts that showed only little progress during the last years (Zhang et al., 2011). Forecasts of TC intensity and intensity chances are challenging and complex, and in order to fully exploit the capabilities of high-resolution modelling the knowledge of the TC vortex structure also needs to be improved (Gopalakrishnan et al., 2010).

Undoubtedly, there is a need for high-quality water vapour observations in operational weather and climate prediction (e.g. Gérard et al., 2004), as the GOS is lacking accurate high-resolution humidity observations. Newly developed remote sensing DIAL instruments are able to provide precise observations with a high vertical and horizontal resolution. For this reason, the potential of these new type of observations for NWP was analysed and DIAL humidity observations sampled by an airborne instrument were assimilated into the operational ECMWF global model for the first time. It was shown that the DIAL observations added information supplementary to the existing operational observing network and their assimilation improved the quality of the analysis field. When new types of observations are assimilated into an NWP model, it is important to check whether systematic errors between the observations and the model exist, since a bias in the observations can systematically downgrade the data assimilation system and the quality of the forecast (e.g. Agustí-Panareda et al., 2009). For the DIAL observations, a bias compared to the models was identified which appears to be caused by the DIAL observations and uncertainties in the data processing. Hence, a bias correction of the observations might help to optimise the use of DIAL observations in the data assimilation system for future studies.

The adaptive DIAL humidity observations showed an overall small forecast impact. However, two cases were discovered where DIAL observations had a considerable beneficial

---

<sup>2</sup>[http://www.nrc.noaa.gov/plans\\_docs/HFIP\\_Plan\\_073108.pdf](http://www.nrc.noaa.gov/plans_docs/HFIP_Plan_073108.pdf)

impact on the forecast. For these cases, the moisture, which was advected into a developing extratropical cyclone, was modified in the initial conditions. This indicates that the inflow region of moisture into a cyclone can be particularly sensitive to additional humidity observations and errors in the moisture field in this regions directly affect the prediction of the cyclone. These findings emphasise the sensitivity of the cyclone forecast to an accurate initial humidity analysis in the area where diabatic processes such as latent heating and surface heat fluxes are present as these processes play a crucial role in the development of the cyclone.

Diabatic process are also important for the intensification and movement of a TC and an improved initialisation of the TC related moisture distribution would certainly be beneficial for the forecast of the storm. Unfortunately, the vicinity of the TC is characterised by a large amount of convective clouds, which absorb the lidar signal and make it impossible to observe the humidity distribution close to the storm by lidar instruments.

The assimilation of the DIAL observations showed promising results and the importance of a correct humidity analysis near a developing extratropical cyclone was highlighted. To quantify the humidity inflow into extratropical cyclones and to observe latent heat fluxes in regions relevant for extratropical cyclogenesis are key aspects which are addressed in ongoing studies (Schäfler et al., 2011b) and will be examined in future field campaigns with the new High Altitude and Long Range Research Aircraft (HALO). Instead of collecting observations in areas indicated by “classical” targeting guidance, DIAL humidity observations in the upstream regions of prominent diabatic processes may not only help to improve the understanding of involved moist processes, but could also provide a valuable data set for the assimilation into NWP models.

## List of abbreviations

3D-Var	three-Dimensional Variational
4D-Var	four-Dimensional Variational
ADSSV	Adjoint-Derived Sensitivity Steering Vector
AIRS	Atmospheric Infrared Sounder
ALL_DIAL	uncycled OSE assimilating all DIAL observations
AMDAR	Aircraft Meteorological Data Relay
AMSR	Advanced Microwave Scanning Radiometer
AMSU	Advanced Microwave Sounding Unit
AMV	Atmospheric Motion Vector
AV_DIAL	uncycled OSE assimilating horizontally averaged DIAL observations
A-TReC	Atlantic THORPEX Regional Campaign
BgQC	Background Quality Control
CALJET	California Land-falling Jets
CeObs	uncycled OSE assimilating dropsonde observations in the TC center and core region
CMC	Canadian Meteorological Center
CNTL	control OSE without DIAL observations
COPS	Convective and Orographically-Induced Precipitation Study
DAOS WG	Data Assimilation and Observing Systems Working Group
DFS	Degree of Freedom for Signal
DIAL	Differential Absorption Lidar
DLR	Deutsches Zentrum für Luft- und Raumfahrt
DOTSTAR	Dropwindsonde Observations for Typhoon Surveillance near the Taiwan Region
DROP	cycled OSE assimilating dropsonde observations
DROP_UnCy	uncycled OSE assimilating dropsonde observations
DTS	Data Targeting System
ECMWF	European Centre for Medium-Range Weather Forecasts

EOL	Earth Observing Laboratory
EPS	Ensemble Prediction System
ERA40	ECMWF 40-yr Reanalysis
ESA	European Space Agency
ET	Extratropical Transition
ETKF	Ensemble Transform Kalman Filter
EZMW	Europäisches Zentrum für Mittelfristige Wettervorhersage
E-TReC	European THORPEX Regional Campaign
FASTEX	Fronts and Atlantic Storm-Track Experiment
GFS	Global Forecasting System
GOS	Global Observing System
GPS	Global Positioning System
GTS	Global Telecommunication System
HIRS	High Resolution Infrared Sounder
HFIP	Hurricane Forecast Improvement Project
IASI	Infrared Atmospheric Sounding Interferometer
IHOP_2002	International H <sub>2</sub> O Project
HALO	High Altitude and Long Range Research Aircraft
JMA	Japan Meteorological Agency
JTWC	Joint Typhoon Warning Center
L91	vertical model resolution; exemplary: 91 levels
LASE	Lidar Atmospheric Sensing Experiment
MHS	Microwave Humidity Sounder
MM5	fifth-generation Pennsylvania State University / NCAR Mesoscale Model
MSL	Mean Sea Level
MSLP	Mean Sea Level Pressure
MTE	Moist Total Energy
MTSAT	Multi-functional Transport Satellite
NCAR	National Center for Atmospheric Research
NCEP	National Centers for Environmental Prediction
NOAA	National Oceanic and Atmospheric Administration
NOGAPS	Navy Operational Global Atmospheric Prediction System
NoObs	control OSE without dropsonde observations
NORPEX	North-Pacific Experiment
NRL	Naval Research Laboratory
NWP	Numerical Weather Prediction

OI	Observations Influence
OSE	Observing System Experiment
PANDOWAE	Predictability and Dynamics Of Weather Systems in the Atlantic-European Sector
PWC	Precipitable Water Content
ReObs	uncycled OSE assimilating dropsonde observations in remote sensitive regions
RMS	Root Mean Square
RSMC	Regional Specialized Meteorological Center
SBUV	Solar Backscattering Ultraviolet
SSM/I	Special Sensor Microwave / Imager
SV	Singular Vector
SYNOP	in-situ synoptic observation
TC	Tropical Cyclone
TCS08	Tropical Cyclone Structure 2008
TCWV	Total Column Water Vapour
TE	Total Energy
TEMP	radiosonde sounding
THORPEX	The Observing System Research and Predictability Experiment
TimeErr	cycled OSE assimilating dropsonde observations with erroneous observation times
TRMM	Tropical Rainfall Measurement Mission
T-PARC	THORPEX Pacific Asian Regional Campaign
$T_L799$	spectral model resolution; exemplary: truncation after wave number 799
UKMO	United Kingdom Met Office
UTC	Coordinated Universal Time
VarQC	Variational Quality Control
ViObs	uncycled OSE assimilating dropsonde observations in the vicinity of the TC
WALES	Water Vapour Lidar Experiment in Space
WMO	World Meteorological Organization
WSR	Winter Storm Reconnaissance
WWRP	World Weather Research Programme



# Bibliography

- Aberson, S. and J. Franklin, 1999: Impact on hurricane track and intensity forecasts of GPS dropwindsonde observations from the first-season flights of the NOAA Gulfstream-IV jet aircraft. *Bull. Amer. Meteorol. Soc.*, **80**, 421–427.
- Aberson, S. D., 2002: Two years of operational hurricane synoptic surveillance. *Wea. Forecasting*, **17**, 1101–1110.
- Aberson, S. D., 2003: Targeted observations to improve operational tropical cyclone track forecast guidance. *Mon. Wea. Rev.*, **131**, 1613–1628.
- Aberson, S. D., 2008: Large forecast degradations due to synoptic surveillance during the 2004 and 2005 hurricane seasons. *Mon. Wea. Rev.*, **136**, 3138–3150.
- Aberson, S. D., 2010: 10 years of hurricane synoptic surveillance (1997–2006). *Mon. Wea. Rev.*, **138**, 1536–1549.
- Aberson, S. D., S. J. Majumdar, C. A. Reynolds, and B. J. Etherton, 2010: An observing system experiment for tropical cyclone targeting techniques using the Global Forecast System. *Mon. Wea. Rev.*, doi:10.1175/2010MWR3397.1.
- Agustí-Panareda, A., D. Vasiljevic, A. Beljaars, O. Bock, F. Guichard, M. Nuret, A. Mendez, E. Andersson, P. Bechtold, A. Fink, H. Hersbach, J.-P. Lafore, J.-B. Ngamini, D. J. Parker, J.-L. Redelsperger, and A. M. Tompkins, 2009: Radiosonde humidity bias correction over the West African region for the special AMMA reanalysis at ECMWF. *Quart. J. Roy. Meteor. Soc.*, **135**, 595–617.
- Andersson, E., P. Bauer, A. Beljaars, F. Chevallier, E. Hólm, M. Janisková, P. Kållberg, G. Kelly, P. Lopez, A. McNally, E. Moreau, A. J. Simmons, J. N. Thépaut, and A. M. Tompkins, 2005: Assimilation and modeling of the atmospheric hydrological cycle in the ECMWF forecasting system. *Bull. Amer. Meteorol. Soc.*, **86**, 387–402.

- Andersson, E., E. Holm, P. Bauer, A. Beljaars, G. A. Kelly, A. P. McNally, A. J. Simmons, J. N. Thépaut, and A. M. Tompkins, 2007: Analysis and forecast impact of the main humidity observing systems. *Quart. J. Roy. Meteor. Soc.*, **133**, 1473–1485.
- Andersson, E. and H. Järvinen, 1999: Variational quality control. *Quart. J. Roy. Meteor. Soc.*, **125**, 697–722.
- Bauer, P., R. Buizza, C. Cardinali, and J. Thépaut, 2011: Impact of singular-vector-based satellite data thinning on NWP. *Quart. J. Roy. Meteor. Soc.*, **137**, 286–302.
- Bauer, P., A. Geer, P. Lopez, and D. Salmond, 2010: Direct 4D-Var assimilation of all-sky radiances. Part I: Implementation. *Quart. J. Roy. Meteor. Soc.*, **136**, 1868–1885.
- Behrendt, A., V. Wulfmeyer, H. Bauer, T. Schaberl, P. Di Girolamo, D. Summa, C. Kiemle, G. Ehret, D. Whiteman, B. Demoz, E. V. Browell, S. Ismail, R. Ferrare, S. Kooi, and J. Wang, 2007a: Intercomparison of water vapor data measured with lidar during IHOP\_2002. Part I: airborne to ground-based lidar systems and comparisons with chilled-mirror hygrometer radiosondes. *J. Atmos. Oceanic Technol.*, **24**, 3–21.
- Behrendt, A., V. Wulfmeyer, T. Schaberl, H. Bauer, C. Kiemle, G. Ehret, C. Flamant, S. Kooi, S. Ismail, R. Ferrare, E. V. Browell, and D. N. Whiteman, 2007b: Intercomparison of water vapor data measured with lidar during IHOP\_2002. Part II: airborne-to-airborne systems. *J. Atmos. Oceanic Technol.*, **24**, 22–39.
- Bengtsson, L. and K. Hodges, 2005: On the impact of humidity observations in numerical weather prediction. *Tellus*, **57A**, 701–708.
- Bengtsson, L., K. Hodges, and S. Hagemann, 2004: Sensitivity of large-scale atmospheric analyses to humidity observations and its impact on the global water cycle and tropical and extratropical weather systems in ERA40. *Tellus*, **56A**, 202–217.
- Bergot, T., 2001: Influence of the assimilation scheme on the efficiency of adaptive observations. *Quart. J. Roy. Meteor. Soc.*, **127**, 635–660.
- Bhawar, R., P. Di Girolamo, D. Summa, C. Flamant, D. Althausen, A. Behrendt, C. Kiemle, P. Bossler, C. Cacciani, C. Champollion, T. Di Iorio, R. Engelmann, C. Herold, S. Pal, M. Wirth, and V. Wulfmeyer, 2011: The water vapour intercomparison effort in the framework of the Convective and Orographically-induced Precipitation Study: airborne-to-ground-based and airborne-to-airborne lidar systems. *Quart. J. Roy. Meteor. Soc.*, **137**, 325–348.

- Bishop, C. H., B. J. Etherton, and S. J. Majumdar, 2001: Adaptive sampling with the ensemble transform Kalman filter. Part I: Theoretical aspects. *Mon. Wea. Rev.*, **129**, 420–436.
- Biswas, M. and T. Krishnamurti, 2008: Adaptive use of research aircraft data sets for hurricane forecasts. *Meteorol. Atmos. Phys.*, **99**, 43–64.
- Bjerknes, V., 1904: Das Problem der Wettervorhersage, betrachtet vom Standpunkte der Mechanik und der Physik. *Meteorol. Z.*, **21**, 1–7.
- Bohren, C. F. and B. A. Albrecht, 1998: *Atmospheric Thermodynamics*. Oxford University Press, New York, NY, 402 pp.
- Bösenberg, J., 1998: Ground-based differential absorption lidar for water-vapor and temperature profiling: methodology. *Appl. Opt.*, **37**, 3845–3860.
- Bösenberg, J., 2005: Differential-absorption lidar for water vapor and temperature profiling. *Lidar*, C. Weitkamp, Ed., Springer Berlin / Heidelberg, Springer Series in Optical Sciences, Vol. 102, 213–239.
- Bouttier, F. and G. Kelly, 2001: Observing-system experiments in the ECMWF 4D-Var data assimilation system. *Quart. J. Roy. Meteor. Soc.*, **127**, 1469–1488.
- Bouttier, P. and F. Rabier, 1998: The operational implementation of 4D-Var. ECMWF Newsletter 78, 7–14 pp.
- Browell, E., S. Ismail, and W. Grant, 1998: Differential absorption lidar (DIAL) measurements from air and space. *Appl. Phys.*, **67B**, 399–410.
- Bruneau, D., P. Quaglia, C. Flamant, M. Meissonnier, and J. Pelon, 2001: Airborne lidar LEANDRE II for water-vapor profiling in the troposphere. I. System description. *Appl. Opt.*, **40**, 3450–3461.
- Buizza, R. and A. Montani, 1999: Targeting observations using singular vectors. *J. Atmos. Sci.*, **56**, 2965–2985.
- Buizza, R. and T. Palmer, 1995: The singular-vector structure of the atmospheric global circulation. *Journal of the Atmospheric Sciences*, **52**, 1434–1456.
- Burpee, R., D. Marks, and R. Merrill, 1984: An assessment of Omega dropwindsonde data in track forecasts of Hurricane Debby (1982). *Bull. Amer. Meteorol. Soc.*, **65**, 1050–1058.

- Burpee, R. W., J. L. Franklin, S. J. Lord, R. E. Tuleya, and S. D. Aberson, 1996: The impact of Omega dropwindsondes on operational hurricane track forecast models. *Bull. Amer. Meteorol. Soc.*, **77**, 925–933.
- Cardinali, C., S. Pezzulli, and E. Andersson, 2004: Influence-matrix diagnostic of a data assimilation system. *Quart. J. Roy. Meteor. Soc.*, **130**, 2767–2786.
- Chen, J., M. Peng, C. Reynolds, and C. Wu, 2009: Interpretation of tropical cyclone forecast sensitivity from the singular vector perspective. *J. Atmos. Sci.*, **66**, 3383–3400.
- Chou, K., C. Wu, P. Lin, S. Aberson, M. Weissmann, F. Harnisch, and T. Nakazawa, 2010: The impact of dropwindsonde observations on typhoon track forecasts in DOTSTAR and T-PARC. *Mon. Wea. Rev.*, doi:10.1175/2010MWR3582.1.
- Courtier, P., J. Thépaut, and A. Hollingsworth, 1994: A strategy for operational implementation of 4D-Var, using an incremental approach. *Quart. J. Roy. Meteor. Soc.*, **120**, 1367–1387.
- Dando, M., A. Thorpe, and J. Eyre, 2007: The impact of targeted satellite observations on numerical weather prediction. *Quart. J. Roy. Meteor. Soc.*, **133**, 1945–1957.
- Desroziers, G., L. Berre, B. Chapnik, and P. Poli, 2005: Diagnosis of observation, background and analysis-error statistics in observation space. *Quart. J. Roy. Meteor. Soc.*, **131**, 3385–3396.
- Ebert, E., U. Damrath, W. Wergen, and M. Baldwin, 2003: The WGNE assessment of short-term quantitative precipitation forecasts. *Bull. Amer. Meteorol. Soc.*, **84**, 481–492.
- Ehrendorfer, M., R. Errico, and K. Raeder, 1999: Singular-vector perturbation growth in a primitive equation model with moist physics. *J. Atmos. Sci.*, **56**, 1627–1648.
- Ehret, G., K. Hoinka, J. Stein, A. Fix, C. Kiemle, and G. Poberaj, 1999: Low stratospheric water vapor measured by an airborne DIAL. *J. Geophys. Res.*, **104**, 31 351–31 359.
- Elsberry, R. L. and P. A. Harr, 2008: Tropical Cyclone Structure (TCS08) field experiment science basis, observational platforms, and strategy. *Asia-Pacific J. Atmos. Sci.*, **44**, 209–231.
- Fiorino, M., 2009: Record-setting performance of the ECMWF IFS in medium-range tropical cyclone track prediction. ECMWF Newsletter 118, 20–27 pp.
- Fisher, M., 2003: Background error covariance modelling. *Recent developments in data assimilation for atmosphere and ocean*, 45–63, ECMWF Seminar.

- Flentje, H., A. Dörnbrack, A. Fix, G. Ehret, and E. Hólm, 2007: Evaluation of ECMWF water vapour fields by airborne differential absorption lidar measurements: a case study between Brazil and Europe. *Atmos. Chem. Phys.*, **7**, 5033–5042.
- Fourrié, N. and F. Rabier, 2004: Cloud characteristics and channel selection for IASI radiances in meteorologically sensitive areas. *Quart. J. Roy. Meteor. Soc.*, **130**, 1839–1856.
- Gérard, É., D. G. H. Tan, L. Garand, V. Wulfmeyer, G. Ehret, and P. Di Girolamo, 2004: Major advances foreseen in humidity profiling from the Water Vapour Lidar Experiment in Space (WALES). *Bull. Amer. Meteorol. Soc.*, **85**, 237–251.
- Gilleland, E., D. A. Ahijevych, B. G. Brown, and E. E. Ebert, 2010: Verifying forecasts spatially. *Bull. Amer. Meteorol. Soc.*, **91**, 1365–1373.
- Gimmestad, G., 2005: Differential-absorption lidar for ozone and industrial emissions. *Lidar*, C. Weitkamp, Ed., Springer Berlin / Heidelberg, Springer Series in Optical Sciences, Vol. 102, 187–212.
- Gopalakrishnan, S. G., F. D. Marks, X. Zhang, J.-W. Bao, K. Yeh, and R. Atlas, 2010: The experimental HWRF system: A study of the influence of resolution on the structure and intensity changes in tropical cyclones using an idealized framework. *Mon. Wea. Rev.*, doi:10.1175/2010MWR3535.1.
- Hagedorn, R., 2010: Operational and research activities at ECMWF. ECMWF Training Course: *Data assimilation and use of satellite data*, [http://www.ecmwf.int/newsevents/training/meteorological\\_presentations/MET\\_DA.html](http://www.ecmwf.int/newsevents/training/meteorological_presentations/MET_DA.html).
- Healy, S. and J. Thépaut, 2006: Assimilation experiments with CHAMP GPS radio occultation measurements. *Quart. J. Roy. Meteor. Soc.*, **132**, 605–623.
- Hock, T. and J. Franklin, 1999: The NCAR GPS dropwindsonde. *Bull. Amer. Meteorol. Soc.*, **80**, 407–420.
- Hólm, E., E. Andersson, A. Beljaars, P. Lopez, J. Mahfouf, A. Simmons, and J. Thépaut, 2002: Assimilation and modelling of the hydrological cycle: ECMWF's status and plans. ECMWF Technical Memo 383.
- Irvine, E., S. Gray, J. Methven, I. Renfrew, K. Bovis, and R. Swinbank, 2009: The impact of targeted observations made during the Greenland Flow Distortion Experiment. *Quart. J. Roy. Meteor. Soc.*, **135**, 2012–2029.

- Isaksen, L., 2010: The operational data assimilation system. ECMWF Training Course: *Data assimilation and use of satellite data*, [http://www.ecmwf.int/newsevents/training/meteorological\\_presentations/MET\\_DA.html](http://www.ecmwf.int/newsevents/training/meteorological_presentations/MET_DA.html).
- Ismail, S. and E. V. Browell, 1989: Airborne and spaceborne lidar measurements of water vapor profiles: a sensitivity analysis. *Appl. Opt.*, **28**, 3603–3615.
- Järvinen, H. and P. Undèn, 1997: Observation screening and background quality control in the ECMWF 3D Var data assimilation system . ECMWF Technical Memo 236.
- Joly, A., K. Browning, P. Bessemoulin, J. Cammas, G. Caniaux, J.-P. Chalon, S. Clough, R. Dirks, K. Emanuel, L. Eymard, R. Gall, T. Hewson, P. Hildebrand, D. Jorgensen, F. Lalauette, R. Langland, Y. Lemaître, P. Marcart, J. Moore, P. Persson, F. Roux, M. Shapiro, C. Snyder, Z. Toth, and R. Wakimoto, 1999: Overview of the field phase of the Fronts and Atlantic Storm-Track EXperiment (FASTEX) project. *Quart. J. Roy. Meteor. Soc.*, **125**, 3131–3163.
- Kalnay, E., 2003: *Atmospheric Modeling, Data Assimilation and Predictability*. Cambridge University Press, UK.
- Kamineni, R., T. Krishnamurti, R. Ferrare, S. Ismail, and E. Browell, 2003: Impact of high resolution water vapor cross-sectional data on hurricane forecasting. *Geophys. Res. Lett.*, **30**, 1234, doi:10.1029/2002GL016741.
- Kamineni, R., T. Krishnamurti, S. Pattnaik, E. Browell, S. Ismail, and R. Ferrare, 2006: Impact of CAMEX-4 datasets for hurricane forecasts using a global model. *J. Atmos. Sci.*, **63**, 151–174.
- Keil, C., A. Röpnack, G. Craig, and U. Schumann, 2008: Sensitivity of quantitative precipitation forecast to height dependent changes in humidity. *Geophys. Res. Lett.*, **35**, L09 812, doi:10.1029/2008GL033657.
- Kelly, G., J. N. Thepaut, R. Buizza, and C. Cardinali, 2007: The value of observations. I: Data denial experiments for the Atlantic and the Pacific. *Quart. J. Roy. Meteor. Soc.*, **133**, 1803–1815.
- Kiemle, C., 2008: Airborne water vapor lidar measurements. DLR Forschungsbericht 2008–19, DLR Oberpfaffenhofen, Germany. 94 pp.
- Kiemle, C., G. Ehret, A. Fix, M. Wirth, G. Poberaj, W. A. Brewer, R. M. Hardesty, C. Senff, and M. A. LeMone, 2007: Latent Heat Flux Profiles from Collocated Airborne

- Water Vapor and Wind Lidars during IHOP\_2002. *J. Atmos. Oceanic Technol.*, **24**, 627–639.
- Kiemle, C., M. Wirth, A. Fix, G. Ehret, U. Schumann, T. Gardiner, C. Schiller, N. Sitenikov, and G. Stiller, 2008: First airborne water vapor lidar measurements in the tropical upper troposphere and mid-latitudes lower stratosphere: accuracy evaluation and inter-comparisons with other instruments. *Atmos. Chem. Phys.*, **8**, 5245–5261.
- Kim, H. and B. Jung, 2009: Singular vector structure and evolution of a recurving tropical cyclone. *Mon. Wea. Rev.*, **137**, 505–524.
- Klinker, E., F. Rabier, G. Kelly, and J.-F. Mahfouf, 2000: The ECMWF operational implementation of four-dimensional variational assimilation. III: Experimental results and diagnostics with operational configuration. *Quart. J. Roy. Meteor. Soc.*, **126**, 1191–1215.
- Lang, S., S. Jones, M. Leutbecher, M. Peng, and C. Reynolds, 2011: Sensitivity, structure and dynamics of singular vectors associated with Hurricane Helene (2006). *J. Atmos. Sci.*, -, submitted.
- Langland, R. and N. Baker, 2004: Estimation of observation impact using the NRL atmospheric variational data assimilation adjoint system. *Tellus*, **56A**, 189–201.
- Langland, R., C. Velden, P. Pauley, and H. Berger, 2009: Impact of satellite-derived rapid-scan wind observations on numerical model forecasts of Hurricane Katrina. *Mon. Wea. Rev.*, **137**, 1615–1622.
- Langland, R. H., 2005a: Issues in targeted observing. *Quart. J. Roy. Meteor. Soc.*, **131**, 3409–3425.
- Langland, R. H., 2005b: Observation impact during the North Atlantic TReC-2003. *Mon. Wea. Rev.*, **133**, 2297–2309.
- Langland, R. H., Z. Toth, R. Gelaro, I. Szunyogh, M. A. Shapiro, S. J. Majumdar, R. E. Morss, G. D. Rohaly, C. Velden, N. Bond, and C. H. Bishop, 1999: The North Pacific experiment (NORPEX-98): Targeted observations for improved North American weather forecasts. *Bull. Amer. Meteorol. Soc.*, **80**, 1363–1384.
- Lorenz, E., 1963: Deterministic nonperiodic flow. *J. Atmos. Sci.*, **20**, 130–141.
- Mahfouf, J.-F. and F. Rabier, 2000: The ECMWF operational implementation of four-dimensional variational assimilation. II: Experimental results with improved physics. *Quart. J. Roy. Meteor. Soc.*, **126**, 1171–1190.

- Majumdar, S. J., S. D. Aberson, C. H. Bishop, R. Buizza, M. S. Peng, and C. A. Reynolds, 2006: A comparison of adaptive observing guidance for Atlantic tropical cyclones. *Mon. Wea. Rev.*, **134**, 2354–2372.
- Majumdar, S. J., C. H. Bishop, B. J. Etherton, and Z. Toth, 2002: Adaptive sampling with the ensemble transform Kalman filter. Part II: Field program implementation. *Mon. Wea. Rev.*, **130**, 1356–1369.
- Marécal, V., É. Gérard, J. Mahfouf, and P. Bauer, 2001: The comparative impact of the assimilation of SSM/I and TMI brightness temperatures in the ECMWF 4D-Var system. *Quart. J. Roy. Meteor. Soc.*, **127**, 1123–1142.
- Marécal, V., J. Mahfouf, and P. Bauer, 2002: Comparison of TMI rainfall estimates and their impact on 4D-Var assimilation. *Quart. J. Roy. Meteor. Soc.*, **128**, 2737–2758.
- McNally, A., 2002: A note on the occurrence of cloud in meteorologically sensitive areas and the implications for advanced infrared sounders. *Quart. J. Roy. Meteor. Soc.*, **128**, 2551–2556.
- Montani, A., A. Thorpe, R. Buizza, and P. Uden, 1999: Forecast skill of the ECMWF model using targeted observations during FASTEX. *Quart. J. Roy. Meteor. Soc.*, **125**, 3219–3240.
- Morss, R. E. and K. A. Emanuel, 2002: Influence of added observations on analysis and forecast errors: Results from idealized systems. *Quart. J. Roy. Meteor. Soc.*, **128**, 285–321.
- Parrish, D. and J. Derber, 1992: The National Meteorological Center’s spectral statistical-interpolation analysis system. *Mon. Wea. Rev.*, **120**, 1747–1763.
- Peng, M. S. and C. A. Reynolds, 2006: Sensitivity of tropical cyclone forecasts as revealed by singular vectors. *J. Atmos. Sci.*, **63**, 2508–2528.
- Persson, A. and F. Grazzini, 2007: User Guide to ECMWF forecast products. ECMWF, V4.0, 153 pp. Available from ECMWF, Reading, UK: [http://www.ecmwf.int/products/forecasts/guide/user\\_guide.pdf](http://www.ecmwf.int/products/forecasts/guide/user_guide.pdf).
- Petersen, G. N. and A. J. Thorpe, 2007: The impact on weather forecasts of targeted observations during A-TReC. *Quart. J. Roy. Meteor. Soc.*, **133**, 417–431.
- Pierrehumbert, R., 2002: The hydrologic cycle in deep-time climate problems. *Nature*, **419**, 191–198.

- Poberaj, G., A. Fix, A. Assion, M. Wirth, C. Kiemle, and G. Ehret, 2002: Airborne all-solid-state DIAL for water vapour measurements in the tropopause region: system description and assessment of accuracy. *Appl. Phys.*, **75B**, 165–172.
- Poli, P., P. Moll, F. Rabier, G. Desroziers, B. Chapnik, L. Berre, S. Healy, E. Andersson, and F. El Guelai, 2007: Forecast impact studies of zenith total delay data from European near real-time GPS stations in Meteo France 4DVAR. *J. Geophys. Res.*, **112**, D06 114, doi:10.1029/2006JD007430.
- Pu, Z., E. Kalnay, J. Sela, and I. Szunyogh, 1997: Sensitivity of forecast errors to initial conditions with a quasi-inverse linear method. *Mon. Wea. Rev.*, **125**, 2479–2503.
- Rabier, F., P. Gauthier, C. Cardinali, R. Langland, M. Tsyrlunikov, A. Lorenc, P. Steinle, R. Gelaro, and K. Koizumi, 2008: An update on THORPEX-related research in data assimilation and observing strategies. *Nonlin. Processes Geophys.*, **15**, 81–94.
- Rabier, F., H. Jarvinen, E. Klinker, J.-F. Mahfouf, and A. Simmons, 2000: The ECMWF operational implementation of four-dimensional variational assimilation. I: Experimental results with simplified physics. *Quart. J. Roy. Meteor. Soc.*, **126**, 1143–1170.
- Rabier, F., E. Klinker, P. Courtier, and A. Hollingsworth, 1996: Sensitivity of forecast errors to initial conditions. *Quart. J. Roy. Meteor. Soc.*, **122**, 121–150.
- Reynolds, C. A., M. S. Peng, and J.-H. Chen, 2009: Recurving tropical cyclones: singular vector sensitivity and downstream impacts. *Mon. Wea. Rev.*, **137**, 1320–1337.
- Reynolds, C. A., M. S. Peng, S. J. Majumdar, S. D. Aberson, C. H. Bishop, and R. Buizza, 2007: Interpretation of adaptive observing guidance for Atlantic tropical cyclones. *Mon. Wea. Rev.*, **135**, 4006–4029.
- Richardson, D., J. Bidlot, L. Ferranti, A. Ghelli, C. Gibert, T. Hewson, M. Janousek, F. Prates, and F. Vitart, 2009: Verification statistics and evaluations of ECMWF forecasts in 2008-2009. ECMWF Technical Memo 606.
- Schäfler, A., A. Dörnbrack, C. Kiemle, S. Rahm, and M. Wirth, 2011a: Tropospheric water vapor transport as determined from airborne lidar measurements. *J. Atmos. Oceanic Technol.*, **27**, 2017–2030.
- Schäfler, A., A. Dörnbrack, H. Wernli, C. Kiemle, and S. Pfahl, 2011b: Airborne lidar observations in the inflow region of a Warm Conveyor Belt. *Quart. J. Roy. Meteor. Soc.*, **137**, 1257–1272.

- Snyder, C., 1996: Summary of an informal workshop on adaptive observations and FASTEX. *Bull. Am. Meteor. Soc.*, **77**, 953–961.
- Sun, B., A. Reale, D. Seidel, and D. Hunt, 2010: Comparing radiosonde and COSMIC atmospheric profile data to quantify differences among radiosonde types and the effects of imperfect collocation on comparison statistics. *J. Geophys. Res.*, **115**, D23 104.
- Szunyogh, I., Z. Toth, R. E. Morss, S. J. Majumdar, B. J. Etherton, and C. H. Bishop, 2000: The effect of targeted dropsonde observations during the 1999 Winter Storm Reconnaissance Program. *Mon. Wea. Rev.*, **128**, 3520–3537.
- Szunyogh, I., Z. Toth, A. Zimin, S. J. Majumdar, and A. Persson, 2002: Propagation of the effect of targeted observations: The 2000 Winter Storm Reconnaissance Program. *Mon. Wea. Rev.*, **130**, 1144–1165.
- Thorpe, A. J. and G. N. Petersen, 2005: Predictability and Targeted Observations. *Predictability of Weather and Climate*, T. Palmer and R. Hagedorn, Eds., Cambridge University Press, 561–583.
- Van der Grijn, G., J. E. Paulsen, F. Lalaurette, and M. Leutbecher, 2005: Early medium-range forecasts of tropical cyclones. ECMWF Newsletter 102, 7–14 pp.
- Velden, C., J. Daniels, D. Stettner, D. Santek, J. Key, J. Dunion, K. Holmlund, G. Dengel, W. Bresky, and P. Menzel, 2005: Recent innovations in deriving tropospheric winds from meteorological satellites. *Bull. Amer. Meteorol. Soc.*, **86**, 205–223.
- Wandinger, U., 2005: Introduction to Lidar. *Lidar*, C. Weitkamp, Ed., Springer Berlin / Heidelberg, Springer Series in Optical Sciences, Vol. 102, 213–239.
- Wang, J., 2005: Evaluation of the dropsonde humidity sensor using data from DYCOMS-II and IHOP\_2002. *J. Atmos. Oceanic Technol.*, **22**, 247–257.
- Wang, J., L. Zhang, P. Lin, M. Bradford, H. Cole, J. Fox, J. Hock, D. Lauritsen, S. Loehrer, C. Martin, J. VanAndel, C. Weng, and K. Young, 2010: Water vapor variability and comparisons in the subtropical Pacific from The Observing System Research and Predictability Experiment-Pacific Asian Regional Campaign (T-PARC) Driftsonde, Constellation Observing System for Meteorology, Ionosphere, and Climate (COSMIC), and reanalyses. *J. Geophys. Res.*, **115**, D21 108, doi:10.1029/2010JD014494.
- Weissmann, M., R. Busen, A. Dörnbrack, S. Rahm, and O. Reitebuch, 2005: Targeted observations with an airborne wind lidar. *J. Atmos. Oceanic Technol.*, **22**, 1706–1719.

- Weissmann, M. and C. Cardinali, 2007: Impact of airborne Doppler lidar observations on ECMWF forecasts. *Quart. J. Roy. Meteor. Soc.*, **133**, 107–116.
- Weissmann, M., F. Harnisch, C. Wu, P. Lin, Y. Ohta, K. Yamashita, Y. Kim, E. Jeon, T. Nakazawa, and S. Aberson, 2011: The influence of assimilating dropsonde data on typhoon track and mid-latitude forecasts. *Mon. Wea. Rev.*, **139**, 908–920.
- Wirth, M., A. Fix, P. Mahnke, H. Schwarzer, F. Schrandt, and G. Ehret, 2009: The airborne multi-wavelength water vapor differential absorption lidar WALES: system design and performance. *Appl. Phys.*, **96B**, 201–213.
- Wu, C. C., 2001: Numerical simulation of Typhoon Gladys (1994) and its interaction with Taiwan terrain using the GFDL hurricane model. *Mon. Wea. Rev.*, **129**, 1533–1549.
- Wu, C.-C., J.-H. Chen, P.-H. Lin, and K.-H. Chou, 2007a: Targeted observations of tropical cyclone movement based on the adjoint-derived sensitivity steering vector. *J. Atmos. Sci.*, **64**, 2611–2626.
- Wu, C.-C., J.-H. Chen, S. Majumdar, M. Peng, C. Reynolds, S. Aberson, R. Buizza, M. Yamaguchi, S.-G. Chen, T. Nakazawa, and K.-H. Chou, 2009: Intercomparison of targeted observation guidance for tropical cyclones in the Northwestern Pacific. *Mon. Wea. Rev.*, **137**, 2471–2492.
- Wu, C.-C., K.-H. Chou, P.-H. Lin, S. D. Aberson, M. S. Peng, and T. Nakazawa, 2007b: The impact of dropwindsonde data on typhoon track forecasts in DOTSTAR. *Wea. Forecastings*, **22**, 1157–1176.
- Wu, C.-C., P.-H. Lin, S. Aberson, T.-C. Yeh, W.-P. Huang, K.-H. Chou, J.-S. Hong, G.-C. Lu, C.-T. Fong, K.-C. Hsu, I.-I. Lin, P.-L. Lin, and C.-H. Liu, 2005: Dropsonde observations for typhoon surveillance near the Taiwan region (DOTSTAR): An overview. *Bull. Amer. Meteorol. Soc.*, **86**, 787–790.
- Wulfmeyer, V., H.-S. Bauer, M. Grzeschik, A. Behrendt, F. Vandenberghe, E. V. Browell, S. Ismail, and R. A. Ferrare, 2006: Four-dimensional variational assimilation of water vapor differential absorption lidar data: the first case study within IHOP\_2002. *Mon. Wea. Rev.*, **134**, 209–230.
- Wulfmeyer, V. and J. Bösenberg, 1998: Ground-based differential absorption lidar for water-vapor profiling: assessment of accuracy, resolution, and meteorological applications. *Appl. Opt.*, **37**, 3825–3844.

- Yamaguchi, M., T. Iriguchi, T. Nakazawa, and C.-C. Wu, 2009: An observing system experiment for Typhoon Conson (2004) using a singular vector method and DOTSTAR data. *Mon. Wea. Rev.*, **137**, 2801–2816.
- Zhang, C., B. Mapes, and B. Soden, 2003: Bimodality in tropical water vapour. *Quart. J. Roy. Meteor. Soc.*, **129**, 2847–2866.
- Zhang, X., K.-S. Yeh, T. Quirino, S. Gopalakrishnan, F. Marks, S. Goldenberg, and S. Aberson, 2011: HWRFx: Improving hurricane forecasts with high-resolution modeling. *Computing in Science & Engineering*, **13**, 13–21.
- Zus, F., M. Grzeschik, H. Bauer, V. Wulfmeyer, G. Dick, and M. Bender, 2008: Development and optimization of the IPM MM5 GPS slant path 4DVAR system. *Meteorol. Z.*, **17**, 867–885.

# Acknowledgements

At first, I am deeply grateful to Dr. Martin Weissmann who supervised me in the last three years. He assisted me, was always open for questions and spent a lot of time discussing various things with me. He perfectly guided me throughout the last three years but also encouraged me to find my own way and develop my own ideas.

Further, I would like to thank Prof. George C. Craig for supervising this thesis. Our discussions were very fruitful for me and he provided very valuable comments on the manuscript.

I also want to thank Prof. Ulrich Schumann for his support.

The help of various people at ECMWF during the last years and ECMWF computing resources are highly appreciated. In particular, I want to thank Carla Cardinali and Peter Bauer who gave me the chance to spend some time at ECMWF and assisted me with all their helpful advice.

The work of this thesis was performed within the DFG research unit PANDOWAE and I want to say “Thank you” to all people engaged in PANDOWAE. It was a great experience to be part of this excellent research group and I enjoyed the fantastic team spirit.

The possibility to participate in T-PARC was a great experience for me. The work would not have been possible without the T-PARC data set and I am grateful to everybody who participated in the campaign and contributed to its success.

I am thankful to the people of the lidar group for the very nice working atmosphere, especially to Andi for the innumerable coffee breaks trying to keep up the motivation.

I want to thank my family and friends with all my heart for the support through the last years that helped me to conduct my studies and to finish this thesis.



# Curriculum Vitae

---

**Name** : Florian Christian Harnisch

**Born** : 19 October 1981 in Prien (Chiemsee), Germany

**Citizenship** : German

---

## EDUCATION AND PROFESSIONAL TRAINING:

2008–2011      Ph.D. student at DLR, Institut für Physik der Atmosphäre, Oberpfaffenhofen, Germany

01/2008        Diploma in Meteorology, Diploma Thesis: “Airborne Aerosol Measurements: Spatial distribution of aerosols during wintertime”

2003–2008      Study of Meteorology at the University of Innsbruck, Austria

2001–2002      Military service, Bad Reichenhall/Berchtesgaden, Germany

1992–2001      Secondary School Staatliches Landschulheim Marquartstein, Germany

---